Side Reactions in Lithium-Ion Batteries

by

Maureen Han-Mei Tang

A dissertation submitted in partial satisfaction of the
requirements for the degree of
Doctor of Philosophy

in

Chemical Engineering

and the Designated Emphasis

in

Energy Science and Technology

in the

Graduate Division

of the

University of California, Berkeley

Committee in charge:

Professor John Newman, Chair
Professor David Graves
Professor Thomas Devine

Spring 2012

Side Reactions in Lithium-Ion Batteries

Abstract

Side Reactions in Lithium-Ion Batteries

by

Maureen Han-Mei Tang

Doctor of Philosophy in Chemical Engineering

with the Designated Emphasis in

Energy Science and Technology

University of California, Berkeley

Professor John Newman, Chair

Lithium-ion batteries store energy through two electrochemical reactions. In addition to these main reactions, many side reactions are possible. The causes and effects of battery side reactions are usually detrimental, sometimes positive, and almost always very complicated. We investigate here both fundamental and applied aspects of several side reactions using experiments and theory.

In Part I, we develop a new method to characterize the solid-electrolyte-interphase (SEI), a passivating film that is the product of side reactions on the graphite electrode, using ferrocene, a redox shuttle. By comparing ferrocene kinetics in the presence and absence of passivating films, the shuttle functions as an electrochemical probe of the mechanism by which the SEI prevents reaction. We develop our method using a model system of a rotating-disk-electrode (RDE) and glassy carbon. Coupling experimental measurements with a physics-based model aids interpretation of the results. We develop both steady-state and transient methods in the model system before applying the methods to highly oriented pyrolytic graphite (HOPG), which more closely resembles the carbon found in an actual battery. We study the effects of the relative fraction of edge and basal planes, the formation voltage, and the electrolyte anion. We also attempt in-situ atomic-force microscopy to validate our electrochemical measurements.

In Part II, we treat several different overcharge reactions theoretically to explain empirical observations, predict system behavior, and suggest considerations for battery design. We develop a two-dimensional model to explain why lithium deposition occurs preferentially at the edges of electrodes and suggest mitigation techniques. In a separate model, we implement a redox shuttle for overcharge protection. We study how the presence of a redox shuttle affects the macroscale current-potential relations of the battery and optimize the redox potential of the shuttle while considering the tradeoffs between current efficiency and overcharge protection.

Contents

List of Figures

List of Tables

Acknowledgments

I am grateful to Professor Newman for his mentorship over the past five years. His reputation for intellectual rigor is well-deserved, and working for him has trained me to approach problems and question assumptions in an extremely thorough way. His pragmatic, old-school approach to choosing research topics asks not "What will get funded?" or "What will make a high-profile publication?", but "What problems are important, and what can we do about them?" He believes that if you do good and useful work, the grants and citation counts will follow. Professor Newman's attitude towards research is inspiring; he demands quality, not quantity, from his graduate students and never creates an high-pressure atmosphere for them or himself. When I encountered frustrating obstacles, his intellectual insight into the physical problems and his confidence in my ability to solve them led me to success. He encouraged me to explore my interests in teaching, even when it detracted from time spent in lab. I feel very lucky to have been part of his research group.

This work would also not have been possible without help from scientists at Lawrence Berkeley National Laboratory. Venkat Srinivasan was and continues to be generous with his extremely valuable time. His 'big-picture' approach to problems complements nicely Professor Newman's focus on details, and his enthusiasm and optimism are contagious. In the spring of 2010, Venkat's involvement made it possible for us to offer and teach a class on batteries. Experiments in Part I of this thesis were performed in Vince Battaglia's lab at LBNL. His entire group was generous with time, resources, and lab space. Paul Ridgway especially taught me many practical details and also let me drill holes in his glovebox. John Kerr, Phil Ross, Gao Liu, and Robert Kostecki had interesting insight and useful suggestions. The AFM experiments in Chapter 5 were performed by Dr. Ivan Lucas in the Kostecki lab.

Funding for my graduate studies came from the National Science Foundation, the Department of Energy's BATT program, and the Japan Society for the Promotion of Science. In 2011, I spent three months at Kyoto University working with Takeshi Abe's research group through the JSPS Summer Program. Most of Chapter 4 in this thesis is a result of that collaboration. Professor Abe and his group were welcoming and supportive, as was Professor Hiro Fukunaka at Waseda University. The Summer Program was an excellent experience personally and professionally, and Saya Takeuchi was largely responsible for making my stay as enjoyable and productive as it was.

The Newman Lab is a great place to work. I have enjoyed and benefited from time in the attic with colleagues Paul Albertus, Penny Gunterman, Ryan Balliet, Charles Delacourt, Nate Craig, Tony Ferrese, and Alan Berger. Justin Huang, Ariana Husain, and Sida Lu were talented and motivated undergraduate assistants. Teaching electrochemistry with Nate has been an extremely informative and exciting way to finish my studies. Last of all, I'm grateful to the family and friends who made me who I am today, especially my parents. I can't imagine completing a Ph.D. without the skills and attitudes they taught me much earlier in life. I also owe a great deal to Paul Albertus, whose level-headed, analytical approach to all types of problems is inspiring. Paul's original battery class in 2007 led me to join the Newman Lab and gave me a solid start in grad school.

Chapter 1

Introduction

Lithium-ion batteries are a promising option for electric vehicles because of their high energy and power density. However, the high cost of lithium-ion batteries has so far prevented widespread automotive application. One approach to reducing the cost is to improve the energy density of the battery, so that it requires less material. Research efforts to develop new high-energy materials such as silicon nanowires and the vaunted lithium-air battery have captured the imaginations of scientists and the general public alike. However, developing new materials is slow and expensive. Given the high cost and uncertainty of hunting for new materials, a strong case can be made for better engineering of existing materials and systems. One avenue for improving existing systems is to extend the battery lifetime. While current lifetimes of two to five years are suitable for consumer electronics, a lifetime of at least ten years is considered necessary for automotive applications. In order to improve battery lifetime, a better understanding of side reactions in existing systems is necessary. Although side reactions are known to be critical to determining battery lifetime, the mechanisms, the relative importance, and even the identity of various side reactions in lithium-ion batteries are all poorly understood.

1.1 Fundamentals of lithium ion batteries

In a lithium ion battery, positively charged lithium ions travel back and forth between two electrodes upon charge and discharge. At the positive electrode, the following reaction occurs:

$$\mathrm{Li}_y\mathrm{MO}_2 \rightleftharpoons y\mathrm{Li}^+ + e^- + \mathrm{MO}_2 \tag{1.1}$$

MO_2 is a metal oxide such as lithium cobalt oxide (LiCoO_2, abbreviated LCO) or lithium iron phosphate (LiFePO_4, or LFP). At the negative electrode,

$$x\mathrm{Li}^+ + e^- + \mathrm{C}_6 \rightleftharpoons \mathrm{Li}_x\mathrm{C}_6 \tag{1.2}$$

The above reaction is written for graphite, but different alloys and oxides are sometimes used. As written above, both reactions occur from left to right on charge and from right

to left on discharge. Although popular and scientific literature often refers to the positive electrode as the cathode and the negative as the anode, these labels are technically correct only upon discharge. In order to increase the surface area available for electrochemical reaction, electrodes are constructed by mixing micro- or nanoscale particles with conductive additive and polymer binder, then coating the mixture onto a copper or aluminum current collector. The separator is a porous polymer membrane filled with an ionically conducting but electronically insulating electrolyte. For Li-ion cells, the electrolyte is most commonly $LiPF_6$ in a solvent of mixed organics such as ethylene carbonate and diethyl carbonate.

1.2 Side reactions on overcharge

The equilibrium potential U is the thermodynamic driving force for the reaction that generates or consumes current during charge or discharge. During charging, lithium deintercalates from the lattice of the positive electrode and intercalates in the lattice of the negative electrode, causing the equilibrium potential of both reactions to change, as shown in Figure 1.1. Fig. 1.1 shows the potential of several other reactions in addition to the main reactions, which are represented by dotted lines. Lithium deposition occurs at 0.0 V vs. the lithium reference. Deposition can occur during overcharge if the graphite electrode becomes saturated with lithium and the potential drops below 0.0 V. If metallic lithium plates on the electrode surface instead of intercalating into the particle, it may cause dendrite formation. Dendrites are both a safety and lifetime problem because they can grow across the cell separator and cause short-circuiting; their formation is a major obstacle for the use of lithium metal as a negative electrode.

Overcharge has detrimental effects on the positive electrode as well as the negative. If too much lithium is removed from the positive electrode, the voltage of the positive electrode rises above the stability limit of the electrolyte. Above approximately 4.3 V, solvents and salt begin to oxidize on the positive electrode. The detrimental consequences of overcharge reactions include capacity fade, both by loss of cyclable lithium and by loss of active material. The exact decomposition reactions vary greatly with the specific material used for the positive electrode and can be very complicated. Vetter et al. give a recent review [1].

To prevent overcharge, manufacturers include sensors and circuitry to monitor the voltage of each battery while charging and to stop passing current when a given cutoff potential is reached. This process is called cell balancing, and does not present a serious issue in consumer devices because the number of cells to monitor is small. However, electric vehicles require thousands of series- and parallel-connected cells in order to achieve the voltage and energy required, and cell balancing these systems quickly becomes complicated and expensive. Chemical redox shuttles offer a proposed alternative to cell balancing. A molecule with a standard potential at or slightly higher than the desired cutoff potential is added to the electrolyte. When the cathode potential rises above the redox potential, the chemical is oxidized to a radical cation. The resulting concentration gradient causes the cation to diffuse to the negative electrode, where it is reduced to the neutral form and diffuses back

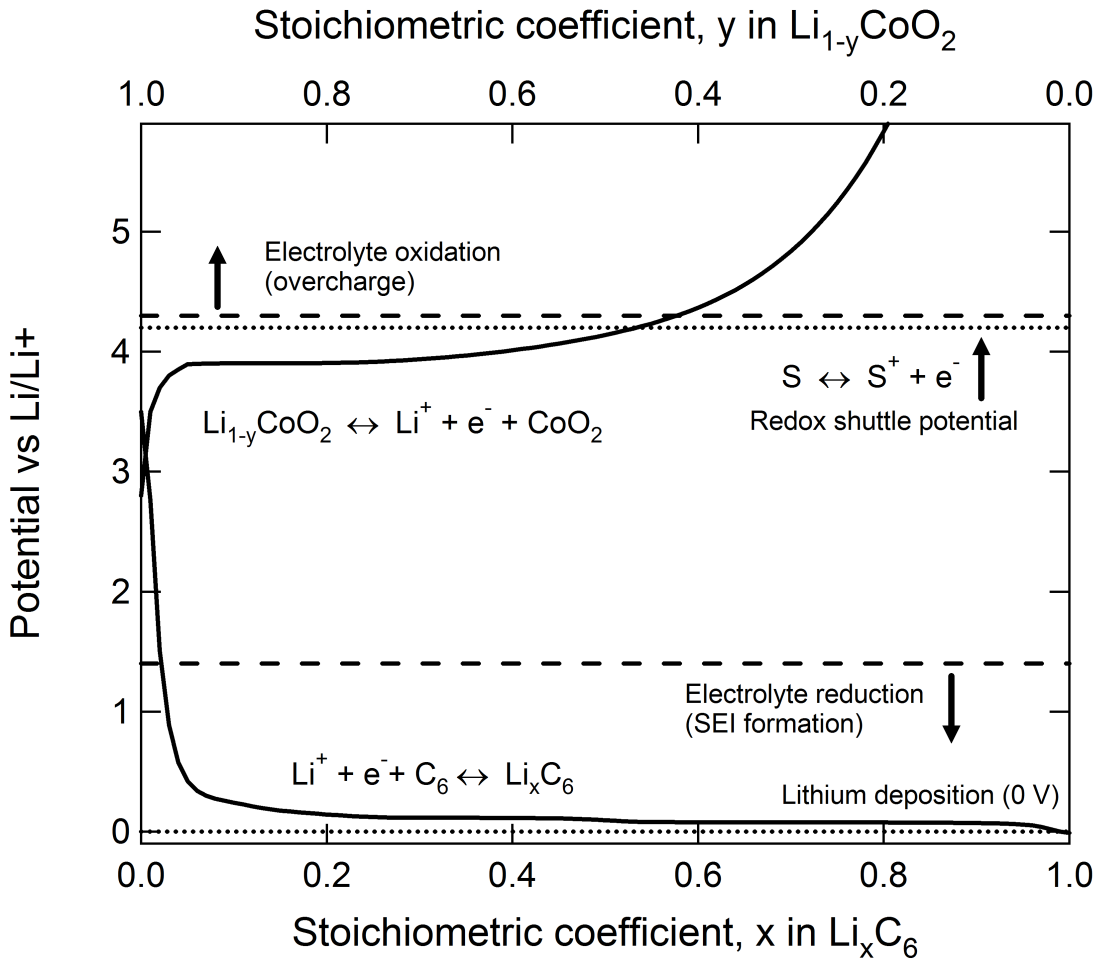

Figure 1.1: Equilibrium potential U of main and side reactions vs. concentration of lithium in the electrodes. The solid lines show the potential of the negative electrode, graphite, and the positive electrode, lithium cobalt oxide. As shown, the concentration moves from left to right on charge. The two dashed lines at 4.3 and 1.5 V show approximate stability limits to the electrolyte. The dotted line at 4.2 shows the operating potential of a redox shuttle, and the dotted line at 0 V is the potential for lithium deposition.

to the positive electrode. Thus, current is passed without removing lithium from the positive electrode. Since shuttles were proposed in the late 1980s, researchers have expended considerable efforts searching for an appropriate molecule [2, 3, 4]. Overcharge protection at appreciable charging rates has been demonstrated for over 200 cycles [5]; however, that redox shuttles have not yet been commercially implemented attests to the difficulty of designing and synthesizing a species that meets the criteria for overcharge protection.

1.3 The solid-electrolyte-interphase (SEI)

Limiting the maximum voltage by choosing an appropriate cutoff potential is an effective strategy for reducing or preventing capacity fade at the positive electrode. At the negative electrode, in contrast, the operating potential of graphite is well-below the thermodynamic stability limit of nonaqueous electrolytes. Fig. 1.1 shows that, below approximately 1.5 V vs. Li/Li^+ , the nonaqueous electrolyte is reduced. Insoluble reduction products precipitate onto the electrode surface and form a passivating film, which is known as the solid-electrolyte-interphase (SEI). In the absence of the SEI, or on an electrode with a "bad" SEI, electrolyte would be continuously reduced, decreasing the current efficiency of the battery and reducing the amount of lithium available for energy storage.

Although the importance of the SEI has been recognized since 1979 [6], its workings remain far from understood. It is considered to be an electronic insulator but an ionic conductor that allows lithium ions through for normal battery operation. Because it is sensitive to air, moisture, and impurities, the SEI is very difficult to characterize. However, researchers have generally agreed that the film has a two-layer structure, with a compact inorganic inner layer 1 to 2 nm thick, and a porous organic outer layer 10 to 100 nm thick [7, 8]. The exact structure and composition depend heavily on the specific electrolyte chemistry and formation conditions, as well as the specific substrate [9]. The works referenced here make up only a few of many, many studies attempting to identify the components of the SEI and their dependence on formation conditions and electrolyte composition. Xu's comprehensive review of nonaqueous electrolytes gives an excellent review of literature on the subject, while Verma et al. provide a more recent summary on the status of SEI knowledge [10, 11].

The mechanisms for the formation and growth of the SEI are even less well understood than its composition and structure. One of the many experimental difficulties associated with studying the SEI is the small rate of reaction. If a 5 Ah cell loses 10% of its capacity in a year, a rough estimate of the current density associated with SEI formation reactions is 3.5×10^{-5} mA/cm^2 of superficial area or 2.9×10^{-7} mA/cm^2 of interfacial area, assuming a superficial area of 0.165 m^2 and an interfacial area of 20 m^2 [12, 13]. This calculation assumes that SEI growth is the only mechanism of capacity fade and thus represents an upper bound on the growth rate. In comparison, at a 2C charge or discharge rate, lithium ions must be able to travel through the same SEI at 6.1 or 0.05 mA/cm^2 of superficial or interfacial area, respectively. Modelers have tried several different approaches to explain the long-term growth rate over time [7, 6, 12, 14, 15]. Capacity-fade measurements suggest that film-growth reactions are transport-limited [13], but whether the transport in question is of electrons from graphite to the film/solution interface [6] or solvent from the solution to the electrode/film interface [12] is unknown.

Successful demonstrations of redox shuttles for overcharge protection present an interesting contradiction in the present understanding of the SEI. The literature shows that shuttles are capable of sustaining overcharge at up to 2.3 mA/cm^2 of superficial electrode area [5]. For the shuttle to carry overcharge current, the cationic shuttle molecule must be reduced at the graphite electrode. Under the previous assumptions of interfacial area, this corresponds

to a rate of 0.02 mA/cm^2 of interfacial area, a factor of 10,000 higher than the SEI growth reaction. Unlike the main intercalation reaction, the shuttle reduction requires either that an electron is transported through the SEI to the cation, or that the cation is transported through the SEI to the electrode/film interface and then back out as a neutral molecule. The disparity between the two reaction rates remains largely unaddressed in redox-shuttle research. If SEI growth is limited by transport of electrons through the film, its growth is determined by the film thickness, electron concentration, and parameters such as the electron diffusivity and vibration frequency [6]. These parameters are independent of the reaction at the film/solution interface. Thus, a model in which either migration or diffusion of electrons from the electrode to the film/solution interface limits SEI growth does not seem to be able to account for the observed selectivity, despite the higher driving force for shuttle reduction. Dahn et al. suggested that the larger driving force for shuttle reduction allows electrons to tunnel to the oxidized shuttle but not to the solvent [16]. While such an explanation accounts for the observed selectivity, electron tunneling is generally confined to short distances of less than 2 nm [17]; thus, a rigorous proof of Dahn's hypothesis would demonstrate an effective SEI thickness much thinner than most measurements have shown. An alternative explanation is selectivity due to transport; if some molecules are much more soluble or mobile in the SEI than others, it is possible for the oxidized shuttle molecule to diffuse to the film/electrode interface, react, and be transported back out at a much higher rate. Although this mechanism seems intuitively less likely, it accounts for the observed selectivity and agrees with present SEI growth models, which consider primarily solvent transport through the SEI [12, 15].

1.4 Outline of chapter contents

This thesis has two parts. In the first part of this thesis, we take advantage of the seemingly contradictory observations about redox shuttles and the SEI to develop a new method of characterizing the SEI using ferrocene, a model redox shuttle. By comparing the kinetic behavior on both a pristine electrode and in the presence of electrolyte reduction products, ferrocene functions as an electrochemical probe that identifies transport and kinetic resistances to reduction.

Chapters 2 and 3 develop a rotating-disk-electrode (RDE) method for ferrocene characterization of the SEI on glassy carbon, a model surface. Unlike graphite or hard carbon, lithium intercalation into glassy carbon is thought to be minimal, meaning that the electrode is effectively inert [18, 19]. Use of an inert electrode minimizes the intercalation reaction, allowing more direct measurements of the film-formation and shuttle-reduction reactions. Another advantage of using glassy carbon is that the structural degradation commonplace with graphite electrodes is avoided [20]. Structural integrity is particularly important for rotating disk techniques, which place mechanical demands on the electrode that are not ordinarily required in lithium-ion batteries. The RDE method separates transport and kinetic resistances to reaction, allowing us to apply a simple model to the through-film ferrocene

reaction. In Chapter 2, we present steady-state experimental data and models to describe the through-film ferrocene current when the SEI is formed potentiostatically at 0.6 V vs. lithium. In Chapter 3, we measure and model the transient response of the through-film ferrocene reaction using electrochemical impedance spectroscopy (EIS).

Although glassy carbon avoids complications with simultaneous formation of the SEI and intercalation of lithium, the literature suggests that the SEI can differ substantially with different substrates [9]. Graphite has an anisotropic structure with edge and basal planes, and the SEI on those planes contains different products and forms at different voltages. Its structure, compared with that of glassy carbon, is shown in Fig. 1.2. Although glassy carbon also contains graphene layers, the layers form ribbons that curl and tangle in an amorphous structure [21]. Highly oriented pyrolytic graphite (HOPG) is a form of graphite

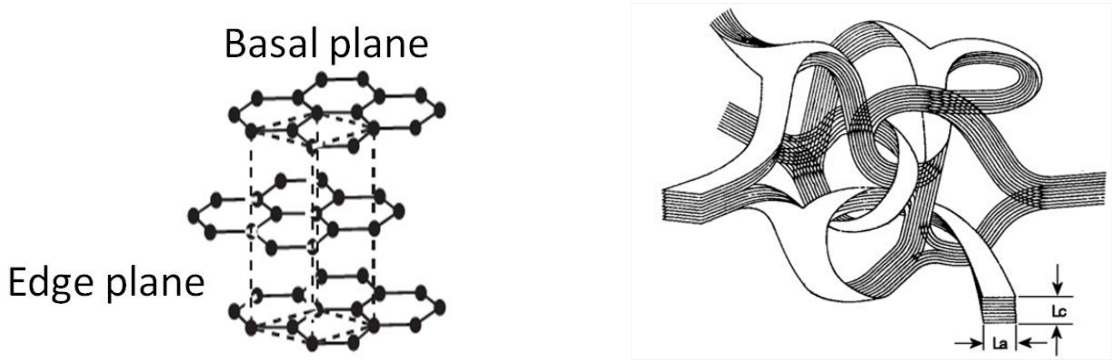

Figure 1.2: Structure of graphite and glassy carbon. Graphite contains crystals of stacked graphene layers, while glassy carbon has an amorphous network of graphite ribbons. Images are taken from Refs. [22] and [21].

with a lamellar structure. Because it can be cleaved in a manner similar to mica, it permits a certain degree of control over the crystal orientation of the surface. In Chapter 4, we extend the ferrocene method to this more realistic system and relate the fraction of exposed edge planes on graphite, f_e, to macroscopic passivation properties of the SEI. We also study the effects of SEI formation voltage and compare behavior in $LiPF_6$-based and $LiClO_4$-based electrolytes.

In Chapter 5, we attempt to obtain nonelectrochemical measurements of SEI formation through in-situ atomic-force microscopy (AFM). Although AFM has been used extensively in previous studies of the SEI, measurements of thickness vary greatly from study to study, and few, if any, previous experiments have reported AFM measurements under potentiostatic conditions. In collaboration with Drs. Robert Kostecki and Ivan Lucas at Lawrence Berkeley National Laboratory, we attempt to validate the results of Chapters 2 and 3 by measuring the evolution of the SEI thickness and morphology during potentiostatic formation at 0.6 V.

In the second part of this thesis, we treat several different overcharge reactions theoretically. Chapter 6 studies the effect of electrode geometry on the lithium deposition reaction. Empirical observations have shown that lithium deposition occurs preferentially at electrode

edges, and that extending the negative electrode beyond the edge of the positive by approximately 1 mm can prevent deposition from occurring. We use a simplified COMSOL Multiphysics model to explain this behavior and to investigate the conditions under which deposition occurs, paying particular attention to the magnitude of edge effects. Chapter 7 examines theoretically the feasibility of redox shuttle overcharge protection by incorporating redox shuttles into an existing cell-sandwich battery model. These simulations predict the effect of redox shuttles on overall cell behavior and suggest how shuttle properties affect tradeoffs between overcharge protection and performance.

Part I

Electrochemical characterization of the solid-electrolyte-interphase using ferrocene

Chapter 2

Steady-state voltammetry on glassy carbon

As described in the introduction, redox shuttles present an apparent inconsistency in current understanding of lithium-ion batteries. If the battery is to operate successfully, electron transfer to the solvent must be prevented by the passivating SEI. If a redox shuttle is to operate successfully, electrons somehow must be transferred through the SEI to the shuttle. In Part I of this thesis, we use this paradox to develop a new method of characterizing the SEI. By measuring the kinetics of a redox shuttle in the presence of passivating films, we directly measure the effect of films on reduction kinetics. Although adding a species to an already-complicated system may seem counterintuitive, measuring the effect of the SEI on the shuttle reaction is actually easier than measuring the effects on lithium intercalation or SEI-formation reactions for several reasons. First, the shuttle is present at a much lower concentration than the solvent or salt. This means that it can be treated as a minor component in supporting electrolyte, and classical electroanalytical techniques can be applied [23, 24]. The shuttle also has a better-defined equilibrium potential than the other reactions, and by choosing a molecule with an appropriate redox potential, complications with simultaneous shuttle, solvent, and lithium reduction can be avoided. Ferrocene is a particularly advantageous choice of molecule because of both its redox potential (approximately 3.25 V vs. Li/Li^+) and the high stability and commercial availability of both the neutral and cationic forms.

By comparing the kinetic behavior on both a pristine electrode and in the presence of electrolyte reduction products, ferrocene functions as an electrochemical probe that identifies transport and kinetic resistances to reduction. In the past, this approach has been successfully applied to the study of electrodes modified with membranes and electrodeposited polymer films [25, 26, 27].

2.1 Experimental method

Electrochemical experiments were performed at room temperature inside an Ar-atmosphere glovebox with oxygen and water content of less than 2 and 5 ppm, respectively. Instrumentation was a VMP potentiostat and RRDE-3A rotating disk system with EC-Lab software (BioLogic). The electrolyte, 1.0 M $LiPF_6$ in 1:1 w/w ethylene carbonate: diethyl carbonate (EC:DEC), was obtained from Novolyte Corporation. Temperature was controlled by pumping 24 L/min of cooling water at 22° C from a circulator (Polyscience) located outside the glovebox through tubes leading to a jacketed glass cell (Biologic) that contained the electrolyte. Because water is a common contaminant in nonaqueous electrochemical systems, both the mechanical integrity of the cooling system and the water content of the glovebox atmosphere were carefully maintained and monitored to prevent leaks. Despite these efforts, ambient glovebox temperature, which ranged from 22 to 30° C depending on factors such as weather and time of day, was found to be a source of error.

The working electrode was a 4 mm diameter glassy-carbon disk embedded in polyetheretherketone (PEEK) resin (Biologic). Unlike graphite or hard carbon, lithium intercalation into glassy carbon is thought to be minimal, meaning that the electrode is effectively inert [18, 19]. Although the literature suggests that the SEI can differ substantially with different substrates [9], use of an inert electrode reduces the intercalation reaction, allowing more direct measurements of the film formation and shuttle reduction reactions. Another advantage of using glassy carbon is that the structural degradation commonplace with graphite electrodes is avoided [20]. Structural integrity is particularly important for rotating disk techniques, which place mechanical demands on the electrode that are not ordinarily required in lithium-ion batteries. The reference electrode was lithium foil.

The working electrode was passivated by a potentiostatic hold at 0.6 V vs. Li/Li^+ for 10 seconds to 120 minutes in approximately 9 mL of electrolyte. The counterelectrode for the passivation hold was also lithium foil. After passivation, 1 mL of electrolyte containing approximately 10 mM ferrocene and ferrocenium hexafluorophosphate (Sigma-Aldrich) was added to the cell, and the lithium counterelectrode was replaced with a platinum mesh. Although only the kinetics of ferrocenium reduction were of interest, including ferrocene in the solution allowed the counterelectrode to run the main reaction in reverse, preventing changes in bulk concentration. Using a platinum mesh of large surface area facilitated ferrocene oxidation instead of lithium plating while voltage was varied and current measured at different electrode rotation speeds. Any imbalance between the ferrocenium reduction and ferrocene oxidation resulted in changes in bulk concentration, which caused a drift in the open circuit potential. Data points exhibiting more than 3 to 4 mV change in open circuit potential between the beginning and end of the experiment were discarded. Reaction between the redox couple and the lithium reference electrode would also cause drift in the measured potential of the working electrode; however, the combined observations of constant open circuit potential and shiny lithium foil suggested that a reactive reference electrode was not a significant source of error. Abraham also found that a ferrocene derivative did not react with lithium foil upon prolonged storage [2].

After passivation, the working electrode was cleaned using a two-step procedure of cycling at high potential and rinsing with dimethyl carbonate (DMC), which has been observed to solubilize SEI components [28, 29]. The electrochemical stripping of surface films has been shown to be an effective method of electrode cleaning [30, 16], and here involved cycling between 2.7 and 4.1 V vs. Li/Li^+ at 100 mV/s and for approximately 10 minutes. After electrochemical cleaning, the electrode was rinsed with DMC (Selectipur, anhydrous) and dried with a lab tissue. A cyclic voltammagram of the test solution was used to diagnose the absence of remaining surface films. If a steady-state current-potential curve at 900 rpm did not exhibit reversible behavior, the cleaning procedure was repeated. The cleaning procedure was developed through trial and error and ultimately judged by its ability to obtain reproducible Q-t curves during film formation. Attempts to clean the electrode by the more traditional method of polishing with diamond or alumina pastes were not particularly successful at obtaining repeatable results. After cleaning, the concentrations of both species were calculated from the slopes of the Koutecký-Levich plots at 2.7 and 3.6 V on the clean electrode.

2.2 Results and discussion

Pristine electrode

A steady-state cyclic voltammagram of 1.2 mM ferrocene/ferrocenium hexafluorophosphate on a glassy-carbon electrode after cleaning is shown in Fig. 2.1. The measured open-circuit potential is 3.233 V, in agreement with the literature [2, 31]. As potential is swept at 10 mV/s from open-circuit, the current increases rapidly until a limiting current is reached at approximately 3.1 V for reduction or 3.35 V for oxidation. The slight difference between the forward and backward sweeps can be attributed to double-layer charging. The Levich equation for limiting current to a rotating disk is

$$i_{\mathrm{lim},i} = 0.62nFD_i^{2/3}\Omega^{1/2}\nu^{-1/6}c_{i,\infty} \tag{2.1}$$

where ν is the kinematic viscosity of the electrolyte and i refers to the oxidized ferrocenium or reduced ferrocene. The concentration at the electrode surface is related to bulk concentration by

$$c_{i,s} = c_{i,\infty}\left(1 - \frac{i_n}{i_{\mathrm{lim},i}}\right) \tag{2.2}$$

With the surface concentration calculated, the equilibrium potential can be determined from the Nernst equation.

$$E_{\mathrm{rev}} = E^0 + \frac{RT}{F}\ln\left(\frac{c_{O,s}}{c_{R,s}}\right) \tag{2.3}$$

In Fig. 2.1, differences between the measured and equilibrium potentials of Eq. 2.3 are negligible, showing that in the absence of surface films, the kinetics is reversible. The sharp

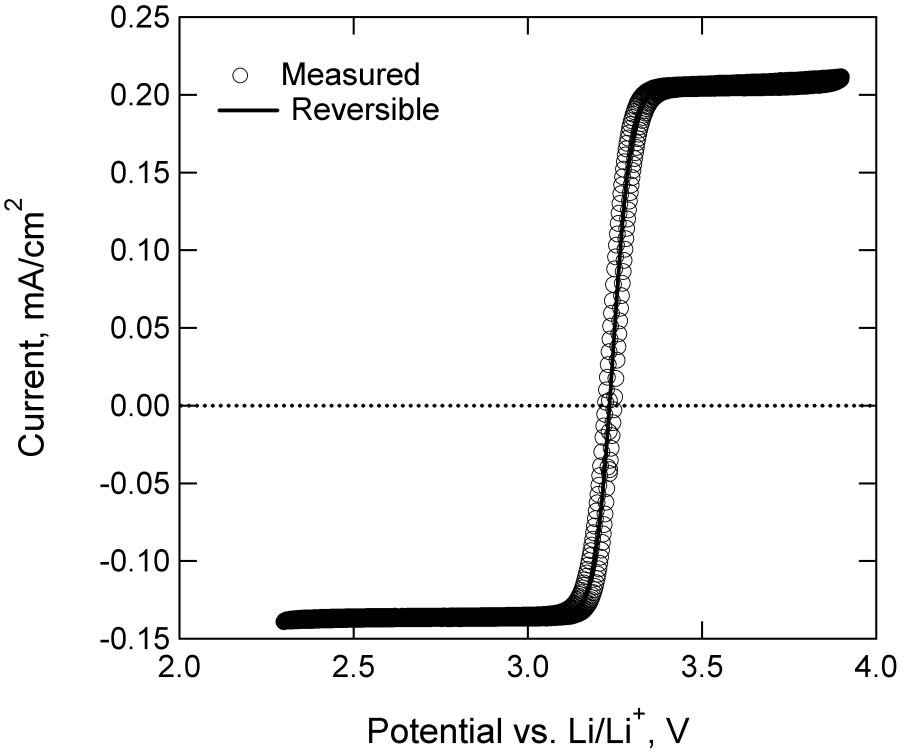

Figure 2.1: Steady-state ferrocene/ferrocenium current on a glassy-carbon electrode after cleaning. The electrolyte contains 1.2 mM of ferrocene/ ferrocenium hexafluorophosphate each. Scan rate = 10 mV/s, rotation speed = 900 rpm. Measured potential and the potential calculated from the Nernst equation agree, showing that kinetics in the absence of films is extremely fast.

transition to the limiting current at potentials ± 150 mV from open circuit is indicative of fast kinetics, which are confirmed by Koutecký-Levich plots generated at 2.7 and 3.6 V. Plotting the inverse of current density i_n versus the inverse of the square root of rotation speed gives a linear relationship:

$$i_n^{-1} = i_{\text{lim}}^{-1} + i_K^{-1} = \left(0.62nFD_i^{2/3}\Omega^{1/2}\nu^{-1/6}c_{i,\infty}\right)^{-1} + i_K^{-1} \tag{2.4}$$

The slope of the line, given a kinematic viscosity of 0.039 cm^2/s [32], shows a bulk ferrocenium diffusivity of $1.28 \pm 0.05 \times 10^{-6}$ cm^2/s, consistent with reported values in similar systems [31]. Taking the inverse of the intercept gives i_K, the current that would be measured if external mass transfer were infinitely fast and the concentration at the surface were equal to the concentration in the bulk. Oxidation of ferrocene was also measured at 3.6 V and yielded a diffusivity of $2.23 \pm 0.13 \times 10^{-6}$ cm^2/s. The best-fit lines in Fig. 2.2 have intercepts of 0.0027 and 0.018 cm^2/mA, which are within error of zero. The negligible intercepts demonstrate that, in the absence of transport limitations, kinetics is too fast to be measured. These

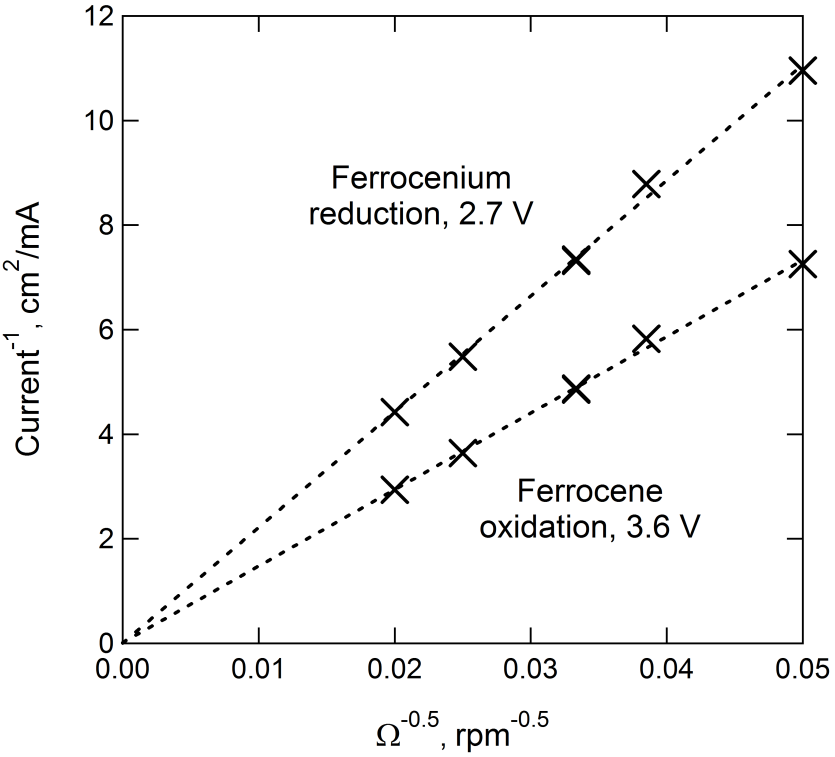

Figure 2.2: Koutecký-Levich plot on a clean electrode for ferrocene oxidation/ ferrocenium reduction. The zero intercept shows that, in the absence of transport limitations, the kinetics is too fast to be measured.

results are consistent with the literature and are, in themselves, not very interesting, but the reversibility of the reaction on a clean electrode means that any changes after holding the electrode at low potential must be due to the presence of passivating films.

Formation of passivating films

The formation of surface films is shown in Figure 2.3. As the electrode is held at 0.6 V vs. Li/Li$^+$, current decays with time (a) because electrolyte reduction products passivate the surface. Fig. 2.3 (b) shows the area under the curve, or total charge passed, versus the time of formation hold. (a) shows three different I-t curves, all from the same day of experiments, while (b) contains data obtained on many different days. In order to demonstrate the range of formation times sampled, (b) shows only the last data point in the series, representing the total charge passed during the formation hold, whereas (a) shows data points as they are measured by the potentiostat throughout the experiment. Scatter is higher at longer times because error accumulates throughout the formation hold, and is likely caused by temperature fluctuations in the glovebox and imperfections in the electrode cleaning proce-

dure. Despite the existence of outliers, the overall consistency of the data in Fig. 2.3 shows reasonable reproducibility and proves the efficacy of the cleaning method.

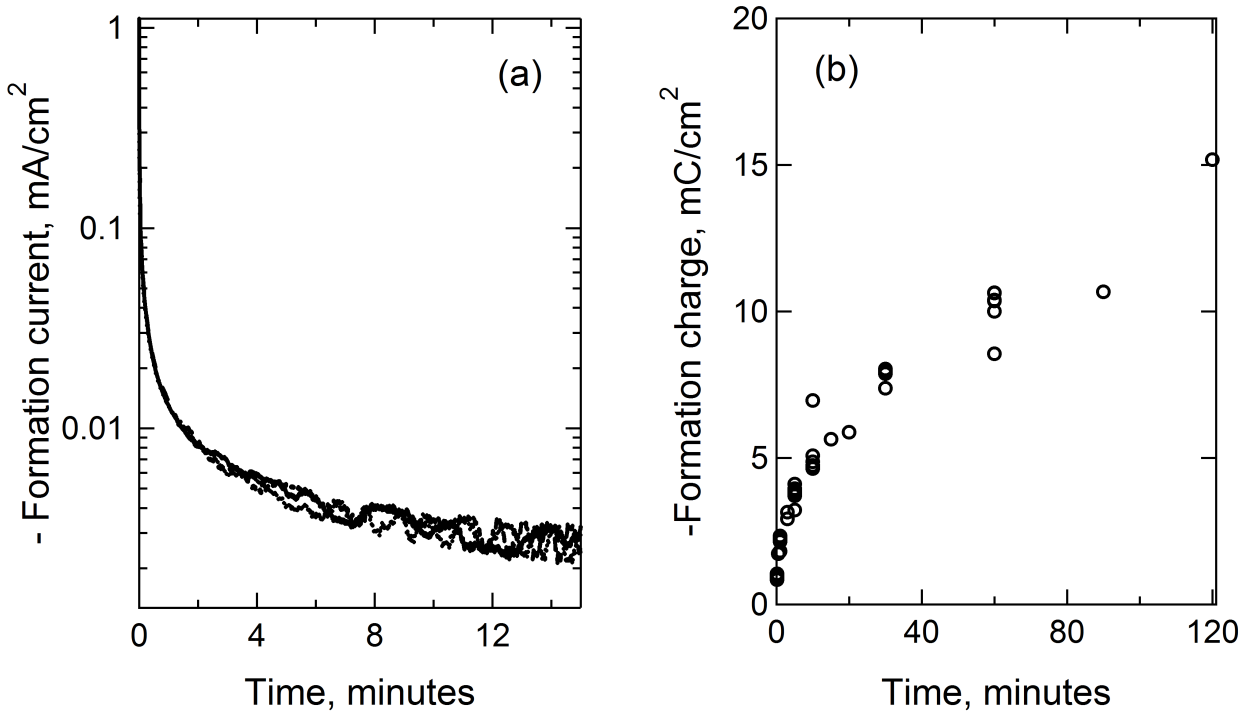

Figure 2.3: Film formation at 0.6 V in EC:DEC 1.0 M $LiPF_6$. Solution does not contain ferrocene/ferrocenium. (a) Current during film formation holds collapses among different trials, showing good reproducibility. (b) Integrating current for total film-formation charge shows reasonable day-to-day reproducibility, although some outliers exist. In order to demonstrate the range of formation times sampled, (b) shows only the total charge passed or the last data point. For a discussion of scatter, see the text.

Because the formation solution does not contain ferrocene or ferrocenium, all current passed should go to SEI-formation reactions; thus, the charge should give a rough measurement of the film thickness by

$$-Q = \frac{F\rho L}{M} \tag{2.5}$$

where M is equivalent weight and ρ the density of products. If the electrolyte reduction product is assumed to be lithium ethylene dicarbonate (LiEDC) with a density of 2.1 g/cm^3 [33] [34] [35], a formation charge of 10 mC/cm^2 corresponds to a film thickness of approximately 50 nm. If the properties of lithium carbonate are used, the calculated thickness for the same amount of charge is approximately 18 nm. Neither calculation takes into account any effects of porosity or inhomogeneities in the film, nor the possiblity of reactive intermediates which diffuse away from the electrode. Finally, while this work, like Refs. [18] and

[19], takes the view that lithium intercalation into the glassy carbon electrode is negligible, its possibility cannot be ruled out completely. Sleigh et al. cycled glassy carbon and found that intercalation capacity was smaller than that of both hard carbon and carbon black [36]. Carbon black is commonly used as a conductive additive in both anodes and cathodes of lithium ion batteries, and its contribution to electrode capacity is rarely reported in battery literature. Any intercalation would decrease the current efficiency of film-formation reactions, making the thickness estimated by Eq. 2.5 too high and possibly affecting the electrochemical behavior of the surface.

Because of the complications described above, the correlation from Eq. 2.5 gives only a very rough estimate of film thickness. Additionally, all passivation holds were performed at 0.6 V vs. Li/Li^+, which is higher than the operating potential of graphite at 0.1 to 0.0 V vs. Li/Li^+. 0.6 V was chosen as a moderate value between the operating potential of graphite and the the beginning of SEI formation reactions at 1.2 to 1.5 V [37, 38]. The properties of the SEI have been found to depend strongly on the potential at which it is formed [39]; thus, this study does not exactly simulate conditions inside a commercial battery although the electrolyte studied is directly relevant.

Ferrocene reduction on passivated electrodes

Steady-state current-potential curves after 10 minutes of passivation are shown in Fig 2.4. Comparison to the pristine-electrode current in Fig. 2.1 shows that the kinetics has changed greatly. Instead of sharply varying from zero at 3.233 V to the limiting current at 3.1 V, the negative current first increases rapidly between open circuit and 3.2 V, then slopes gradually as potential decreases from 3.2 to 2.1 V. The shape of the curve is more obvious at higher rotation speeds. Data were taken at rotation speeds of 900, 2500, 1600, 400, 675, and 900 rpm, in that order. The minimal difference between the two measurements at 900 rpm shows that the system is at steady state and that rotation does not mechanically remove reduction products from the surface. The family of curves follows the expected trend with rotation speed; this is also shown in the linearity of Koutecký-Levich plots in Fig. 2.5. Except in the region of low overpotential, where the slope is affected by the concentrations of both the oxidized and reduced species, the slopes do not vary with potential, showing that the presence of the film does not affect transport from the bulk solution to the electrode surface. The intercept i_K^{-1}, which is negligible on the clean electrode, increases in the presence of surface films, confirming that the kinetics is no longer reversible.

Plotting the reciprocal of the intercept, or the kinetic current i_K, gives a current-potential curve such as those shown in Fig. 2.6. Curves generated after passivation holds of 10, 30, and 60 minutes are shown. For all three curves, the linear region between 3.1 and 2.8 V vs. lithium suggests Tafel kinetics, but the bend in the curve at very negative overpotential suggests a limiting current. Because the current in Fig. 2.6 is the extrapolated kinetic current i_K, any transport limitations must be due to transport of electrons or ferrocenium through the film, not transport from the bulk solution to the surface. These observations can be described by a simple model that combines Butler-Volmer kinetics with a through-

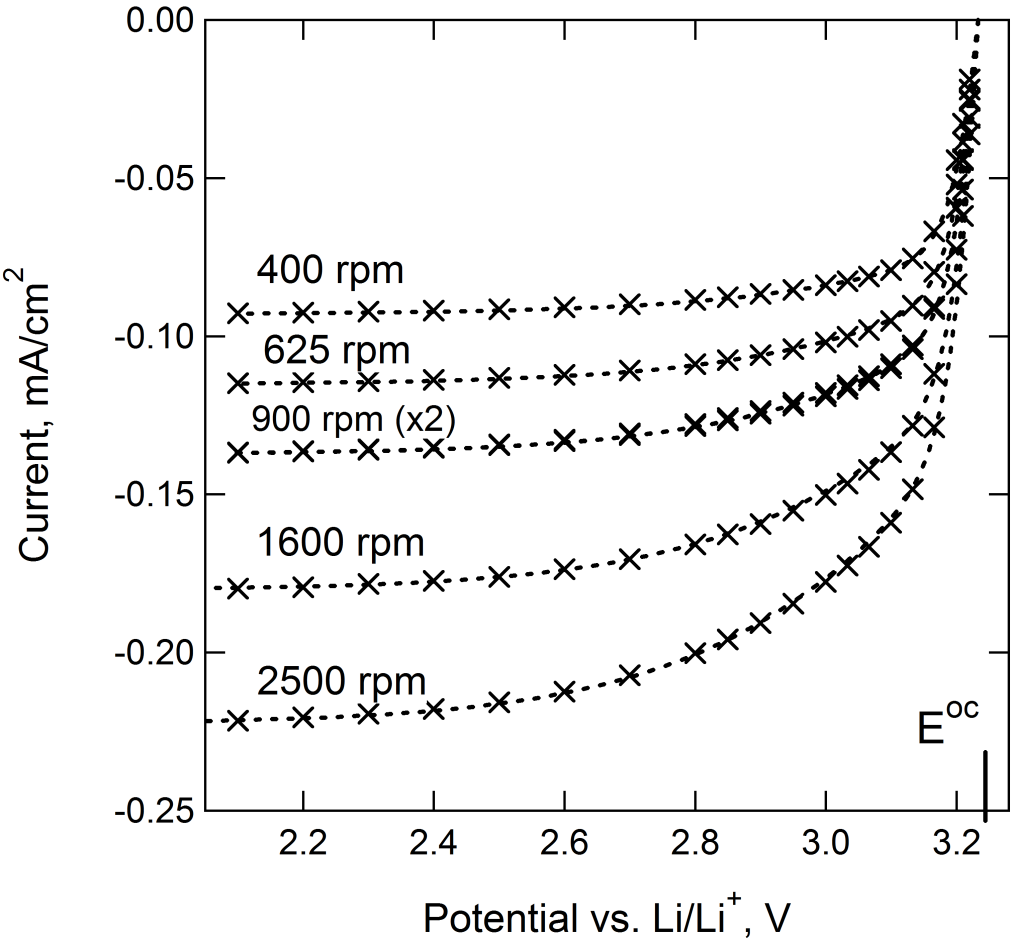

Figure 2.4: Ferrocenium reduction on a glassy-carbon electrode after a 10 minute formation hold at 0.6 V. Markers are measurements, dashed lines are model fits with α_a=0.89, $k = 2.65 \times 10^{-3}$ cm/s, and $i_{\mathrm{lim},f} = -3.7$ mA/cm^2. The solution contains 1.2/1.3 mM ferrocene/ferrocenium, and the open circuit potential is 3.233 V.

film limiting current to describe i_K as a function of V. The surface concentration is now determined by

$$c_{i,s} = c_{i,\infty}\left(1 - \frac{i_K}{i_{\mathrm{lim},f}}\right) \tag{2.6}$$

To fit the raw current measurements i_n instead of the manipulated i_K, Eq. 2.2 can be used with one effective limiting current,

$$i_{\mathrm{lim}}^{-1} = i_{\mathrm{lim},\infty}^{-1} + i_{\mathrm{lim},f}^{-1} \tag{2.7}$$

where $i_{\mathrm{lim},\infty}$ is given by the Levich equation, Eq. 2.1. At the surface, the exchange current density i_0 is calculated by assuming both a transfer coefficient α_a and an effective rate

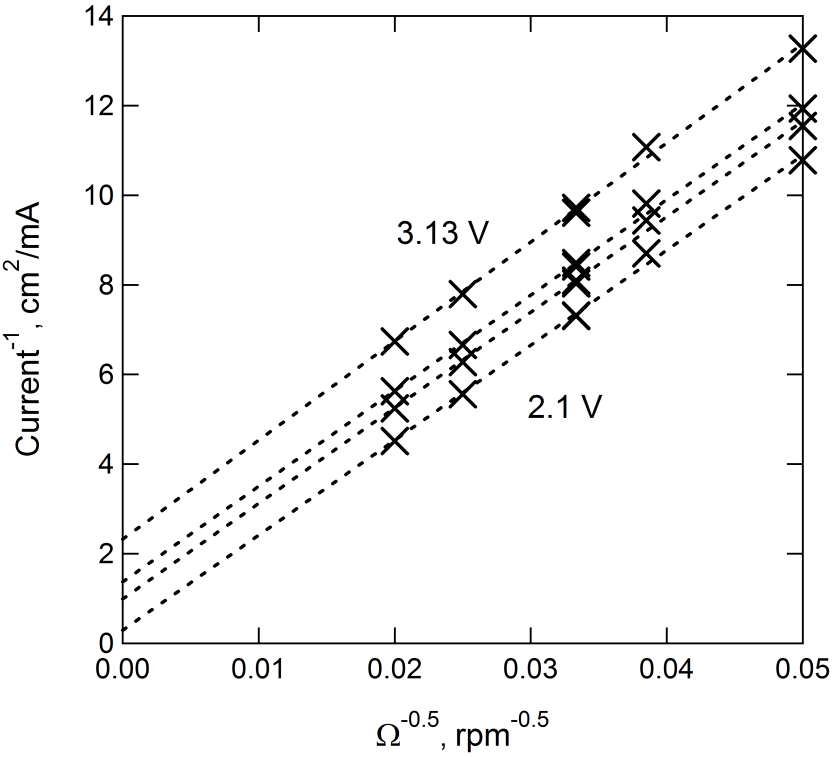

Figure 2.5: Koutecký-Levich plot on a glassy-carbon electrode after a 10 minute hold at 0.6 V. Data are taken from Fig. 2.4 at 2.1, 2.9, 3, and 3.13 V. The intercepts are no longer zero, and depend on potential, showing that the presence of electrolyte reduction products inhibits the ferrocenium reduction.

constant k_{eff}

$$i_0 = k_{\text{eff}} F c_{R,s}^{\alpha_a} c_{O,s}^{1-\alpha_a} \tag{2.8}$$

Eq. 2.8 assumes that the transfer coefficients α_a and α_c sum to unity. For multi-step electrochemical reactions such as the formation of the SEI, this assumption may be incorrect. However, the reaction modeled here is the ferrocene/ferrocenium couple, which has repeatedly been demonstrated to exhibit simple one-electron behavior consistent with the above treatment [31, 40, 41]. Accordingly, model development proceeds assuming that $\alpha_c = 1 - \alpha_a$. The surface overpotential or kinetic loss η_s is found by solving the equation

$$\frac{i_K}{i_0} = \exp\left(\frac{\alpha_a F}{RT}\eta_s\right) - \exp\left(-\frac{(1-\alpha_a)F}{RT}\eta_s\right) \tag{2.9}$$

The total calculated potential $V_{\text{tot}} = E_{\text{rev}} + \eta_s$ can be plotted against measured data to find the best fit for k_{eff} and α_a.

As shown in Fig. 2.6, the simple model approximates the measurements extremely well. Because the open-circuit potential is measured and the bulk concentrations are known, α_a,

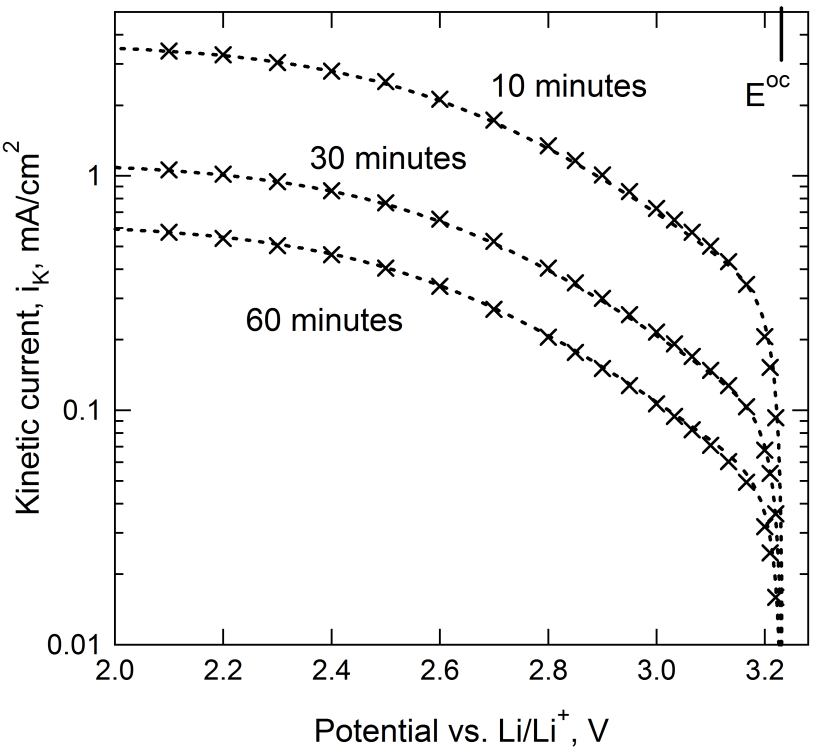

Figure 2.6: Kinetic current i_K-potential curves on a glassy-carbon electrode after different lengths of passivation time at 0.6 V. Markers are measurements, dashed lines are model fits with α_a=0.89, k=2.65, 0.85, and 0.45 $\times 10^{-3}$cm/s, and $i_{\mathrm{lim},f}$=-3.7, -1.15, and -0.63 mA/cm^2 for 10, 30, and 60 minute formation holds. The solution contains 1.2/1.3 mM ferrocene/ferrocenium, and the open circuit potential is 3.233 V.

k_{eff}, and $i_{\mathrm{lim},f}$ form the only independent fitting parameters for the system of equations. Each parameter affects the curve uniquely: α_a gives the slope of the Tafel region, k_{eff} affects its intercept, and $i_{\mathrm{lim},f}$ is the asymptotic limit of i_K at very negative values of η_s. $i_{\mathrm{lim},f}$ refers to a through-film limiting current for ferrocenium reduction. The through-film limiting ferrocene oxidation current is also needed for calculation of $c_{O,s}$ and may not be exactly the same as that for reduction. However, model fits depend little on the value of the oxidation current because measurements are taken either near equilibrium or at highly negative overpotentials; thus, assuming that $i_{\mathrm{lim},f,O}$ = -$i_{\mathrm{lim},f,R}$ introduces neglible error in the model. Incorporating the effects of bulk mass transfer using Eq. 2.7 in Fig. 2.4 shows that the simple model can also provide an excellent fit to raw data without changing any of the fitting parameters.

Holding the electrode at 0.6 V for a longer period of time should increase the thickness of the film, as shown by Eq. 2.5. Intuition says that an increased film thickness should cause the through-film limiting current to decrease, while the kinetic rate constant should remain unaffected. The results of these experiments are shown in Fig. 2.6. Comparing i_K

currents obtained after 10, 30, and 60 minute holds shows that as the time of formation hold increases, the slope of the Tafel region remains constant, but both the intercept of the Tafel region and the limiting current decrease. This result is shown again in Fig. 2.7, which plots k_{eff} from Eq 2.16 and and $i_{\text{lim},f}$, normalized for concentration, versus charge passed during film formation. The best-fit value of α_a varies between 0.88 and 0.91 for all data points and is not shown.

The best-fit values of $i_{\text{lim},f}$, k_{eff}, and α_a were evaluated visually, and it is estimated that values $\pm$ 5% of those reported cause a visible divergence between the model and measured data. While a more sophisticated fitting scheme would provide quantitative error of each parameter, the excellent fits shown in Figs. 2.6 and 2.4, the unique effect of each parameter on the fits, and the scatter seen in Fig. 2.3 suggest that the primary source of variation in Fig. 2.7 does comes not from the analysis and curve fitting. The scatter in Fig. 2.3 reflects variation in the film-formation process, which in turn affects the parameters measured by the method. Temperature was also found to have an enormous influence on steady-state i-V measurements such as those in Fig. 2.4. In addition to day-to-day variation in glovebox temperature, temperature increased throughout the day as friction between the rotating electrode shaft and electrical contact brushes generated heat. Rough measurements of the surface temperature suggested that for the same film (i.e., one data point in Fig. 2.3 (b)), an increase of 1° C caused the best-fit value of both $i_{\text{lim},f}$ and k_{eff} to increase by a factor of three to five. α_a did not vary with temperature. Using a jacketed cell and allowing a cool-down period between measurements was helpful for controlling temperature, but the extreme sensitivity of the method and the impossibility of measuring precisely the surface temperature of the submerged rotating electrode made compensating for this source of error extremely difficult.

In order to relate the values of α_a, k_{eff}, and $i_{\text{lim},f}$ to a passivation mechanism, a physical model is required. A schematic of the proposed SEI model is shown in Fig. 2.8. For clarity, only the concentration profile of oxidized ferrocenium is shown. Based on Refs. [7] and [8], the film is assumed to have a two-layer structure. The inner layer is compact, of thickness l, and thin enough for electron tunneling. It corresponds to the inorganic layer reported in the literature and is assumed to grow very quickly to a thickness that is limited by the range of electron tunneling (a few nanometers). Thus, the thickness of the compact layer does not vary in our model. The outer layer is a two-phase structure of impermeable solids and electrolyte-filled voids, electronically insulating but porous enough for ferrocenium cations and neutral ferrocene to diffuse across the thickness, L. All reaction is assumed to occur at the compact layer/porous layer interface as electrons tunnel through the compact layer and ferrocene diffuses through the porous layer. Reaction occurs at the same interface during SEI formation, when the reactant is ethylene carbonate instead of the redox couple. This two-layer growth mechanism is consistent with the mixed-control model of SEI growth suggested by [15] and requires modification of Eq. 2.5 so that

$$-Q = \frac{F\rho_p L}{M_p(1-\epsilon)} + \frac{F\rho_c l}{M_c} \tag{2.10}$$

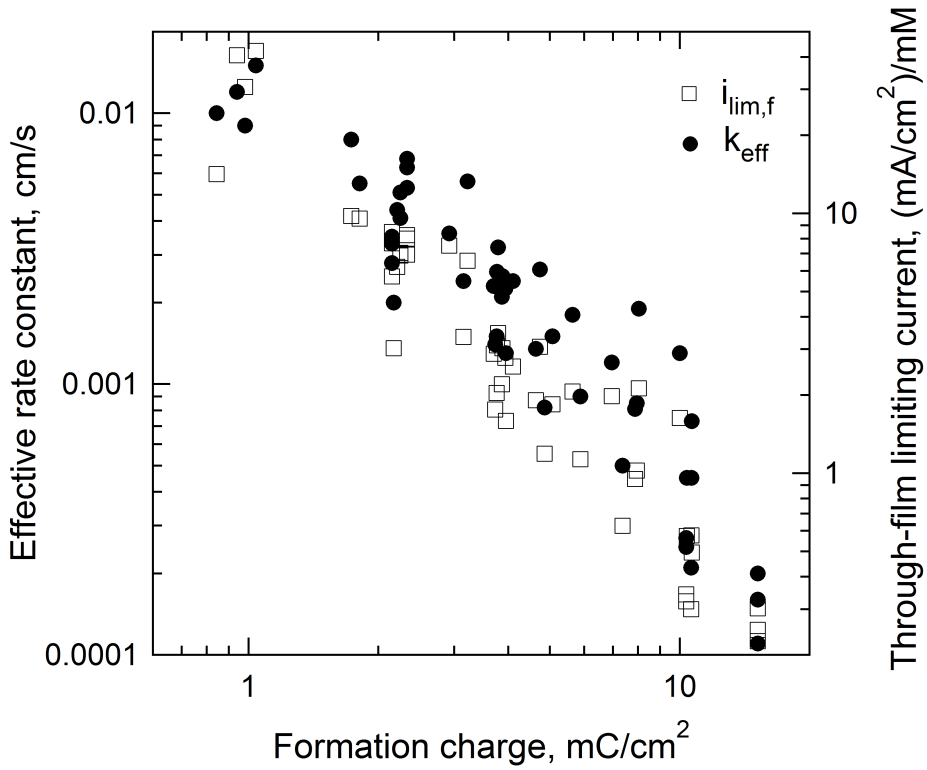

Figure 2.7: The apparent rate constant $k_{\text{eff}} = k\epsilon$ and through-film limiting current given by Eq. 2.13 decrease with increasing passivation time, possibly because of a decreasing porosity in addition to or instead of increasing thickness. The limiting current is normalized for the concentration of ferrocenium by dividing by the bulk concentration $c_{O,\infty}$.

where the subscripts p and c refer to the porous and compact layers and ϵ is the void fraction or porosity of the porous layer.

The superficial concentration at the compact/porous layer interface is $c_{i,s}$ and affects the exchange current density in Eq. 2.8. The concentration at the film/solution interface is $c_{i,f}$ on the film side and $c_{i,b}$ on the solution side. When the measured current i_n is extrapolated to the Koutecký-Levich intercept i_K, $c_{i,b} = c_{i,\infty}$. At finite rotation speeds, $c_{i,b}$ is related to the known bulk concentration $c_{i,\infty}$ by Eq. 2.2. Because the two shuttle species are present in the bulk solution at less than 2 mM, the electrolyte in the pores is treated as a supporting electrolyte, and migration effects on the ferrocene cation are neglected. This assumption greatly simplifies the governing equations.

At steady-state, all fluxes must be constant and proportional to current by Faraday's law. Thus, in the porous layer

$$\frac{i_n}{F} = -\frac{D_{R,f}\left(c_{R,s} - c_{R,f}\right)}{L} = \frac{D_{O,f}\left(c_{O,s} - c_{O,f}\right)}{L} \tag{2.11}$$

$D_{i,f}$ is an effective diffusivity inside the film, equal to D_i/τ, where τ is the tortuosity [23].

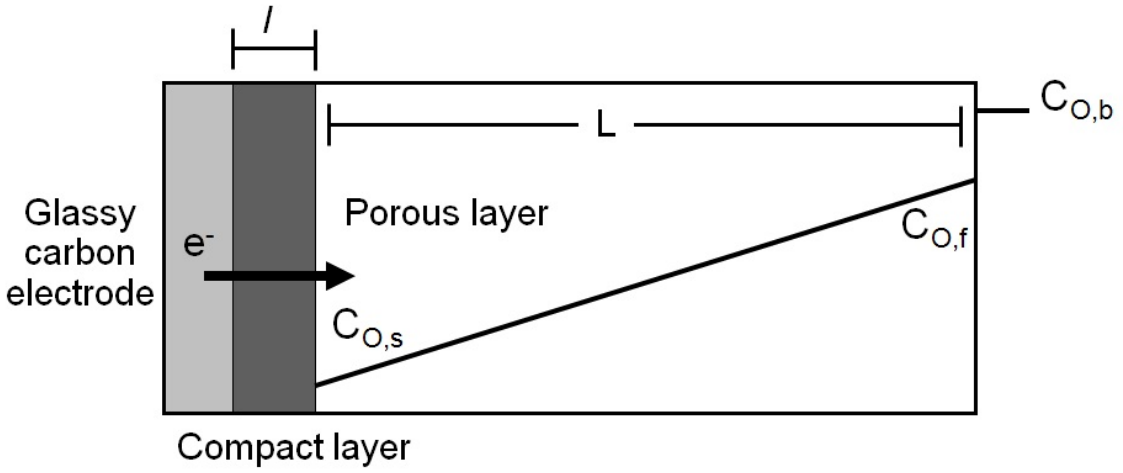

Figure 2.8: Schematic of simple two-layer SEI model with ferrocenium concentration profile. Electrons can tunnel across the inner compact layer to react with ferrocenium at concentration $c_{O,s}$. Transport through the porous layer is governed by Fickian diffusion. At the outer interface, concentrations inside and outside the film are related by $c_{O,f} = \epsilon c_{O,b}$, where both of the concentrations are measured with respect to superficial, not in-pore, area. When the measured current i_n is extrapolated to the Koutecký-Levich intercept i_K, $c_{i,b} = c_{i,\infty}$. At finite rotation speeds, $c_{i,b}$ is related to the known bulk concentration $c_{i,\infty}$ by Eq. 2.2.

At the film/solution interface, concentrations are governed by interfacial mass transfer:

$$\frac{i_n}{F} = -k_{mt,R}\left(c_{R,f} - \epsilon c_{R,b}\right) = k_{mt,O}\left(c_{O,f} - \epsilon c_{O,b}\right) \tag{2.12}$$

$k_{mt,i}$ is a mass-transfer coefficient. Because the volume fraction of electrolyte inside the film is less than unity, $\epsilon c_{O,b}$ gives the highest possible superficial concentration of ferrocenium inside the film. If the film is of a polymeric nature instead of a two-phase structure, then ϵ is replaced by K_{eq}, a thermodynamic partition coefficient that gives the ratio of concentrations inside and outside the film at equilibrium. Combining Eqs. 2.11 and 2.12 yields a through-film limiting reduction current of

$$i_{\mathrm{lim},f} = -\frac{F\epsilon c_{O,b}}{\frac{L}{D_{O,f}} + \frac{1}{k_{mt}}} \tag{2.13}$$

If ferrocene and ferrocenium have different in-film diffusion coefficients or mass-transfer coefficients, the through-film limiting current may be different for oxidation and reduction. However, as previously discussed, assuming that $i_{\mathrm{lim},f,O}$ = -$i_{\mathrm{lim},f,R}$ introduces neglible error in the model.

At the film/electrode interface, charge transfer is governed by Butler-Volmer kinetics. Rewriting Eq. 2.9 to consider more precisely the physical significance of k_{eff} used to fit the

data gives

$$\frac{i_n}{F} = k_a c_{R,s} \exp\left(\frac{\alpha_a F}{RT}\Delta\Phi\right) - k_c c_{O,s} \exp\left(-\frac{(1-\alpha_a)F}{RT}\Delta\Phi\right) \tag{2.14}$$

$\Delta\Phi$ is the potential difference across the electrode/film interface. k_a and k_c are forward and backward rate constants determined by the energetics of the ferrocene/ferrocenium couple. In the absence of current, no concentration gradients exist, and the surface concentration is the equilibrium concentration, ϵc_b. Solving for $\Delta\Phi$ at equilibrium in the presence of a film gives

$$E_{\text{rev},f} = \frac{RT}{F} \ln\left(\frac{k_c c_{O,s}}{k_a c_{R,s}}\right) \tag{2.15}$$

Comparison with Eq. 2.3 shows that $E^0 = RT/F \ln(k_c/k_a)$; thus, any difference between k_c/k_a in the presence and absence of a film will cause the open-circuit potential to change. The equilibrium potential, which is determined by the thermodynamics of the ferrocene /ferrocenium couple, should be independent of any specific kinetics at the electrode surface. Experimentally, no change in the open-circuit potential before and after cleaning the electrode was observed.

Further manipulation to make Eq. 2.14 consistent with Eqs. 2.9 and 2.6 gives

$$i_0 = F(k_a \epsilon c_{R,s})^{(1-\alpha_a)} (k_c \epsilon c_{O,s})^{\alpha_a} = F\epsilon k c_{R,s}^{(1-\alpha_c)} c_{O,s}^{\alpha_a} \tag{2.16}$$

where $k = k_a^{1-\alpha_a} k_a^{1-\alpha_a}$. Figs. 2.1 and 2.2 show that, in the absence of passivating films, k is too large to measure by the methods presented here. However, the presence of the compact SEI layer should increase the energy barrier of the reaction and decrease k. The k_{eff} in Eq. 2.8 is thus equal to the quantity ϵk, where k is the kinetic rate constant in the presence of the compact layer.

Eqs. 2.16 and 2.13 provide physical meanings for the fitting parameters used in the model. The development of a physical model replaces two unique fitting parameters (k_{eff} and $i_{\text{lim},f}$) with five physical properties ($D_{O,f}$ or τ, $k_{mt,O}$, ϵ, L, and k). Although multiple combinations of these may be used to obtain the same values of k_{eff} and $i_{\text{lim},f}$, the dependence of k_{eff} and $i_{\text{lim},f}$ on the film charge places constraints on the range of values and can suggest an overall mechanism limiting ferrocenium reduction. Fig. 2.7 shows that $i_{\text{lim},f}$ decreases as more charge is passed to film-forming reactions. Because the rate constant of partitioning at the film/electrolyte interface should not depend on the thickness of the film, Fig. 2.7 suggests that k_{mt} is large in comparison to $L/D_{O,f}$, i.e. partitioning into the film is not limiting. Fig. 2.7 also shows that k_{eff} decreases with a thicker film. The rate constant k should not be affected by the thickness of the porous film, but k_{eff} includes the factor of porosity, which may decrease with longer film-formation holds. A lower porosity with longer formation time thus explains the trend of both parameters. The similar slopes of k_{eff} and $i_{\text{lim},f}$ in Fig. 2.7 suggest, but do not ensure, that the same physical phenomenon causes both parameters to decrease.

The above analysis treated $c_{i,s}$ as a superficial concentration. Alternatively, the model can be developed using in-pore concentrations to find the same result. If this approach is

taken, Eqs. 2.11 and 2.14 still apply. However, Eqs. 2.12 and 2.16 are modifed so that

$$\frac{i_n}{F} = -k_{mt,R}\left(c_{R,f} - c_{R,b}\right) = k_{mt,O}\left(c_{O,f} - c_{O,b}\right) \tag{2.17}$$

and

$$i_0 = F(k_a c_{R,s})^{(1-\alpha_a)}(k_c c_{O,s})^{\alpha_a} = F k c_{R,s}^{(1-\alpha_c)} c_{O,s}^{\alpha_a} \tag{2.18}$$

The porosity affects the total flux by

$$N_{\text{superficial}} = \epsilon N_{\text{in-pore}}; \tag{2.19}$$

thus, the porosity can also be thought of as the the area fraction of electrode that is not blocked by the inert film. Finally, the above analysis was developed for a two-layer film with a coherent compact layer. An alternative physical model to Fig. 2.8 treats the diffuse layer not with a homogenous porosity, but as a completely blocking layer with a number of cracks or active sites to which ferrocene can diffuse. Depending on the values of different constants and method of measurement, these two interpretations (the "membrane" and "pinhole" models, respectively) may not be exactly equivalent, but the mathematics is indistinguishable. Savéant has discussed this problem [42].

2.3 Conclusions

The present experiments show that ferrocene kinetics is inhibited in the presence of passivating films on a glassy-carbon electrode. Using a rotating disk electrode permits steady-state measurements and the application of simple models to describe the data. Our results show that the through-film ferrocenium reduction current can be described by simple Butler-Volmer kinetics combined with a limiting current. Both the exchange current density and through-film limiting current decrease with more passivation time; this observation can be explained by a decreasing porosity. More work is required to prove conclusively the mechanism of passivation and to expand the method developed here to conditions that more realistically simulate those in a lithium battery.

Chapter 3

Transient voltammetry on glassy carbon

The previous chapter developed and applied a technique to characterize the SEI using ferrocene and rotating-disk-electrode voltammetry. Measuring ferrocenium reduction kinetics in the presence and absence of passivating films reveals the electrochemical effects of the SEI, not just physical characteristics such as composition or morphology. The ferrocenium reduction current was described by simple Butler-Volmer kinetics combined with a through-film limiting current, and as the amount of passivation time increased, the limiting current and the exchange current density also decreased. By developing a simple model of the through-film reduction, these observations were explained qualitatively by a decrease in the film porosity. However, because the model replaced the two unique fitting parameters of exchange current density and limiting current with multiple physical properties such as thickness, porosity, and tortuosity, a more quantitative measurement of the properties was not possible.

This chapter attempts to verify qualitatively the results of Chapter 4 and to relate quantitatively the steady-state fitting parameters to physical constants using two different methods. First, the steady-state analysis is expanded to model the frequency response of the system and compared to electrochemical impedance spectroscopy (EIS) measurements. Secondly, the transient open-circuit potential as ferrocene and ferrocenium are introduced into the cell is measured and described by a simple model to provide a separate estimation of the film time constant.

3.1 Experimental method

Electrochemical experiments were performed using a VMP potentiostat, RRDE-3A rotating disk electrode, and temperature-control system as described in the previous chapter. The electrolyte was 1:1 weight ethylene carbonate : diethyl carbonate with 1.0 M $LiPF_6$ (Novolyte). The working electrode was glassy carbon (Biologic/ALS), and the reference electrode was lithium foil. Three different working electrodes were used to compare the

difference between glassy carbon samples. The working electrode was passivated by a potentiostatic hold at 0.6 V vs. Li/Li^+ in 8 mL of electrolyte for different lengths of time. The counterelectrode for the passivation hold was also lithium foil. After passivation, 1 mL of electrolyte containing approximately 10 mM ferrocene and ferrocenium hexafluorophosphate (Sigma-Aldrich) was added to the cell, and the open-circuit potential monitored while rotating the electrode at 900 rpm. After steady-state was reached, the lithium counterelectrode was replaced with a platinum mesh, and the impedance and steady-state reduction kinetics were measured. After passivation, the working electrode was cleaned with a two-step process of cycling at high voltage (2.7 to 4.1 V vs. Li/Li^+) and rinsing with dimethyl carbonate (DMC). After cleaning, the concentrations of both species were calculated from the slopes of the Koutecký-Levich plots at 2.7 and 3.6 V on the clean electrode.

3.2 Model development

Previous steady-state model

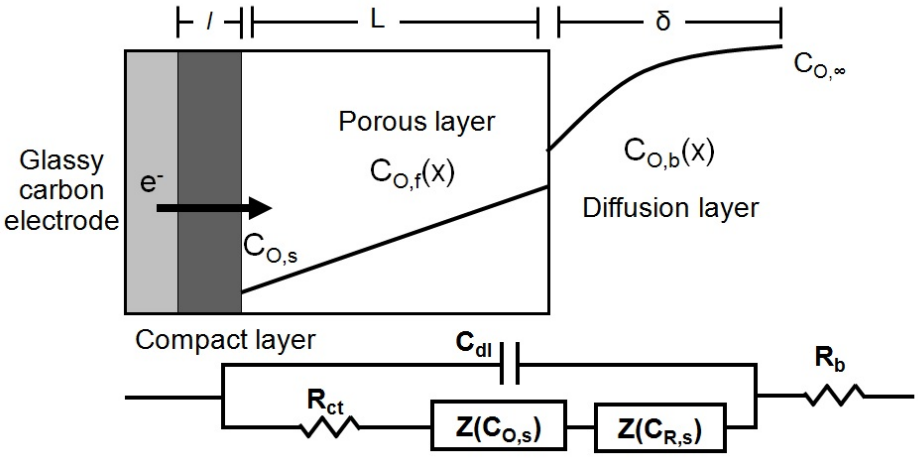

Figure 3.1: Model schematic showing the diffusion layer, porous layer, and compact layer. For clarity, only the concentration profile of oxidized ferrocenium is shown. The circuit representing the impedance model derived in Section 3.2 is also shown. Although $R_{f,c}$ and $R_{f,p}$ are shown to represent ohmic resistance in the compact and porous layers, both resistances are considered negligible. Elimination of these two resistances reduces the model to Eqs. 3.13 and 3.20.

A schematic of the proposed SEI model is shown in Fig. 3.1. Based on Refs. [7] and [8], the film is assumed to have a two-layer structure. For clarity, only the steady-state concentration profiles of oxidized ferrocenium, $\bar{c}_{O,f}(x)$ and $\bar{c}_O(x)$, are shown in the film and solution,

respectively. $c_{i,f}$ is an in-pore concentration while the overbar denotes a steady-state quantity. Outside the film, the bulk diffusion layer extends to thickness $\delta_i = 1.61 D_i^{1/3} \Omega^{-1/2} \nu^{1/6}$ if the electrode rotates at speed Ω. If the electrode is stationary and free convection is ignored, the bulk diffusion layer is infinitely thick. The film is assumed to have a two-layer structure. The inner layer is compact, of thickness l, and ionically conductive to Li^+. Although it is electronically insulating, the layer is thin enough for electron tunneling. The outer layer is electronically insulating, but has a porosity ϵ large enough for Li^+, PF_6^-, ferrocenium cations, and neutral ferrocene to diffuse across the thickness, L. The concentration at the compact/ porous film interface is $\bar{c}_{i,f}(0) = \bar{c}_{i,s}$. All reaction is assumed to occur at this interface, where it is governed by Butler Volmer kinetics,

$$\bar{i}_{\text{far}} = i_0 \left[\frac{\bar{c}_{R,s}}{c_{R,\infty}} \exp\left(\frac{\alpha_a F}{RT} \bar{\eta} \right) - \frac{\bar{c}_{O,s}}{c_{O,\infty}} \exp\left(-\frac{(1-\alpha_a) F}{RT} \bar{\eta} \right) \right] \tag{3.1}$$

where

$$i_0 = F k_{\text{eff}} \bar{c}_{R,\infty}^{\alpha_c} \bar{c}_{O,\infty}^{\alpha_a} = F k_0 \epsilon \bar{c}_{R,\infty}^{\alpha_c} \bar{c}_{O,\infty}^{\alpha_a} \tag{3.2}$$

k_{eff} is the effective rate constant and $\bar{\eta}$ is the total overpotential, given by $\bar{\eta} = V - E^{OC}$. The factor of ϵ relates the in-pore concentration $\bar{c}_{i,s}$ to the superficial current density i_{far}. Because the porosity is assumed uniform throughout the porous layer, ϵ may also be thought of as the area fraction of the superficial compact layer / porous layer interface that is not blocked by the solid part of the porous layer. Transport through the porous layer of the film creates a through-film limiting current for reduction,

$$i_{\text{lim},f} = -\frac{F \epsilon \bar{c}_{O,\infty}}{\frac{L}{D_{O,f}} + \frac{1}{k_{mt}}} \tag{3.3}$$

Under the assumption that k_{mt} is very large compared to $L/D_{O,f}$, Eq. 3.3 reduces to

$$i_{\text{lim},f} = -\frac{F \epsilon D_O \bar{c}_{O,\infty}}{\tau L} \tag{3.4}$$

where τ is the tortuosity of the film. Tortuosity may be related to porosity by a Bruggeman relation:

$$\tau = \epsilon^{-0.5}; \tag{3.5}$$

however, this relationship may not apply to all systems.

Eq. 3.3 may be found as the limit of i_K, the kinetic current found from extrapolating Koutecký-Levich plots, as $\bar{\eta} \to -\infty$. A plot of $\ln(i_K)$ vs. $\bar{\eta}$ or $\bar{V}$ yields α_a from the slope and i_0 and thus k_{eff} from the intercept at $\bar{\eta} = 0$ or $\bar{V} = E^{oc}$. Alternatively, raw current measurements instead of extrapolated i_K values can be fit by first calculating the surface concentration of both species

$$\bar{c}_{i,s} = \bar{c}_{i,\infty} \left(1 - \frac{\bar{i}_n}{i_{\text{lim},i}} \right) \tag{3.6}$$

where

$$i_{\text{lim}}^{-1} = i_{\text{lim},\infty}^{-1} + i_{\text{lim},f}^{-1} \tag{3.7}$$

and $i_{\text{lim},\infty}$ is given by the Levich equation. With the surface concentration calculated, $\bar{\eta}$ is found by inverting Eq. 3.1 after calculating i_0 with assumed values of k_{eff} and α_a. These values are iterated until the calculated and theoretical curves agree. Because bulk transport is so well characterized in RDE systems, calculating i_0 and $i_{\text{lim},f}$ from $\bar{i}$ vs. $\bar{V}$ instead of i_K vs. $\bar{V}$ curves gives the same results with fewer measurements.

Previous work found that both i_0 and $i_{\text{lim},f}$ decreased with increasing passivation time. Because both k_0 and k_{mt} should be independent of the thickness of the passivating film, the suggested explanation was that a decrease in ϵ was responsible for the trend of i_0 and $i_{\text{lim},f}$ with passivation time. This explanation is consistent with a study by Aurbach et al., who found that the roughness of the SEI decreased as reduction products filled holes of existing surface films [43].

Frequency response of passivated electrode

Although the relative speed and ease of EIS measurements make it a useful diagnostic tool for evaluating the performance and aging of cells, drawing meaningful conclusions from impedance spectra can be difficult. Most studies rely on equivalent circuits for interpreting EIS data; these do not always provide a clear link between physical processes and the frequency response of the system. Furthermore, multiple equivalent circuits may mathematically describe the system with equal accuracy, although the physical meanings of the circuits are different [44]. In this work, we follow a different approach to EIS by developing a physical model for the system in the manner of previous studies [45, 46, 47].

To find the impedance of the system, an overpotential η is applied to the electrode while the current i is measured. Both consist of a steady state and oscillating contribution such that

$$\eta = \bar{\eta} + \text{Re}\{\tilde{\eta}\exp(j\omega t)\} \tag{3.8}$$

and

$$i = \bar{i} + \text{Re}\{\tilde{i}\exp(j\omega t)\} \tag{3.9}$$

The calculated impedance is resolved into real and imaginary components:

$$Z = \frac{\tilde{\eta}}{\tilde{i}} = Z_{Re}(\omega) + jZ_{Im}(\omega) \tag{3.10}$$

The measured current i has both a faradaic contribution from the reduction of ferrocenium to ferrocene and a capacitive contribution from double-layer charging inside the diffuse part of the SEI.

$$\tilde{i} = \tilde{i}_{\text{far}} + \tilde{i}_{\text{cap}} = \tilde{\eta}Z_{\text{far}}^{-1} + C_{dl}\frac{d\tilde{\eta}}{dt} \tag{3.11}$$

Including the effect of bulk electrolyte resistance R_b yields

$$\tilde{i} = (\tilde{\eta} - \tilde{i}R_b)Z_{\text{far}}^{-1} + C_{dl}\frac{d(\tilde{\eta} - \tilde{i}R_b)}{dt} \tag{3.12}$$

Rearranging gives

$$Z = R_b + \frac{Z_{\text{far}}Z_{\text{cap}}}{Z_{\text{far}} + Z_{\text{cap}}} \tag{3.13}$$

$Z_{\text{far}} = \tilde{\eta}/\tilde{i}_{\text{far}}$ and $Z_{\text{cap}} = 1/(sC_{dl})$, where $s = j\omega$. Eq. 3.13 corresponds to the well-known parallel RC-circuit and is illustrated in Fig. 3.1. C_{dl} refers to the capacitance of electrolyte in the porous layer

In this work, $R_{f,p}$ and $R_{f,c}$, the ohmic resistances of the porous and compact layers of the SEI, respectively, are both assumed to be negligible. This assumption is based on the lack of apparent ohmic resistance in the previous steady-state experiments. In the porous layer, ionic current is carried by solvated lithium ions in electrolyte-filled pores. Thus, the resistance of the layer will be

$$R_{f,p} = \frac{L\tau}{\epsilon\kappa} \tag{3.14}$$

where κ is the electrolyte conductivity. Eq. 3.14 assumes that the solid part of the porous layer is ionically as well as electronically nonconducting. To include $R_{f,p}$ in the impedance model, it should be added to R_b in Eq. 3.13.

The resistance of the compact layer is given by

$$R_{f,c} = l\rho \tag{3.15}$$

where ρ refers to the ionic resistivity of the inorganic compounds, such as LiOH and Li_2CO_3, that form the compact layer. If the compact layer is very thin and has a negligible ohmic resistance and double-layer capacitance, it contributes to reaction impedance only by slowing the rate constant for ferrocene reaction as a result of electron tunneling. If the ohmic resistance and double-layer capacitance of the compact layer become appreciable, an additional parallel RC-circuit term is added to Eq. 3.13. In contrast to this work, which focuses on the porous layer of the SEI, many previous studies on the SEI have used impedance to estimate the properties of the compact layer; Refs. [44] and [43] are two of many examples.

The faradaic impedance Z_{far} is determined by linearizing the interfacial Butler-Volmer kinetics about the steady-state overpotential $\bar{\eta}$ and surface concentrations $\bar{c}_{O,s}$ and $\bar{c}_{R,s}$.

$$\tilde{i}_{\text{far}} = \frac{\partial i_{\text{far}}}{\partial \eta}\tilde{\eta} + \frac{\partial i_{\text{far}}}{\partial c_{O,s}}\tilde{c}_{O,s} + \frac{\partial i_{\text{far}}}{\partial c_{R,s}}\tilde{c}_{R,s} \tag{3.16}$$

When $\bar{\eta} = 0$, linearization gives

$$\tilde{\eta} = \frac{RT}{F}\left[\frac{\tilde{i}_{\text{far}}}{i_0} + \frac{\tilde{c}_{O,s}}{c_{O,\infty}} - \frac{\tilde{c}_{R,s}}{c_{R,\infty}}\right] \tag{3.17}$$

whereas if $\bar{\eta} \neq 0$,

$$\tilde{\eta} = \frac{RT}{F}\left(\frac{\alpha_c K_c}{c_{O,\infty}}\bar{c}_{O,s} + \frac{\alpha_a K_a}{c_{R,\infty}}\bar{c}_{R,s}\right)^{-1}\left[\frac{\tilde{i}_{\text{far}}}{i_0} + \frac{K_c}{c_{O,\infty}}\tilde{c}_{O,s} - \frac{K_a}{c_{R,\infty}}\tilde{c}_{R,s}\right] \tag{3.18}$$

where

$$K_a = \exp\left(\frac{\alpha_a F}{RT}(\bar{\eta} - \bar{i}R_b)\right) \quad \text{and} \quad K_c = \exp\left(-\frac{(1-\alpha_a)F}{RT}(\bar{\eta} - \bar{i}R_b)\right)$$

The presence of $\bar{c}_{O,s}$ and $\bar{c}_{R,s}$ in Eq. 3.18 places several limits on the experimental parameters for impedance measurements. For stationary electrodes in battery systems, measurements made at potentials other than open circuit will not be meaningful because the system will never be at steady-state and thus cannot be properly linearized. For a rotating disk electrode, the impedance will become infinite at extreme overpotentials because at the limiting current, both $\bar{c}_{O,s}$ and K_a approach zero. At potentials between open circuit and the limiting current, $\bar{c}_{O,s}$ and K_c have opposing magnitudes, making measurements extremely sensitive to instrument error and noise from the glovebox electronics. For these reasons, the following analysis is restricted to linearization about open circuit.

A concentration impedance may be defined as the change in surface concentration divided by the change in flux for both the oxidized and reduced species

$$Z_O = \frac{\tilde{c}_{O,s}}{\tilde{N}_O} = \frac{\tilde{c}_{O,s}}{\tilde{i}_{\text{far}}/F} \qquad\qquad Z_R = \frac{\tilde{c}_{R,s}}{\tilde{N}_R} = -\frac{\tilde{c}_{R,s}}{\tilde{i}_{\text{far}}/F} \tag{3.19}$$

yielding at $\bar{\eta} = 0$

$$\frac{\tilde{\eta}}{\tilde{i}_{\text{far}}} = Z_{\text{far}} = \frac{RT}{F}\left[\frac{1}{i_0} + \frac{Z_O}{Fc_{O,\infty}} + \frac{Z_R}{Fc_{R,\infty}}\right] = R_{ct} + \frac{RT}{F^2}\left[\frac{Z_O}{c_{O,\infty}} + \frac{Z_R}{c_{R,\infty}}\right] \tag{3.20}$$

The charge-transfer resistance R_{ct} is here defined as $\frac{RT}{Fi_0}$. Determining the concentration impedances Z_R and Z_O requires solution of the partial differential equations governing transient mass transfer. For the rotating disk, concentration in the bulk layer is governed by convective diffusion,

$$\frac{\partial \tilde{c}_i}{\partial t} + v_x\frac{\partial \tilde{c}_i}{\partial x} = D_i\frac{\partial^2 \tilde{c}_i}{\partial x^2} \tag{3.21}$$

while a stagnant diffusion applies in the porous layer of thickness L:

$$\frac{\partial \epsilon\tilde{c}_{i,f}}{\partial t} = -\frac{\partial \tilde{N}_{i,f}}{\partial x} = D_{i,f}\frac{\partial^2 \epsilon\tilde{c}_{i,f}}{\partial x^2} \tag{3.22}$$

The factor of ϵ relates the in-pore concentration $c_{i,f}$ to the superficial flux N_i. If a stationary electrode with a finite diffusion-layer thickness instead of rotating electrode is used, Eq. 3.22 applies in the outer layer as well, with $D_{i,f}$ replaced by D_i.

Eq. 3.21 requires numeric solution, but for the present purpose, only the ratio of bulk concentration to bulk flux is required:

$$Z_b = \frac{c(L)}{N(L)} = \frac{\delta}{D}\frac{1}{\Gamma(4/3)}\frac{1}{\theta'(0)} \tag{3.23}$$

where $1/\theta'(0)$ is tabulated in Ref. [45] and the subscript i has been dropped for simplicity. If the electrode does not rotate, bulk impedance is given by the semi-infinite Warburg expression

$$Z_b = \frac{c(L)}{N(L)} = \frac{1}{\sqrt{D\omega j}} \tag{3.24}$$

In the film, solving Eq. 3.22 via Laplace transform yields

$$\tilde{c}_f(x) = A\exp\left(\sqrt{sx^2/D_f}\right) + B\exp\left(-\sqrt{sx^2/D_f}\right) \tag{3.25}$$

and

$$\tilde{N}_f(x) = -\epsilon\sqrt{sD_f}\left[\left(A\exp\left(\sqrt{sx^2/D_f}\right) - B\exp\left(-\sqrt{sx^2/D_f}\right)\right)\right] \tag{3.26}$$

where $s = j\omega$ and A and B are constants to be determined by the boundary conditions. These are given at $x = L$, where the superficial flux is continuous,

$$\tilde{N}_f(L) = \tilde{N}_b(L) \tag{3.27}$$

and the relation between the bulk concentration and in-pore film concentration is given by the rate of mass transfer into the film

$$\tilde{N}_f(L) = \epsilon k_{mt}\left(\tilde{c}_f(L) - \tilde{c}_b\right) = \epsilon k_{mt}\left(\tilde{c}_f(L) - Z_b\tilde{N}_b\right) \tag{3.28}$$

If mass-transfer into the film is assumed to be very fast, k_{mt} is large, and the in-pore concentration is also continuous;

$$\tilde{c}_f(L) = \tilde{c}_b(L) = Z_b\tilde{N}_b(L) \tag{3.29}$$

Evaluating Eqs. 3.25 and 3.26 at 0 and L and combining with Eqs. 3.27 and 3.28 yields

$$Z_f = \frac{\tilde{c}_f(0)}{\tilde{N}_f(0)} = \frac{\frac{1}{k_{mt}} + \epsilon Z_b + \tanh(\sqrt{st_f})/\sqrt{sD_f}}{\epsilon\sqrt{sD_f}\left(\frac{1}{k_{mt}} + \epsilon Z_b\right)\tanh(\sqrt{st_f}) + \epsilon} \tag{3.30}$$

where $t_f = \frac{L^2}{D_f} = \frac{\tau L^2}{D}$. If k_{mt} is assumed large, the expression for the through-film concentration impedance reduces to

$$Z_f = \frac{\tilde{c}_f(0)}{\tilde{N}_f(0)} = \frac{\epsilon Z_b + \tanh(\sqrt{st_f})/\sqrt{sD_f}}{\epsilon^2 Z_b\sqrt{sD_f}\tanh(\sqrt{st_f}) + \epsilon} \tag{3.31}$$

Inspection of Eq. 3.31 shows that if $L = 0$, Z_f reduces to Z_b, while a porosity of 0 yields an infinite impedance. Eq. 3.31 also agrees with the expression of Deslouis et al., who solved for the impedance of a membrane-coated rotating disk electrode, but did not include the effect of the membrane porosity or partitioning into the membrane [48]. Although further analysis in this work also assumes that k_{mt} is large, the previous steady-state results suggest that porosity is a critical parameter and cannot be neglected.

Transient model for open-circuit potential of passivated electrode

In neat electrolyte without ferrocene or ferrocenium, the thermodynamic equilibrium potential of an inert electrode such as glassy carbon or platinum is not well-defined. The potential measured at open-circuit may lie anywhere within the stability limit of the electrolyte and is influenced by the identity and concentration of trace impurities. When ferrocene and ferrocenium are added to the solution, the open-circuit potential is determined by the Nernst equation; thus, monitoring potential versus time gives a measurement of the relative rates at which ferrocene and ferrocenium penetrate the film and reach the electrode surface.

Transport in the film and bulk solution is described by Eqs. 3.22 and 3.21, respectively. After the film is formed, but before ferrocene and ferrocenium are added, $c = c_f = 0$. Open-circuit conditions mean that at the electrode surface ($x = 0$), the flux is zero. To describe the system rigorously, Eq. 3.21 should be solved with a boundary condition of $c \to c_\infty$ as $x \to \infty$ while matching flux and concentration at the film/solution interface. However, the boundary condition of $c \to c_\infty$ when $x \to \infty$ assumes a step change in bulk solution concentration at $t = 0$. This assumption is inaccurate because in the experimental procedure, 1 mL of 10 mM ferrocene/ferrocenium solution is added to the 8 mL of electrolyte already in the cell. Although the RDE provides rapid stirring, the solution still requires a few seconds to become perfectly mixed. Depending on the length of film-formation time, transience in the open-circuit potential is observed for up to ten minutes. We therefore make the approximation that transport through the bulk diffusion layer is rapid in comparison to diffusion through the film and assume that at $x = L$, $c_f = c_\infty$. Experimentally, applying a high rotation speed to the electrode should obtain this condition. Assuming that any transience is due to stagnant film diffusion and none to convective bulk diffusion overestimates the film time constant and sets an upper bound on mass-transport limitations in the film. The boundary condition of $c_f = c_\infty$ again assumes that k_{mt} in Eq. 3.3 is very large so that mass transfer into the film is not limiting.

Eq. 3.22 is solved using separation of variables by converting c_f to a dimensionless deviation variable

$$C_f = \frac{c_f - c_\infty}{c_\infty} \tag{3.32}$$

where c_∞ is the steady-state solution equal to the uniform bulk concentration. Nondimensionalizing the initial and boundary conditions yields

$$\frac{\partial C_f}{\partial t}(t, x = 0) = 0 \tag{3.33}$$

$$C_f(t, x = L) = 0 \tag{3.34}$$

$$C_f(t = 0, x) = -1 \tag{3.35}$$

Solving yields

$$C_f(x, t) = -\sum_{n=0}^{\infty} B_n \exp(-\lambda_n^2 Dt) \cos(\lambda_n x) \tag{3.36}$$

where $\lambda_n = \frac{\pi}{L}(n + \frac{1}{2})$ and $B_n = \frac{2(-1)^n}{L\lambda_n}$. The concentration at the electrode surface is of primary interest; substituting and converting back to dimensional concentration yields

$$c_{i,f}(0, t) = c_{i,s} = c_{i,\infty} \left[1 - \sum_{n=0}^{\infty} \frac{4(-1)^n}{\pi(2n+1)} \exp\left(-\frac{\pi^2 (2n+1)^2}{4} \frac{t}{t_{i,f}} \right) \right] \tag{3.37}$$

where $t_{i,f}$ again is equal to $L^2/D_{i,f} = \tau L^2/D_i$. Eq. 3.37 can be substituted into the Nernst equation to track the open-circuit potential as ferrocene and ferrocenium penetrate the film. Subtracting the steady-state open-circuit potential gives a quantity that can be compared to experiment:

$$E^{oc} - E^{oc,ss} = \frac{RT}{F} \ln \left(\frac{1 - \sum_{n=0}^{\infty} B_n \exp\left(-\frac{\pi^2 (2n+1)^2}{4} \frac{t}{t_{O,f}} \right)}{1 - \sum_{n=0}^{\infty} B_n \exp\left(-\frac{\pi^2 (2n+1)^2}{4} \frac{t}{t_{R,f}} \right)} \right) \tag{3.38}$$

At long time, the negative exponential sign means that higher-order terms in the infinite series of Eq. 3.38 become negligible. For the same reason, the summation term of Eq. 3.38 with the faster time constant will also be negligible compared to that with the slower time constant. Because of the exponential dependence on time, a plot of $\ln(E^{oc} - E^{oc,ss})$ versus t is linear at long time, with a slope equal to $-\frac{\pi^2}{4t_{i,f}}$ or $-\frac{\pi^2 D_i}{4\tau L^2}$. Here, i corresponds to the oxidized species. The bulk diffusion coefficient is 2.23 $\times 10^{-6}$ cm^2/s for ferrocene and 1.29 $\times 10^{-6}$ cm^2/s for ferrocenium [49]. After extracting the quantity τL^2 from the plot of $\ln(E^{oc} - E^{oc,ss})$ vs. t, it can be substituted back into Eq. 3.38, and the result compared directly to experiment.

3.3 Results and discussion

Film formation and steady-state ferrocene reduction

As previously described, the electrode was passivated at 0.6 V vs. Li/Li$^+$. The total charge passed during the formation hold at 0.6 V is plotted vs. total formation time in Fig. 3.2. In order to demonstrate the range of formation times sampled, only the final data point in the series is shown. Three curves are shown, representing three different rotating disk electrodes. Scatter within each curve reveals fluctuations in temperature and imperfections

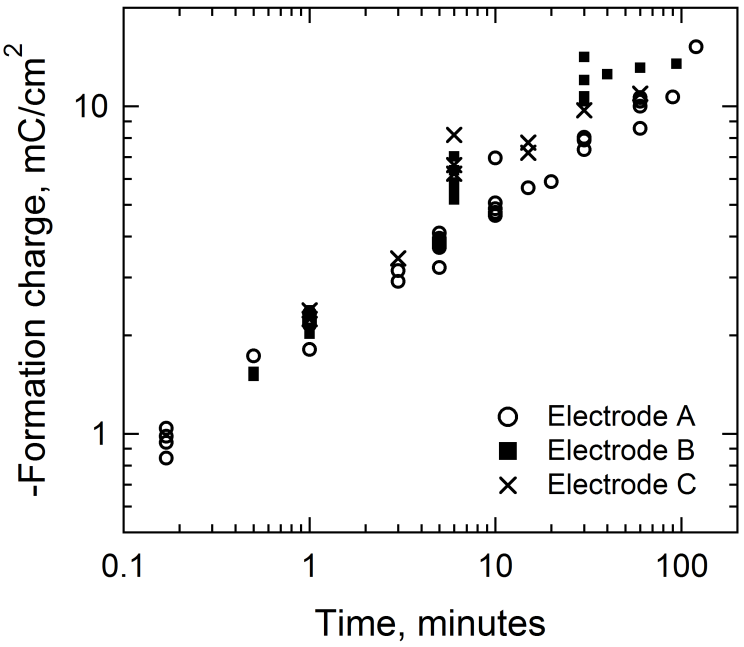

Figure 3.2: Film-formation charge vs. time for different glassy carbon samples. Electrode A is reproduced from Ref. [49] while Electrodes B and C are new measurements. The scatter within each curve and difference between curves is discussed in the text.

in the cleaning procedure, while the difference between curves is more likely indicative of differences between the specific surface chemistry of the different glassy carbon samples.

The through-film ferrocenium reduction current was measured, and the results fit to the steady-state model by varying the three fitting parameters α_a, k_{eff}, and $i_{\text{lim},f}$. An example is shown in Fig. 3.3. As passivation time increases from 0.5 to 60 minutes, both the limiting current and the rate constant decrease. k_{eff} and $i_{\text{lim},f}$, normalized for concentration, are plotted vs. formation charge in Fig. 3.4 (a) and (b). Consistent with Fig. 3.2, there are significant differences among the three electrodes in both the values of k_{eff} and $i_{\text{lim},f}$ and in the slope of the curve with formation charge. However, the slopes of the two parameters agree with each other for each electrode, reinforcing the hypothesis that the same phenomenon causes both parameters to decrease. Because ϵ appears in both expressions, a decreasing porosity with longer formation time is able to explain the trend in both parameters.

The dependence of film formation and characterization on the specific carbon substrate demands a more detailed discussion of the use of a glassy carbon electrode in this work and of how SEI formation is expected to differ between glassy carbon and graphite. The electrochemical behavior of glassy carbon may be related to that of graphite by the work of Rice, et al., who meticulously measured ferro/ferricyanide kinetics on different carbon substrates [50, 51]. They found that electron transfer rates were 10^5 times higher on edge-plane than basal-plane graphite. The rate increased linearly as more edge planes were exposed, and

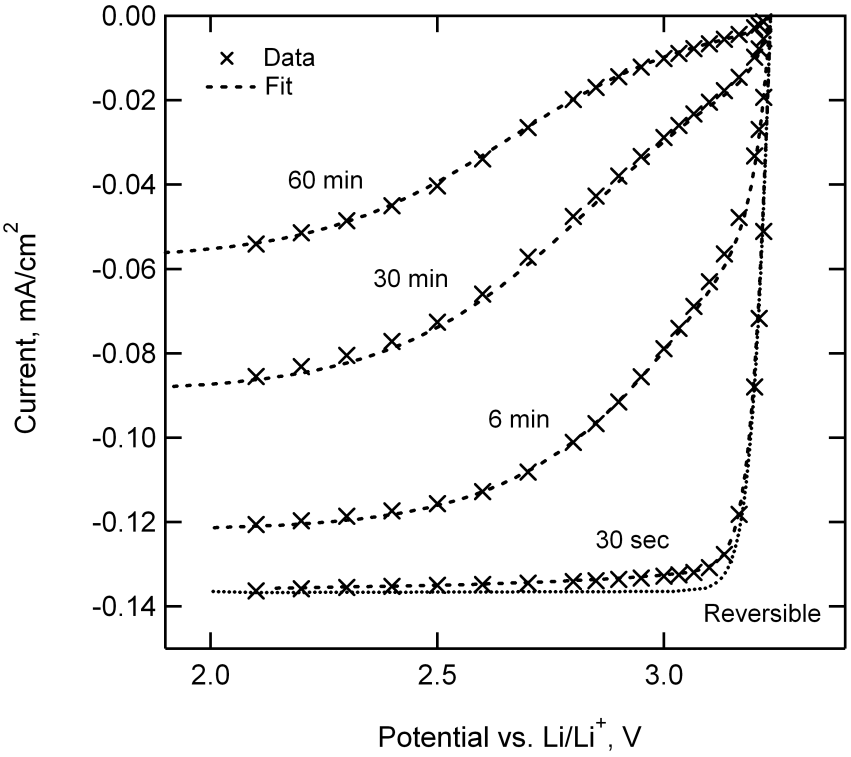

Figure 3.3: Steady-state i-V curves at 900 rpm for passivation holds of 0.5, 6, 30, and 60 minutes at 0.6 V. Markers are measurements; line is model fit. The dotted line shows the reversible limit (no SEI). Ferrocene/ferrocenium concentration is 1.1/1.1 mM.

comparing the behavior of glassy carbon led them to conclude that the glassy carbon surface has an inherently high density of edge-plane sites compared to basal plane graphite.

Knowing the relative density of edge-plane sites on glassy carbon is important because the orientation of the graphite plane has been shown to affect strongly the potential at which electrolyte reduction starts to occur. Using AFM images on highly oriented pyrolytic graphite (HOPG), both Hirasawa et al. and Chu et al. saw that film formation began preferentially along cleavage steps of the HOPG surface and crystal boundaries of a composite graphite electrode between 1.5 and 2.0 V, while reduction occurred on the basal plane of HOPG and the surface of the composite electrode at 0.8 to 0.9 V [52, 53]. These results, combined with XPS studies by Bar-Tow et al., suggest that anions were reduced on the edge plane at 1.5 V while solvent reduction occurred at lower voltages on the basal plane of graphite [9]. Thus, a possible explanation for the variation between samples in Fig. 3.4 may be differences between the relative densities of edge-plane and basal sites among the different glassy carbon samples. If one electrode has more edge-plane sites than the others, it may actually be forming different reaction products, thus causing a different rate of film growth. Although all three glassy carbon samples were obtained from the same manufacturer

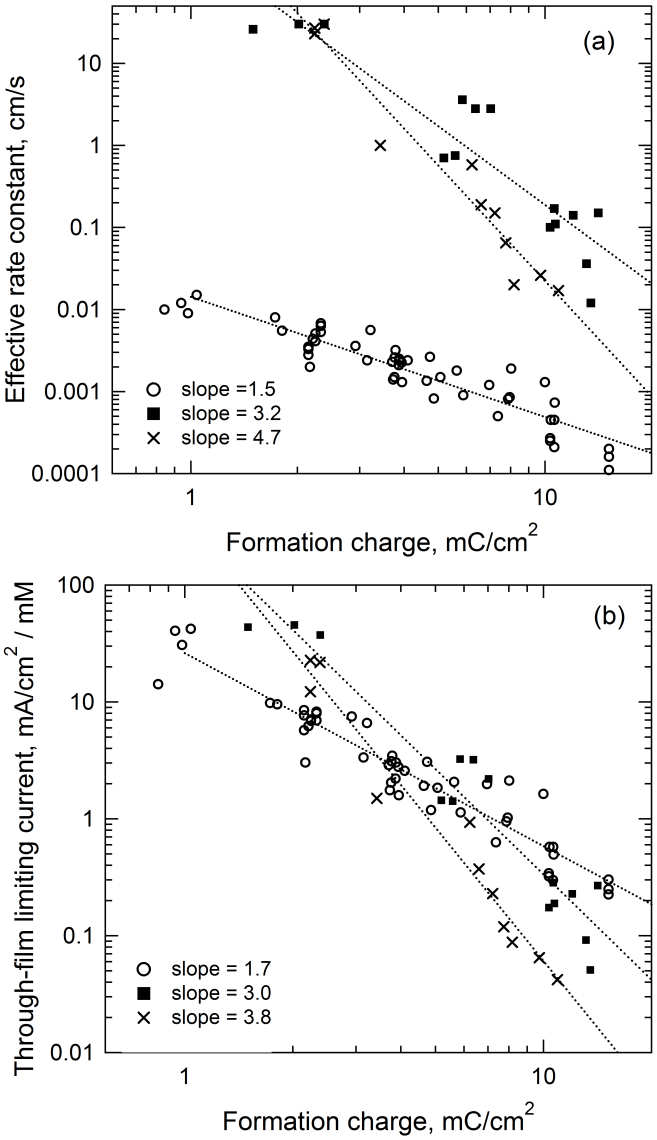

Figure 3.4: (a) effective rate constant, $k_{\text{eff}} = k_0\epsilon$, and (b) through-film limiting current normalized for concentration, $i_{\text{lim},f}/c_{O,\infty} = \frac{F\epsilon D_O}{L\tau}$ vs. formation charge. As the length of passivation time increases, both parameters decrease, suggesting that the film porosity decreases. Although the slope of the line is different for each of the three samples, the slope of $i_{\text{lim},f}$ and k_{eff} are similar for each sample, suggesting that the same phenomena govern the decrease in both parameters. For discussion of the differences between samples, see text.

(ALS), the samples may easily have differed in their previous exposure to heat, polishing, and other factors that affect the surface. These factors can also cause the glassy carbon surface to become functionalized with oxygen-containing side groups, further affecting the

surface chemistry that occurs during electrolyte reduction [54].

Impedance

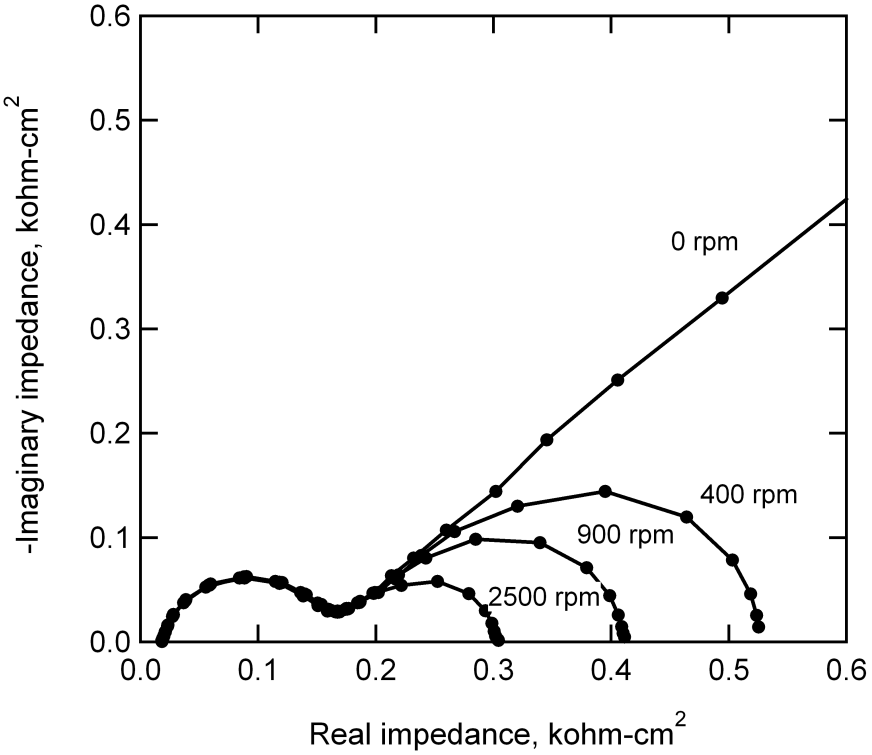

Figure 3.5: Nyquist plot of passivated electrode at different rotation speeds. Passivation time is 5 minutes, solution is 1.9/0.8 mM ferrocene/ium. The high-frequency arc is independent of rotation speed, while the low-frequency arc decreases with faster rotation speeds.

Nyquist plots at different rotation speeds of an electrode passivated for 5 minutes at 0.6 V are shown in Fig. 3.5. The curve exhibits two arcs, one at high frequency and one at low frequency. The low-frequency arc depends on rotation speed, but the high-frequency arc does not. This observation is consistent with a transport resistance in the bulk diffusion layer ($l + L \leq x \leq l + L + \delta$) and either a second transport process in the porous part of the film ($l \leq x \leq l + L$) or a charge-transfer process at $x = l$. As the amount of passivation time increases, the width of the high-frequency arc also increases, consistent with a more passivated system (Fig. 3.6). For small amounts of passivation (enlargement, Fig. 3.6b), the low-frequency arc is independent of passivation time, but as the high-frequency arc grows in width, it eventually obscures the low-frequency arc. The growth of the high-frequency arc is also shown in the frequency dependence of the data (Fig. 3.7). As passivation time increases, the high-frequency peak increases in magnitude and moves to lower frequency, causing the

peaks to merge. The high-frequency real intercept of the impedance varies between 0.013 and 0.016 kΩ-cm^2 for all amounts of passivation (Fig. 3.7a). With an electrolyte conductivity of 7.8 mS/cm [32], and electrode diameters of 3 mm, the theoretical ohmic resistance is $R = \frac{\pi r_0}{4\kappa} = 0.015$ $k\Omega$-cm^2. Both the agreement between theoretical and measured ohmic resistance and the lack of dependence on passivation time support the hypothesis that the compact layer of the SEI is ionically conductive.

i_K-V plots are much easier to interpret than Nyquist or Bode plots such as those in Figs. 3.6 and 3.7. The i_K vs. V curve is described by three parameters i_0, $i_{\mathrm{lim},f}$, and α_a, all of which affect the curve uniquely. If an ohmic resistance of the film is included, it will also have a unique effect on the i_K curve. In comparison, the impedance measurements in Fig. 3.6 and 3.7 have only two clear characteristic numbers, the width of the high-frequency arc, w_{HF}, and the time constant of the arc, t_{EIS}, which is the inverse of the frequency at which the imaginary component is a maximum. Both of these experimental parameters are plotted against the film formation charge in Fig. 3.8. Because the characteristic time and the resistance should be related by

$$t_{EIS} = w_{HF} C_{dl}, \tag{3.39}$$

the two parameters should exhibit the same dependence on formation charge if the double-layer capacitance does not change. The slopes are similar (2.5 vs. 3.0), suggesting that C_{dl} changes very little as the film growth increases. Because w_{HF} depends more strongly on formation charge than t_{EIS}, C_{dl} may decrease slightly as Q_{form} increases. Such a situation may be explained by a decrease in effective area as the electrode is blocked by the passivating film. The slope of 3.0 for the dependence of resistance on formation charge also is very close to the slopes of -2.9 and -3.0 for limiting current and effective rate constant, suggesting that all three parameters are dominated by the same phenomenon.

As well as being more difficult to interpret, the impedance spectra are more difficult to fit than the steady-state data. The parameters used to fit the steady-state model map clearly to physical constants by the relations in Eqs. 3.2 and 3.4, but Eq. 3.31 requires separate input of porosity, film time constants $t_{O,f}$ and $t_{R,f}$, and the film diffusivities $D_f = D/\tau$. In addition, the impedance introduces another physical parameter, C_{dl}. Thus, in order to fit the transient impedance model, we use the steady-state fitting parameters to calculate the relevant physical constants. First, a film thickness is assumed from the literature. Although some AFM measurements have measured the SEI to be several hundred nanometers thick [53, 43], other AFM studies have found film thicknesses of 25 to 70 nm [52, 55]. Considering the uncertainty in measurements, the variation with electrolyte chemistry, and the fact that the SEI in our system is less completely formed than that in many previous studies, a thickness of 5 to 50 nm is assumed for fitting. Next, assuming that $\tau = \epsilon^{-0.5}$ or $\tau = 1$ permits calculation of ϵ from $i_{\mathrm{lim},f}$. When ϵ is known, k_0 can be calculated from k_{eff}. α_a is used without changes, and C_{dl} is adjusted in order to fit the frequency dependence of the maximum imaginary impedance. $R_{f,p}$ is again assumed to be negligible. This assumption is also justified by considering the theoretical resistance of the porous layer in Eq. 3.14. For

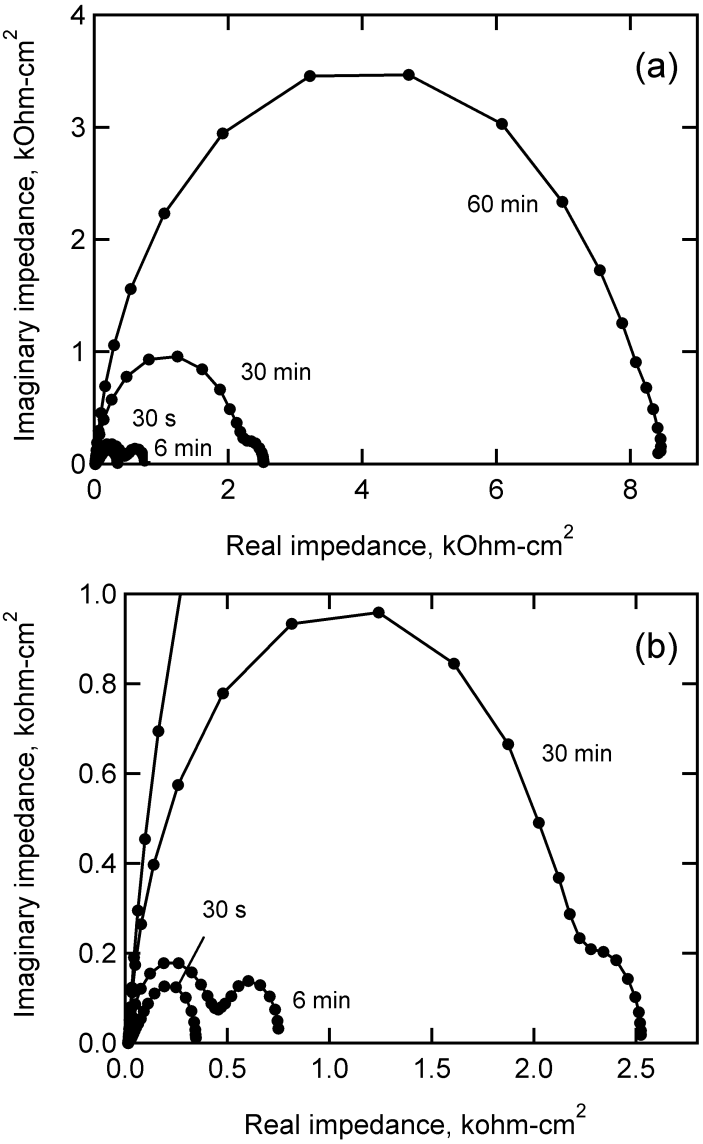

Figure 3.6: a) Nyquist plot of electrode passivated for 0.5, 6, 30, and 60 minutes at 0.6 V at 900 rpm. b) Expanded scale of 0.5, 6, and 30 minute curves. As the passivation time increases, the high-frequency arcwidth increases while the low-frequency behavior does not change. The high-frequency real intercept of the curve is unaffected by passivation. Ferrocene/ium concentration is 1.1 mM.

$L = 50$ nm and $\kappa = 7.8$ mS/cm, τ/ϵ must be smaller than 6.4 $\times 10^{-4}$ in order for R_f to exceed 1 Ω-cm^2.

A sample calculation of the above procedure is shown in Fig. 3.9. The data shown are 1.1 mM ferrocene/ferrocenium after 30 minutes at 0.6 V. The impedance is measured at open

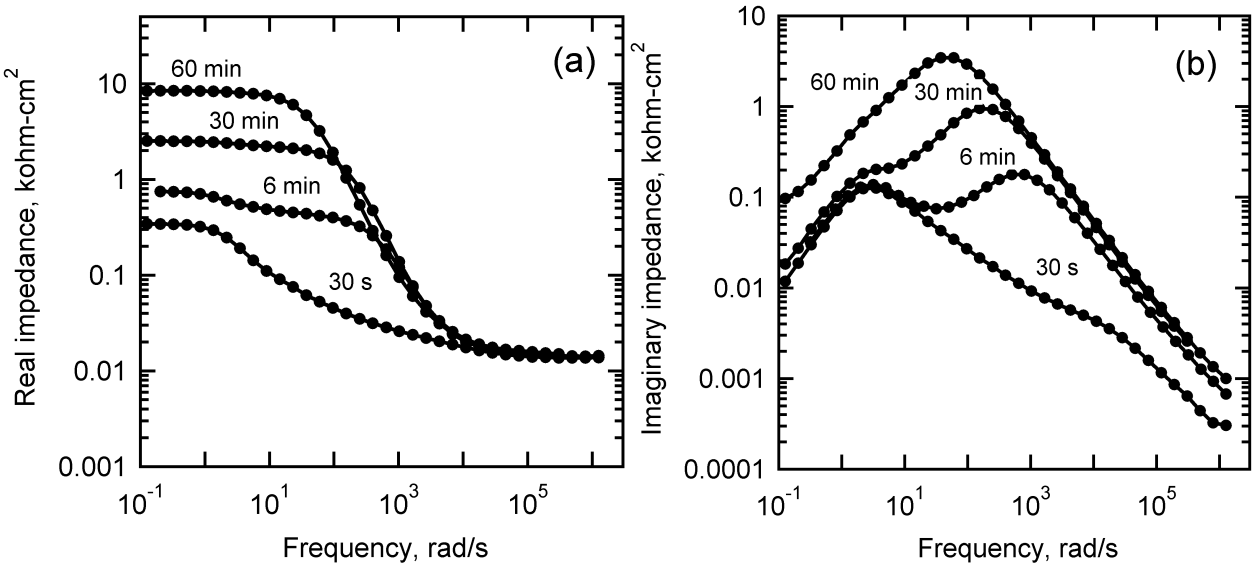

Figure 3.7: Real (a) and imaginary (b) impedances vs. frequency for electrode passivated for 0.5, 6, 30, and 60 minutes at 0.6 V at 900 rpm. As the film becomes more passivating, the response of the electrode slows and the peak frequency decreases.

circuit and 0 rpm. From the $i_K - V$ curve (circles, Fig. 3.9b), $\alpha_a = 0.885$, $k_{\text{eff}} = 0.14 \times 10^{-3}$ cm/s, and $i_{\text{lim},f} = -0.26$ mA/cm^2. Assuming a thickness of 50 nm and $\tau = \epsilon^{-0.5}$ yields $\epsilon = 0.044$ and $k_0 = 3.2 \times 10^{-3}$ cm/s. Calculating the impedance spectra using these values and Eqs. 3.13, 3.17, and 3.31 (Fig. 3.9a, solid line) underestimates the measured arcwidth (crosses). If the film is assumed to be only 5 nm thick, ϵ decreases to 0.009, but because k_{eff} remains constant, k_0 increases to 14.8 $\times 10^{-3}$ cm/s and the curves collapse. Ignoring the Bruggeman relation and assuming that $\tau = 1$ also does not improve agreement between the calculated and measured data.

Fitting the experimental arcwidth requires either reducing k_{eff} by decreasing k^0 approximately 15% (dashed line) or reducing $i_{\text{lim},f}$ by increasing L by a factor of approximately three (broken line). The dashed and broken lines are virtually indistinguishable on the Nyquist plot because the fit is equally good. When the two sets of adjusted values are substituted back into the steady-state model (Fig. 3.9 b), neither set of adjusted parameters maintains the same fit as the optimized i_K values. However, decreasing k_{eff} reduces the agreement by much less than decreasing $i_{\text{lim},f}$ does. The steady-state and EIS methods of characterization thus agree with each other within 15% for this trial. Although RDE and EIS data for only one trial are shown, the fitting procedure was repeated for 15 of the 16 data points in Fig. 3.8 (Electrode B in Figs. 3.2 and 3.4), with k_0 adjusted to fit the high-frequency arcwidth. On average, decreasing k_0 by approximately 10% was sufficient to achieve agreement between the methods. The ratio of values of k_0 used to fit the steady-state and impedance measurements is shown in Fig. 3.10.

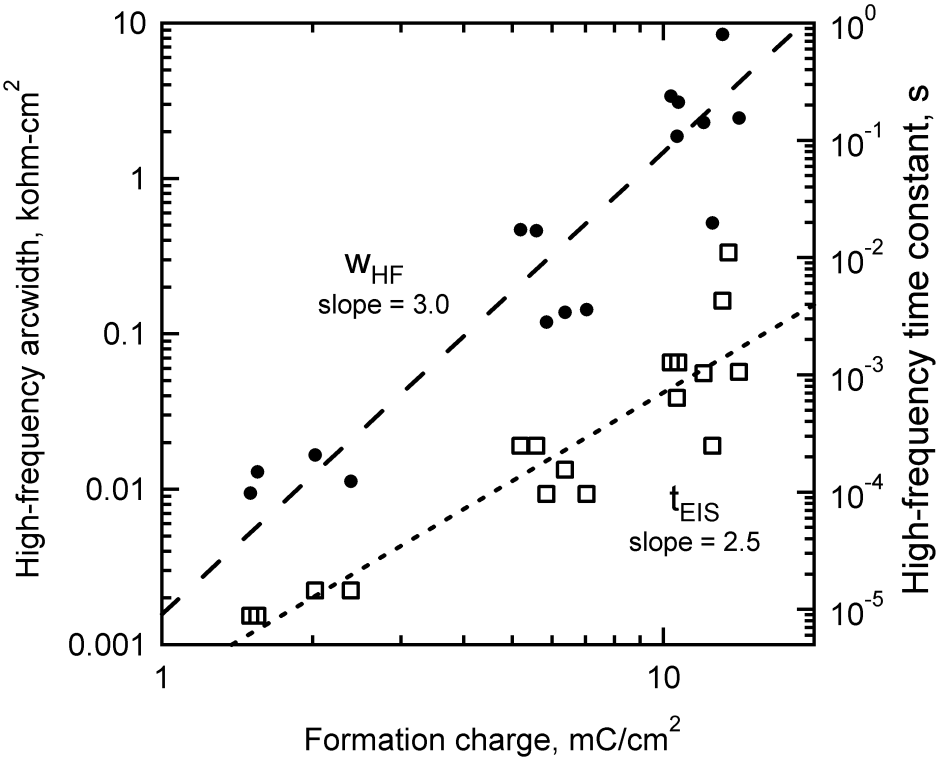

Figure 3.8: High-frequency arcwidth (squares) and characteristic time constant $t_{\rm EIS}$ (circles) vs. formation charge. Only data from Electrode B in Fig. 3.4 are shown. The slopes are similar to each other, suggesting that double-layer capacitance does not change greatly with formation charge. The slope is also similar to the dependence of limiting current and effective rate constant on formation charge.

Comparison of Figs. 3.9 a) and b) clearly demonstrates the superiority of the steady-state method at measuring unique parameters of the film. While the EIS spectra can be fit by adjusting either $k_{\rm eff}$ or $i_{{\rm lim},f}$ (in the form of L), the i_K curve requires a specific value of each. The inability of the EIS method to separate transport and kinetic passivation effects makes it extremely difficult to measure quantitatively film characteristics such as those shown in Fig. 3.4 and is a major disadvantage of the method. The reason for this inability is that all measurements are made at the same potential. Although through-film transport, slow Butler-Volmer kinetics, and ohmic resistances all decrease the steady-state current, i_K is measured at different potentials. The dependence of i_K on voltage can be linear with voltage (R_f), exponential with voltage (α_a and i_0), or independent of voltage ($i_{lim,f}$). In constrast, EIS is measured exclusively at the open-circuit potential, eliminating the ability to determine the potential-dependence of the high-frequency arcwidth.

Although Fig. 3.9 demonstrates that EIS is not as effective as steady-state RDE measurements for drawing quantitative or even qualitative trends, it also shows that, because

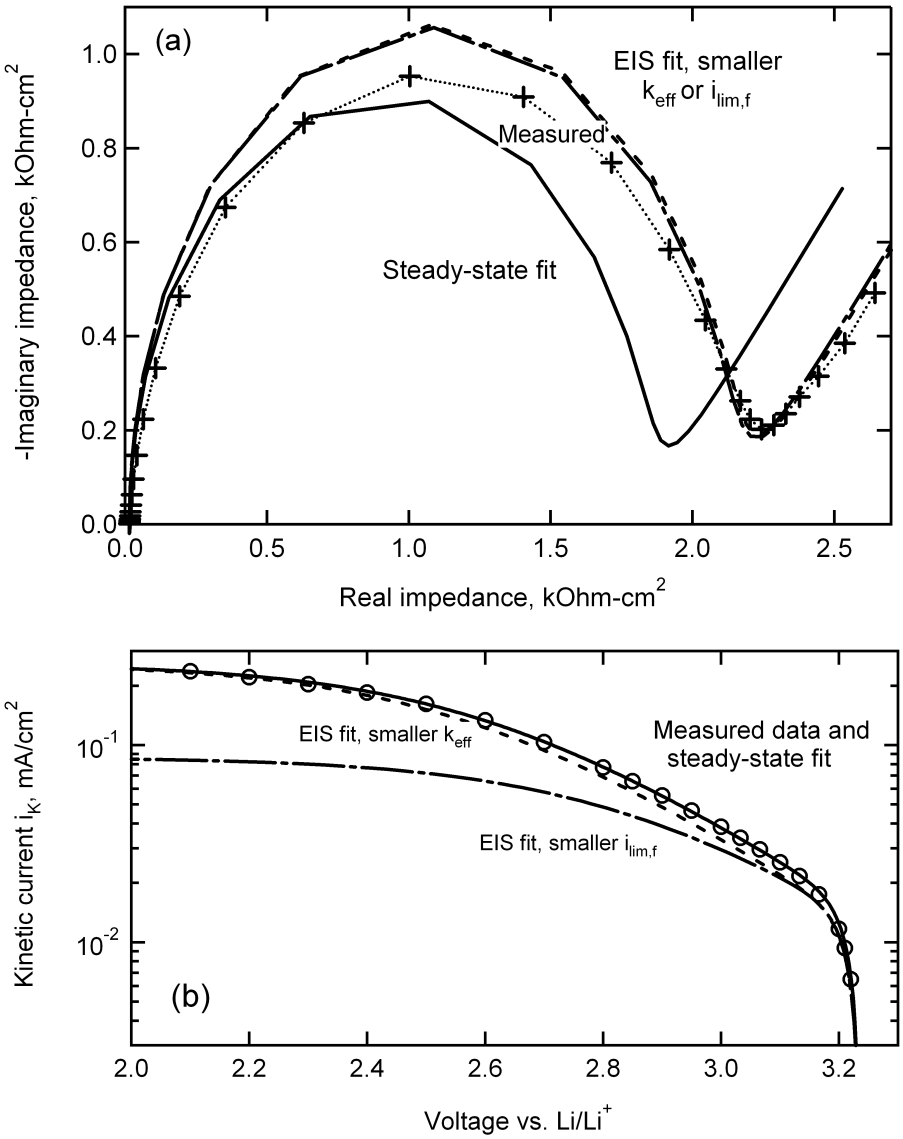

Figure 3.9: Comparison of steady-state and EIS models. a) For EIS measurements at 0 rpm (crosses), the impedance model calculated using the best-fit parameters for steady-state measurements underestimates the width of the high-frequency arc (solid line). Either reducing k_{eff} by 15% (dashed line) or $i_{\text{lim},f}$ (broken line) by a factor of three can approximate the arcwidth. (b) The steady-state model using the EIS-fit value of k_{eff} (dashed line) provides a better fit to steady-state measurements (circles) than the EIS-fit value of $i_{\text{lim},f}$ (broken line). Neither approximates data as well as the steady-state fitting parameters (solid line). The data shown are 1.1 mM ferrocene/ium after 30 minutes at 0.6 V.

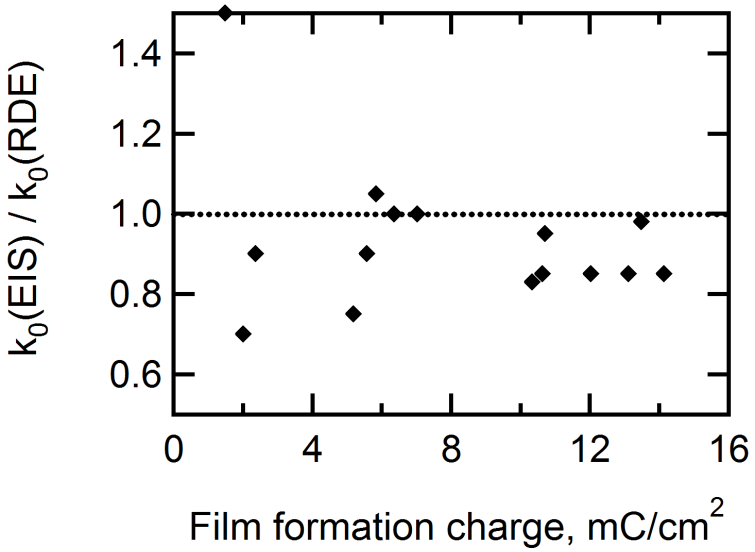

Figure 3.10: Agreement between steady-state and EIS fitting methods. The y-axis shows the ratio of the values of k_0 used to fit the steady-state and impedance data. A value of 1.0 means that the same parameters were able to fit both measurements. Generally, decreasing the rate constant by 10 to 15 % is enough to bring the methods into agreement.

the high-frequency arc is independent of rotation speed, the model can describe EIS data obtained on a stationary electrode. Being able to measure film characteristics, even very qualitatively, without the use of a rotating disk electrode reduces or eliminates many experimental constraints on the system and is the greatest advantage of the EIS method.

Evolution of open-circuit potential

In order to provide a separate estimation of $t_{O,f}$ and $t_{R,f}$, the open-circuit potential was monitored as ferrocene and ferrocenium were introduced to the passivated electrode. Representative data are shown in Fig. 3.11 . Immediately after the film formation hold at 0.6 V and 0 rpm, the open-circuit potential is measured to be between 1.0 and 1.5 V. Because the reactions are unknown, the equilibrium potential is ill defined. The electrode rotation speed was then set to 900 rpm. The corresponding jump in potential suggests that the equilibrium potential before the addition of ferrocene is determined by the concentration of a dilute species. After the initial change, 1 mL of 10 mM ferrocene/ferrocenium was added to the solution, causing a second jump in the potential. The potential then asymptotically approaches the steady-state value determined by the Nernst equation. Fig. 3.11 shows that, for longer formation times, the rate at which the potential approaches the steady-state value is slower.

Subtracting the steady-state value from the transient potential and plotting on semilog

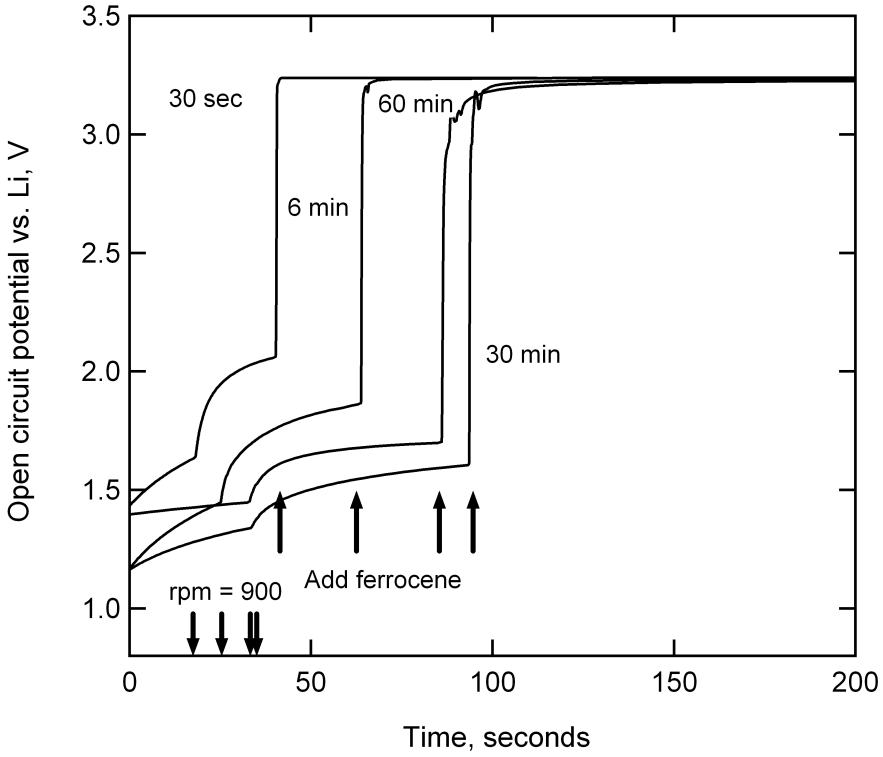

Figure 3.11: Open-circuit potential vs. time after passivation at 0.6 V. The first set of arrows indicates the times that rotation speed jumps from 0 to 900 rpm, and the second set indicates when ferrocene and ferrocenium are introduced into the solution.

coordinates permits comparison of the measured data and model from Eq. 3.38 (Fig. 3.12). Time constants are extracted from the long-time slope of $\ln(E^{oc} - E^{oc,ss})$ vs. time and used to calculate the theoretical potential as determined by Eq. 3.38. Fig. 3.12 shows that the shape of the curve agrees with experiment. Although the calculated potential leads the experimentally measured voltage, the poorly-defined potential at t = 0 means that the location of the curves on the time axis is not meaningful.

Plotting the calculated time constant versus film formation charge shows that as passivation time increases, the film time constant also increases, in agreement with qualitative explanations. However, converting the measured time constants to physical parameters yields numbers that do not make sense. For example, if $t_{O,f} = \frac{L^2}{\tau D_O} = 50$ s, assuming $L = 50$ nm and $\tau = \epsilon^{-0.5}$ yields porosity values on the order of 10^{-15}. Assuming that tortuosity is unity yields a calculated thickness of 80 μm, a number which is clearly unreasonable. If, instead, an expected time constant is calculated from estimated values of the film parameters, assuming that $L = 50$ nm and $D_{O,f} = 1.29 \times 10^{-6}$ cm^2/s yields $t_{O,f} = 2 \times 10^{-5}$ seconds. The expected slope of $\ln(E^{oc} - E^{oc,ss})$ vs. time with such a small time constant is on the order of 10^5 s^{-1}, much higher than values calculated from data as in Fig. 3.12. Because the quantitative

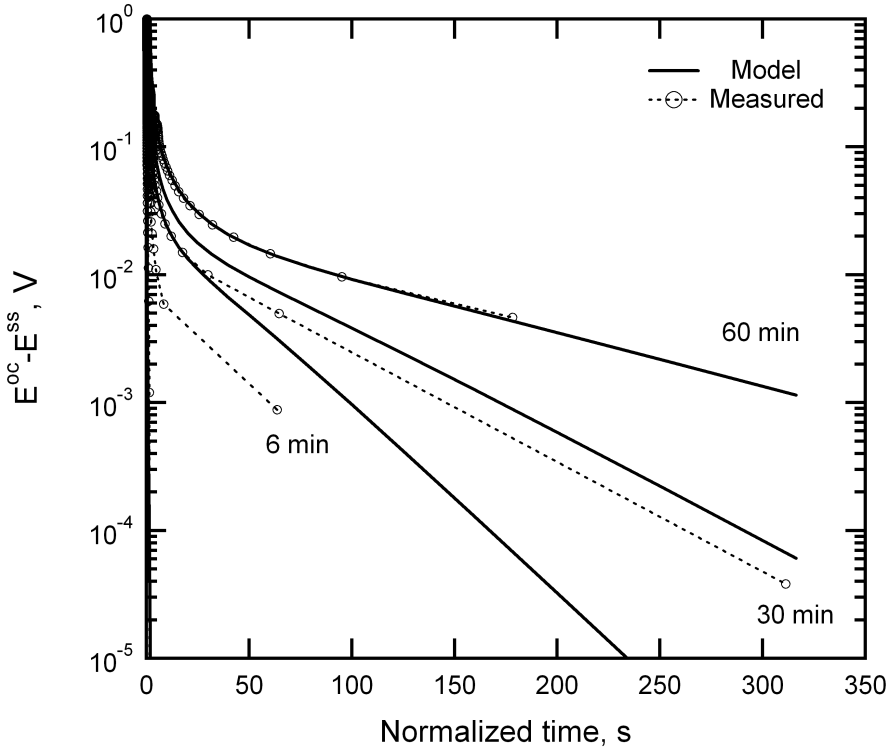

Figure 3.12: Difference between steady-state and transient open-circuit potential vs. time after passivation at 0.6 V. t= 0 is defined as the time at which ferrocene is added to the solution. The slope of the measured data at long time gives the time constant of the system; this is used to calculate the model fits.

values calculated by the evolution of open-circuit potential agree neither with intuition nor the other methods of measurement, another phenomenon besides ferrocene/ium transport must be responsible for the qualitative trends shown in Fig. 3.13 . One possibility may be a relaxation process inside the film, or the diffusion of a reactive intermediate away from the electrode. The dependence of the open-circuit potential on rotation speed (Fig. 3.11 shows that transport from the bulk to the surface affects the process. One possibility is that HF, which has been shown to react with and dissolve carbonate reduction products, is reacting with the primary reduction products of ethylene carbonate [56, 57].

3.4 Conclusions

Measuring ferrocene kinetics in the presence of passivating films allows direct measurement of the effect of films on reduction kinetics. Steady-state measurements show that both the effective rate constant and through-film limiting current decrease with more passivation time at roughly the same rate; this observation can be explained by a decreasing porosity.

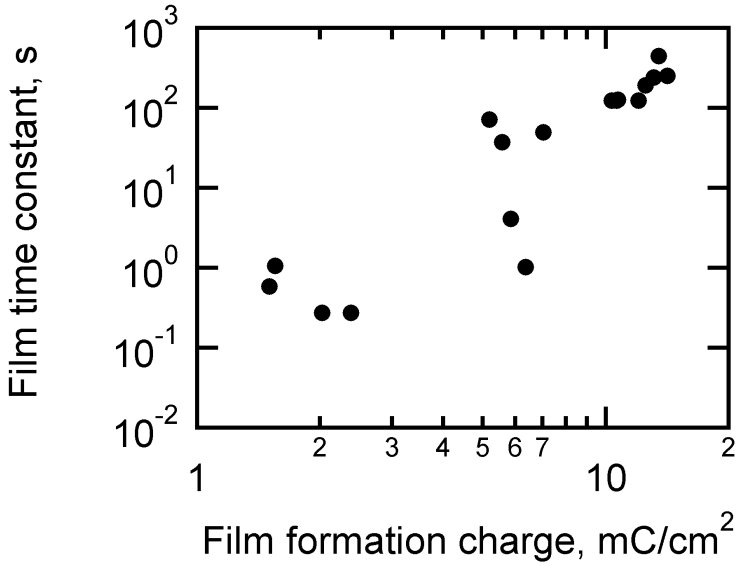

Figure 3.13: Time constant from open-circuit potential method vs. film formation charge. As passivation increases, the time constant also increases, but calculating values of L or τ from the time constant gives unreasonable values (see text).

Although different glassy carbon samples differ in both how much charge is passed for a given length of formation time and in how much the formation charge passivates the surface, the similarities between k_{eff} and $i_{\text{lim},f}$ apply across all the electrodes sampled.

Expanding the model to describe impedance and transients in the open-circuit potential provides mixed results. The high-frequency arcwidth of the impedance spectra and the film time constant increase with more passivation time, but cannot give any more mechanistic information than steady-state fitting because the fitting parameters do not affect the model uniquely. Calculating impedance using best-fit parameters from the steady-state method agrees with measurement to within 15%. Extracting time constants from the evolution of open-circuit potential as ferrocene and ferrocenium are introduced into the cell also gives a trend that agrees qualitatively with other results, but yields values for the time constant that are unrealistically high.

Although the impedance model does not give a set of unique fitting parameters, the indicators of high-frequency arcwidth and time constant agree qualitatively with steady-state results. Impedance also has significant experimental advantages over the rotating disk electrode; it is faster, uses less material, and is less subject to variations in temperature and bulk concentration. Most importantly, it permits the use of more materials, including those actually found in lithium-ion batteries. The methods developed in this work could find application as a post-mortem analysis tool in battery aging studies.

List of Symbols

c_i	Position-dependent concentration in diffusion layer, mol/cm^3
$c_{i,f}$	Position-dependent in-pore concentration in SEI, mol/cm^3
$c_{i,s}$	Concentration at porous/compact layer interface, mol/cm^3
$c_{i,\infty}$	Bulk concentration, mol/cm^3
C_{dl}	Double-layer capacitance, mF/cm^2
D_i	Diffusion coefficient in the bulk solution, cm^2/s
$D_{i,f}$	Diffusion coefficient in the film D_i/τ, cm^2/s
i_0	Exchange current density, mA/cm^2
$i_{\mathrm{lim},f}$	Through-film limiting current, mA/cm^2
i_K	Kinetic current from Koutecký-Levich intercept, mA/cm^2
k_{eff}	Effective rate constant $k_0\epsilon$, cm/s
k_0	Rate constant for ferrocene redox couple, cm/s
k_{mt}	Mass-transfer coefficient from bulk into porous layer, cm/s
l	Thickness of compact layer, cm
L	Thickness of porous layer, cm
N_i	Flux through diffusion layer, mol/cm^2 s
$N_{i,f}$	Superficial flux through SEI, mol/cm^2 s
R_b	Ohmic resistance from solution, kΩ cm^2
R_f	Ohmic resistance from film, kΩ cm^2
$t_{i,f}$	Film time constant, s
t_{EIS}	Impedance time constant, $w_{HF}C_{dl}$, s
v	Fluid velocity, cm/s
w_{HF}	High-frequency arcwidth, kΩ cm^2
Z_b	Concentration impedance, c/N
α_a	Anodic transfer coefficient
α_c	Cathodic transfer coefficient, 1- α_a
ϵ	Porosity
δ_i	Diffusion layer thickness, cm
η	Overpotential, V
η_s	Surface overpotential, V
κ	Electrolyte conductivity, mS/cm
ν	Kinematic Viscosity, cm^2/s
ϕ	Local potential, V
ρ	Compact layer resistivity, Ω cm
τ	Tortuosity
ω	Frequency, rad/s
Φ	Solid-phase potential, V
Ω	Rotation speed, rad/s
Subscripts	
O	Oxidized species, ferrocenium cation
R	Reduced species, neutral ferrocene
p	Porous layer of the SEI
c	Compact layer of the SEI
far	Faradaic
cap	Capacitive

Chapter 4

Characterization on highly oriented pyrolytic graphite

Chapters 2-3 have developed a method using ferrocene to characterize the SEI in lithium-ion batteries. However, the experiments presented so far were measured exclusively on glassy carbon. In this chapter, the ferrocene characterization method is extended to the edge and basal plane of highly oriented pyrolytic graphite (HOPG). Applying the methods developed in previous chapters to study different surfaces is highly desirable because previous work has found that graphite orientation strongly affects SEI formation reactions. Both Hirasawa et al. and Chu et al. used AFM images of HOPG to find that film formation began preferentially along cleavage steps of the HOPG surface and crystal boundaries of a composite graphite electrode between 1.5 and 2.0 V. Reduction occurred on the basal plane of HOPG and the surface of the composite electrode at 0.8 to 0.9 V [52, 53]. In these studies, the HOPG orientation was controlled by imaging either a cleavage step on the electrode or an area of the electrode that contained no defects. Because images were obtained over a few square microns of an electrode several mm in diameter, separately attributing macroscopic electrochemical properties to the different SEIs formed on the edge and basal plane of graphite was not possible. Yamada et al. took a different approach by measuring the fraction of edge planes on the HOPG surface using the kinetics of $Ru(NH_3)Cl_6$ and showing that it was inversely proportional to the macroscopic charge-transfer resistance for lithium-ion intercalation [58]. A similar result was found in a series of papers from Novák's group. Using temperature desorption experiments, they measured the active surface area, which is correlated to defects in the graphite structure. Cycling experiments then showed that, for a higher concentration of defects, electrolyte decomposed faster, permitting reversible intercalation instead of cointercalation and graphite exfoliation. [59, 60]

The previous chapters developed both rotating disk electrode (RDE) and electrochemical impedance spectroscopy (EIS) techniques to characterize the SEI using ferrocene as an electrochemical probe of the SEI [49, 61]. These two approaches have their advantages and disadvantages. The SEI creates both transport and kinetic resistances to reaction, and the RDE method can separate these, unlike impedance. Cyclic voltammetry (CV) has similar

limitations, in which the effects of transport and kinetic resistances may be experimentally indistinguishable [62, 42]. However, both EIS and CV are much less experimentally demanding and are more suitable for studying different surfaces, as HOPG is unable to meet the mechanical demands required by a RDE setup. In this chapter, both CV and EIS of ferrocene are used to monitor the electronic passivity of HOPG as the SEI is formed. We combine the techniques of Refs. [58, 63] and [49, 61] to relate the fraction of exposed edge planes on graphite, f_e, to macroscopic passivation properties. We also study the effects of SEI formation potential and compare behavior in $LiPF_6$-based and $LiClO_4$-based electrolytes.

4.1 Experimental method

Grade ZYH HOPG (mosaic spread 3.5 ± 1.5) was obtained from Momentive Performance Materials Quartz, Inc. and Structure Probe, Inc. and cleaved with adhesive tape before use. Cleavage exposed primarily the basal plane, with a fraction of edge planes, f_e along grain boundaries and defects. f_e is here defined as the fraction of total electrode area that exposes the edge plane to the electrolyte. f_b, the fraction of total electrode area that exposes the basal plane to the electrolyte, is equal to $1 - f_e$. Isolating the edge plane by embedding HOPG in resin is difficult because cutting and polishing the graphite introduces many irregularities into the system. The pressure of polishing may also cause graphite lamellae to fold and bend, exposing basal planes instead of edges. To avoid this time- and material-intensive method, samples with high values of f_e were prepared by finely scratching the freshly cleaved HOPG surface with a sharp tweezer tip to create many surface defects. A commercially available glassy carbon electrode (BASi, Inc) was prepared using the procedure developed in Ref. [49].

The fraction of edge plane, f_e, was determined from the double-layer capacitance C_{dl}, which has been shown to increase with an increasing ratio of edge to basal planes [51]. Because C_{dl} in HOPG is the capacitance of the space charge layer within the graphite instead of the diffuse part of the electrolyte double layer, values of C_{dl} can be distinguished into $C_{dl,e}$ and $C_{dl,b}$, based on the different electronic structures of the edge and basal planes, respectively [64]. Cyclic voltammagrams were measured in neat 1.0 M KCl with a Ag/AgCl reference and platinum counter electrode, and C_{dl} was calculated from the variation of average current with scan rate. The potential limits were ± 50 mV from the open-circuit potential, and the scan rate ranged from 100 to 5000 mV/s. For HOPG, the electrode area was fixed at either 0.2893 or 0.5024 cm^2 with an O-ring. Cells were made of Teflon or polypropylene. For glassy carbon, a commercially available glass cell was used. f_e was also measured using the method of Nicholson to extract a rate constant for the reaction of 1.0 mM $Ru(NH_3)_6Cl_3$ in 1.0 M KCl. Although this method has been used by several other groups [63, 65], the scratched HOPG samples exhibited reversible kinetics, so that accurate extraction of a rate constant was not possible.

After measuring the fraction of edge planes, the cell was dried in a 60^oC oven without removing the HOPG electrode and introduced to an argon atmosphere for SEI formation experiments. Care was taken to ensure that the cell temperature equilibrated to the

glovebox temperature of 22 to 25^{o}C. Lithium foil was used for the counter and reference electrodes. Electrolytes tested were 1.0 M $LiClO_4$ in ethylene carbonate (EC): dimethyl carbonate (DMC) (1:1 volume, Kishida Chemical), 1.0 M $LiClO_4$ in ethylene carbonate (EC): diethyl carbonate (DEC) (1:1 weight, Kishida Chemical), or 1.0 M $LiPF_6$ in EC:DEC (1:1 weight, Novolyte). Approximately 2.0 mM ferrocene (Sigma) was added to the electrolyte for some experiments. Instrumentation was a either a 1480 Multistat with Corrware software (Solartron) or a VMP potentiostat with EC-Lab software (BioLogic).

4.2 Results and discussion

Determination of f_e

Double-layer capacitance was measured by cycling the electrode about the open-circuit potential at 100 to 5000 mV/s. The slope of the steady-state current versus scan rate gives the double layer capacitance, which is related to f_e by

$$C_{dl} = C_{dl,e} f_e + C_{dl,b}(1 - f_e) \tag{4.1}$$

The values for $C_{dl,e}$ and $C_{dl,b}$ used were 60 and 2 μF/cm^2 [51]. A plot of f_e as calculated from Eq. 4.1 is shown in Fig. 4.1. Circles represent samples that were merely cleaved, while stars mark the samples that were scratched to increase the percentage of edge sites. The calculated values of f_e generally range between zero and unity, although several data points are outside this range. Values greater than unity or less than zero are not physically meaningful. However, any uncertainty in the values of $C_{dl,e}$ or $C_{dl,b}$ will affect the calculated values of f_e. Rice et al. reported that $C_{dl,e}$ could range up to 150 μF/cm^2, depending on the electrode surface treatment. Using a reference value of $C_{dl,e}$ = 150 μF/cm^2 brings the calculated values of f_e in Fig. 4.1 within the range of 0 to 1. The emphasis in this work is not the quantitative relationship between C_{dl} and f_e, but the qualitative effect of f_e on the formation and passivation properties of the SEI. Thus, because of the uncertainty in $C_{dl,e}$, measuring C_{dl} serves the present purpose of providing a qualitative, but not a quantitative, indicator of f_e.

Potentiostatic SEI growth

An SEI was formed by holding the HOPG electrodes at 0.6 V vs. Li/Li$^+$ in $LiClO_4$ EC:DEC for 120 minutes. Total charge passed as a function of time is plotted for selected trials in Figure 4.2. Plotting charge versus the square root of time gives a straight line, suggesting transport-limited growth. There are two distinct regions to each curve, with a transition time at approximately 20 seconds. The slope of the short-time growth region is greater than the slope at long times for all curves. Plotting the best-fit slope of each region versus f_e shows that, at long times, the SEI growth rate increases with fraction of edge planes (Fig. 4.3). At

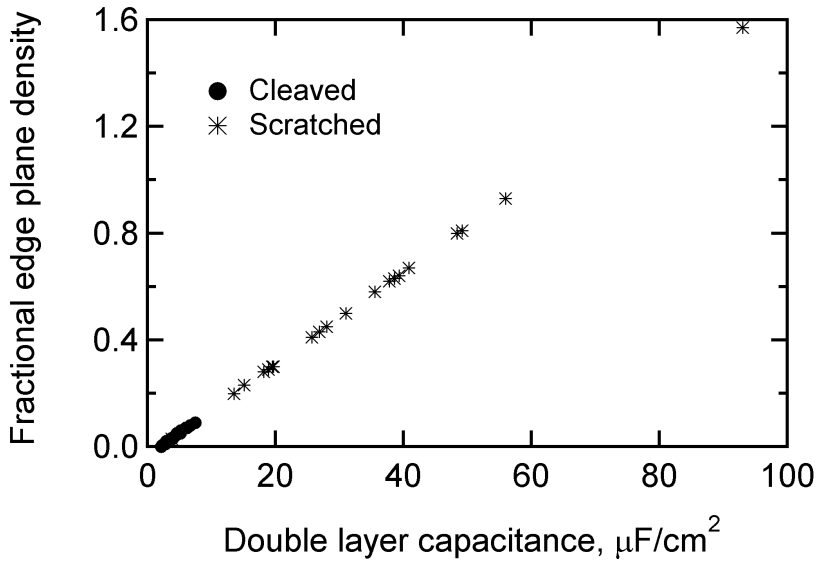

Figure 4.1: Calculation of f_e from double-layer capacitance. Dots are samples that are cleaved, stars are samples that were deliberately scratched to increase the number of defects and grain boundaries.

short times, measurements are more sensitive to instrument error, and the trend with f_e is less clear. The definition of t = 0 is also uncertain.

A higher reaction rate with increased f_e suggests that SEI-formation reactions are surface-specific and require edge sites to intercalate partially before electrochemical decomposition [66]; however, cointercalation is not required to explain the trend. If SEI formation reactions begin at higher potentials along the edge than the basal plane, formation at the same voltage of 0.6 V will result in a higher driving force, and thus higher reaction rate, on the edge plane. Furthermore, for the experiment described in Fig. 4.2, lithium intercalation should be occurring simultaneously. Because lithium ions intercalate only at the edge sites of graphite, the trend of the slope of Q vs. $\sqrt{t}$ with f_e may also be explained independently of any SEI formation.

In order to compare SEI formation on different types of carbon, the same potentiostatic SEI formation experiment was repeated on a glassy carbon electrode; this curve is shown by the dashed line in Fig. 4.2. The straight line shows that SEI formation on glassy carbon also exhibits parabolic growth. The magnitude of current is also similar between the two materials. These two observations suggest that glassy carbon may be used as a model surface for SEI formation, as previous studies have done [49, 61]. However, the dependence of formation rate on f_e in Fig. 4.3 points to the importance of knowing the fractional edge-plane density. Measuring the capacitance on glassy carbon in aqueous KCl shows that f_e is much lower than the value of f_e predicted by the relationship in Fig. 4.2 and the measured rate of SEI formation (triangles, Fig. 4.3). The different structure of HOPG means that the reference

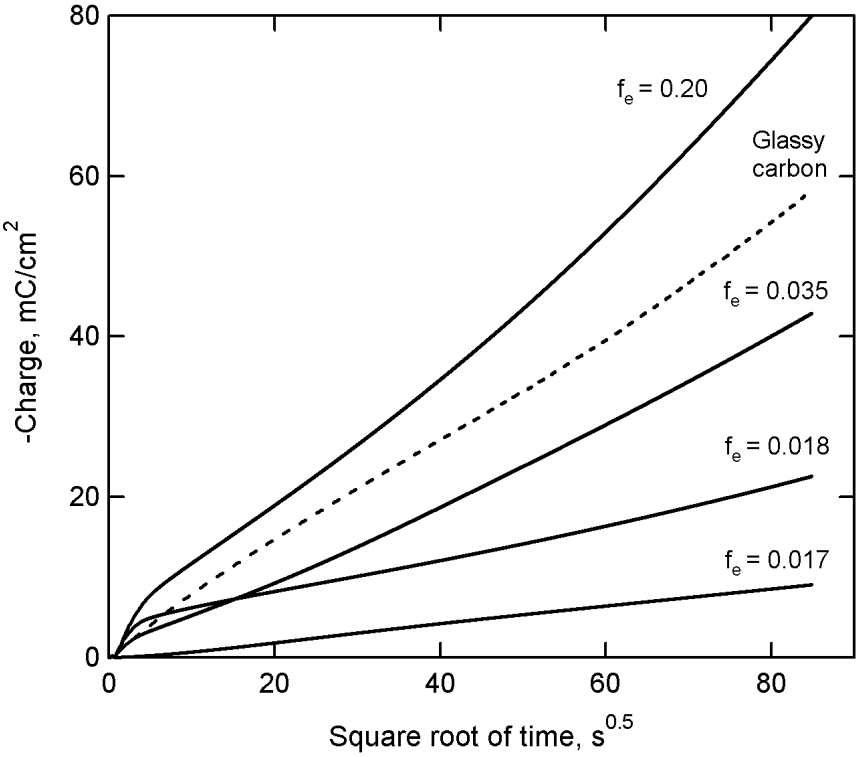

Figure 4.2: Potentiostatic SEI formation on HOPG at 0.6 V vs. lithium. As f_e increases, the rate of growth increases although the shape of the curve does not change. The dotted line shows SEI formation on glassy carbon under the same conditions. Charge is negative because SEI formation is a reduction process.

values of $C_{dl,e}$ and $C_{dl,b}$ used for HOPG may not apply to glassy carbon. Furthermore, the electrochemical behavior of glassy carbon is known to be affected by physi- and chemisorbed impurites [50, 62, 30]. The cycling procedure used to clean the glassy carbon electrode should remove such impurities, but contact with air or aqueous solution may reintroduce them to the surface. Thus, measuring C_{dl} is probably not an appropriate method of estimating f_e on glassy carbon.

The trend in Fig. 4.3b agrees with the literature in suggesting that f_e critically affects SEI formation reactions [52, 53]. However, the scatter and the difficulty of accurately measuring f_e shows that quantitative analysis of the potentiostatic data in Fig. 4.2 is extremely difficult without a separate, nonelectrochemical measurement of f_e.

Potentiodynamic SEI formation and ferrocene characterization

To address the problem of simultaneous intercalation and film formation reactions, and to gain more information about the separate reactions occurring on different orientations of

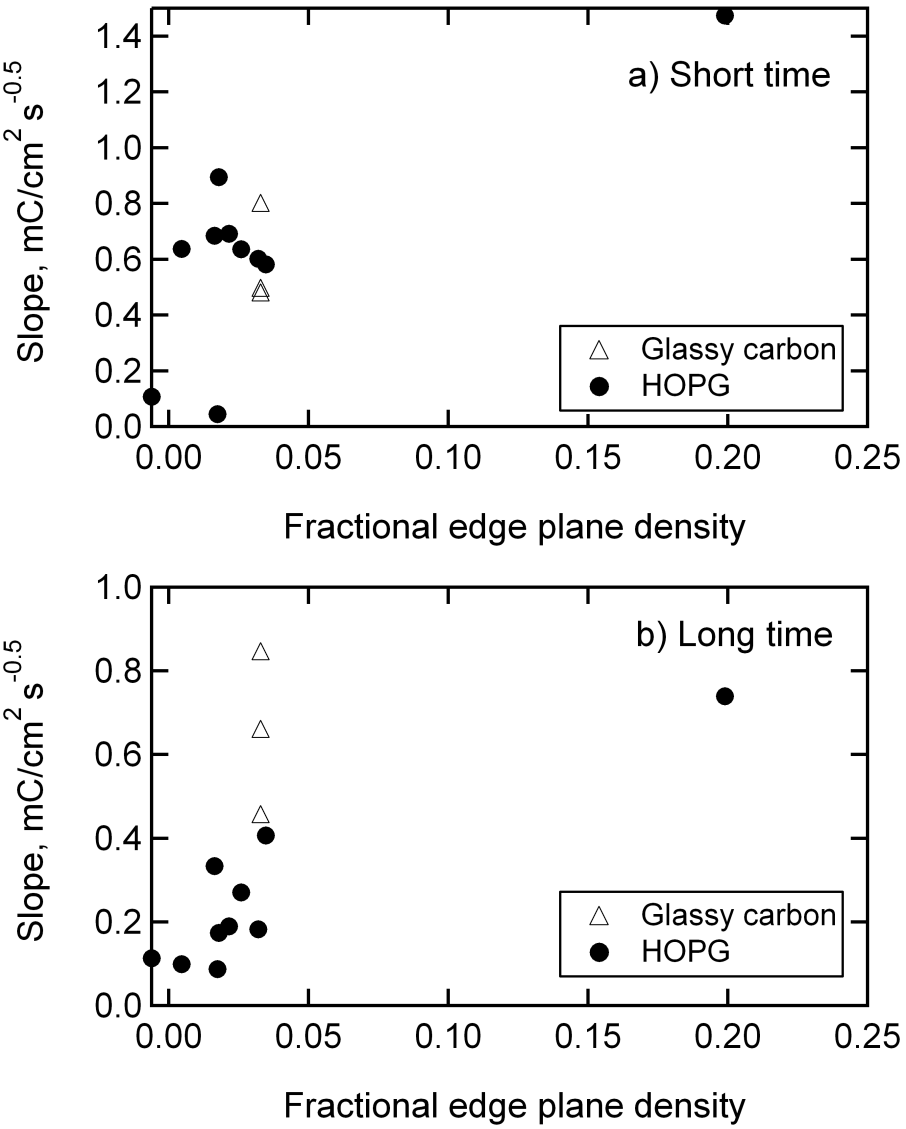

Figure 4.3: SEI formation slope vs. f_e. The dependence of long-time data on f_e is stronger than that at short time. Formation on glassy carbon (triangles) seems anomalously high, considering the f_e measured. For visual clarity, the y-axes of a) and b) have different scales.

graphite, a potentiodynamic method of SEI formation was implemented. Because lithium intercalation and electrolyte reduction occur at different peak potentials, and because intercalation appears on every cycle while electrolyte reduction decreases with cycling, potentiodynamic methods permit qualitative separation of the different reactions at the HOPG surface. Cells were cycled from open circuit to 3.7 V, then to 0.1 V vs. Li/Li$^+$ at 20 mV/s. Approximately 2 mM ferrocene was also added to the electrolyte in order to monitor the de-

gree of electronic passivation at the surface. Replicates were performed for each experiment, and while the exact peak voltages and currents varied, the general location and relative magnitudes of the peaks were consistent among samples. The comparison between samples of high fractional basal plane (cleaved samples) and high fractional edge plane (scratched samples) was also generally consistent. Control cyclic voltammagrams in neat electrolyte without ferrocene were consistent, indicating the cathodic stability of ferrocene at low potentials.

Fig. 4.4 shows a representative experiment in $LiClO_4$-based electrolyte. Three cyclic voltammagram cycles are shown on HOPG with a high fractional basal plane ($f_e = 0.01$, cleaved) and a high fractional edge plane ($f_e = 0.30$, scratched). (a) shows the entire range of data, while (b) expands the potential region in which SEI-formation reactions occur. The voltage is corrected for ohmic drop by

$$E_{\text{cor}} = E_{\text{meas}} - iR_b \tag{4.2}$$

where the bulk electrolyte resistance, R_b, is measured before SEI formation using AC impedance. Because R_b may change as the SEI evolves, the voltage correction should be the most accurate on the first cycle of formation, when most of the SEI formation occurs.

On both samples, the reduction peak at 0.1 V and oxidation peak at approximately 0.9 V occur on all cycles and thus correspond to lithium intercalation and deintercalation. Additional reduction peaks at 1.0 and 0.45 V (on the edge plane) or 0.6 V (on the basal plane) are visible only on the first cycle and thus correspond to SEI formation. All three peak currents are higher on the edge than the basal plane. After the SEI is formed, the steady-state intercalation and deintercalation currents should increase linearly with f_e because lithium intercalates preferentially or even exclusively at edge sites. Because SEI formation takes place on both orientations, it is not expected to scale so directly. Fig. 4.4 shows that, although f_e increases by a factor of 30 between the two samples, the peak intercalation and deintercalation currents increase by factors of approximately three and seven, respectively. The SEI formation peak at 0.45 or 0.6 V increases by a factor of approximately four. The discrepancy between the expected ratio of 30 and the measured ratio of seven may reflect inaccuracy in the absolute measurement of f_e, or simply that, for complicated reactions such as intercalation and electrolyte decomposition, simple linear relationships do not apply. The experiment in Fig. 4.4 was repeated over multiple trials. Although all three peak currents generally increased with f_e, the scatter in the data was too great to determine a definite shape of the relationship between peak current and f_e in any of the cases.

The effect of the SEI on ferrocene oxidation and reduction is also shown in Fig. 4.5, which is an expanded view of the high-voltage behavior in Fig. 4.4 (a). Before SEI formation and after correcting for ohmic drop, the peak potential separation is 73 mV on the basal plane and 66 mV on the edge plane, close to the reversible limit of 59 mV. The peak currents differ on the electrodes by approximately 8%, suggesting that scratching the electrode to expose more edge sites does not increase the microscopic electrode area because of surface roughening. After only one cycle of formation, the CV shows almost no ferrocene oxidation and reduction on the basal plane, and a very small current on the edge plane. Thus, the

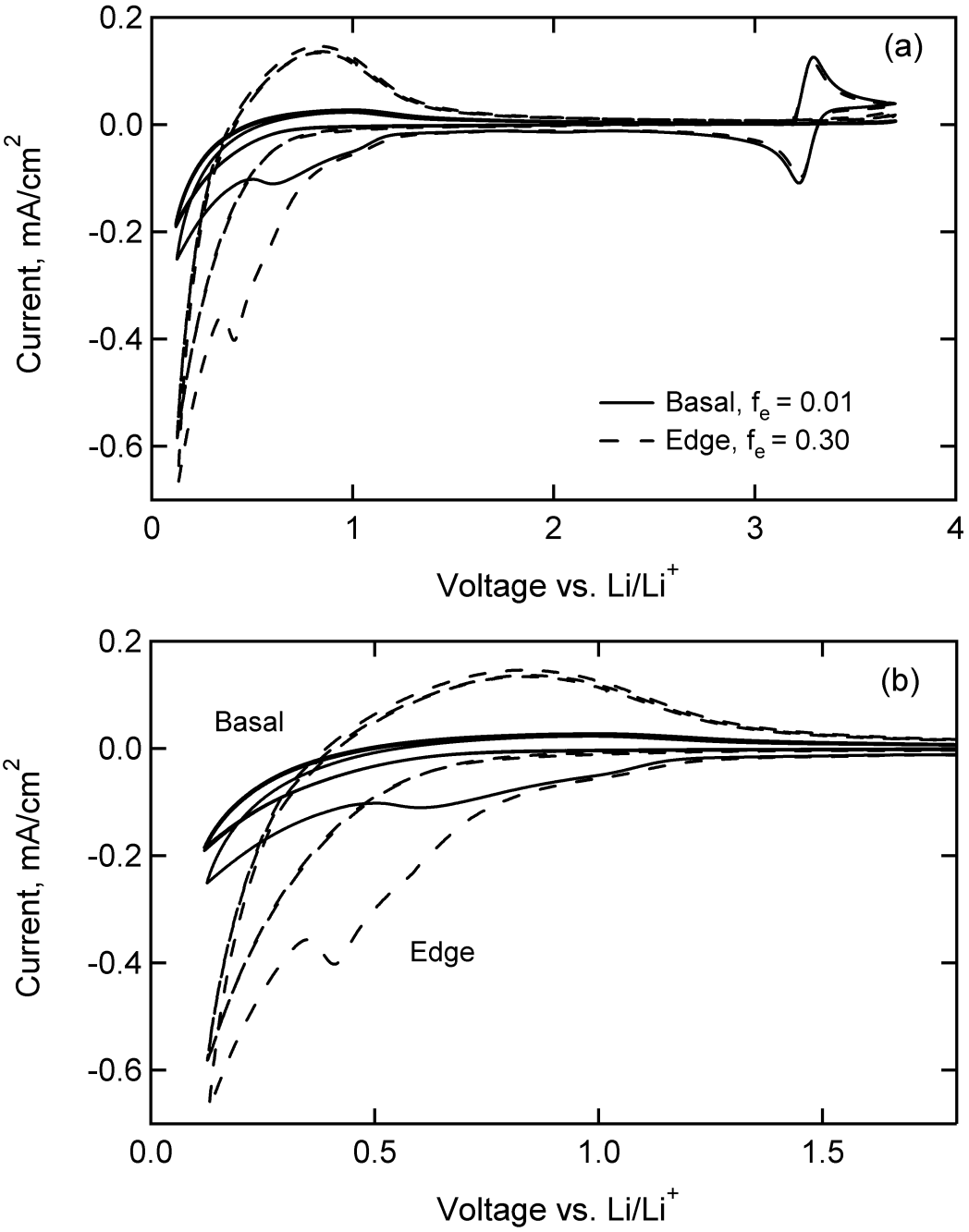

Figure 4.4: SEI formation in 1:1 EC:DMC 1.0 M $LiClO_4$ on edge and basal planes. Activity is higher on the edge than the basal plane. (a) shows the entire range of data, while (b) zooms in on the SEI-formation-potential region. Scan rate is 20 mV/s.

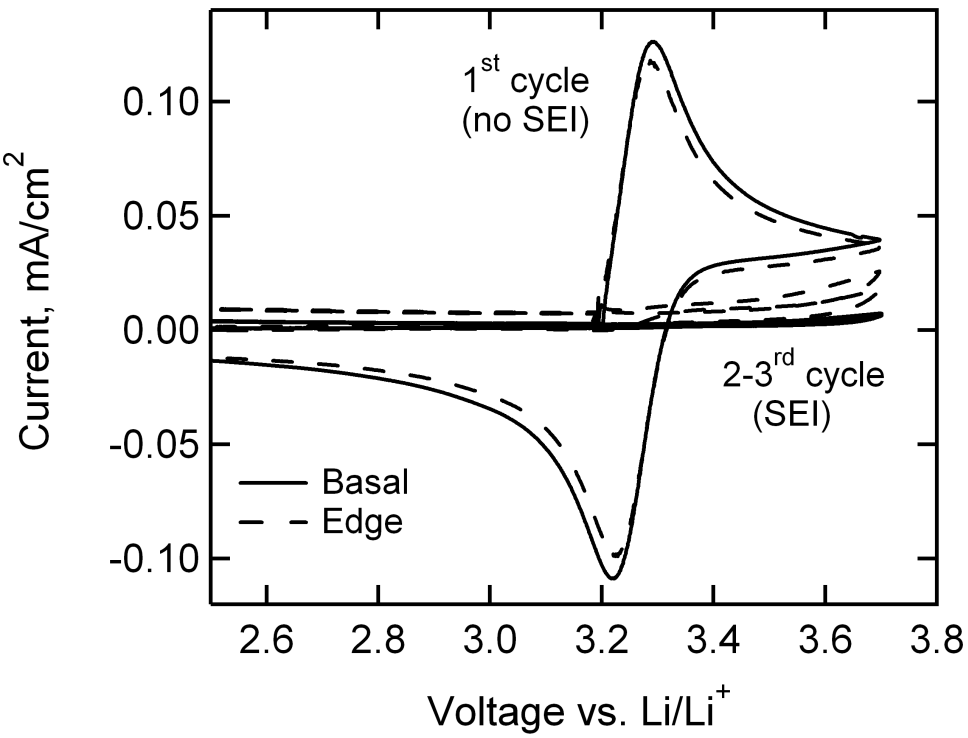

Figure 4.5: Effect of SEI formation on ferrocene CV in 1.0 M $LiClO_4$ in EC:DMC. Before formation, the ferrocene reaction is fast. After one formation cycle to 0.1 V, electron transfer is almost entirely prevented. Higher currents are measured for both SEI formation and ferrocene reaction through the SEI on the edge plane.

SEI formed on both orientations is almost completely electronically passivating after the first cycle, but the edge plane shows slightly higher activity. The slightly higher current in Fig. 4.5 may indicate that the edge-plane SEI is less electronically insulating than the basal-plane SEI, or that higher electronic activity on the edge plane permits greater activity, despite a thicker SEI. In Fig. 4.6, impedance spectra on the edge plane before and after the cycling experiment in Fig. 4.4 also show the complete electronic passivation of the SEI after formation cycles. Before cycling (dashed line), the lack of a high-frequency semicircle also shows that the reaction is fast. After formation, the impedance is extremely large. While the spectrum may exhibit a high-frequency semicircle, the diameter of the semicircle is too large to be captured in the accessible frequencies.

Effect of formation voltage

Figs. 4.4 and 4.5 show that passivation in $LiClO_4$-based electrolyte is almost entirely complete after one formation scan to 0.1 V. In order to form the SEI at a slower rate and monitor its

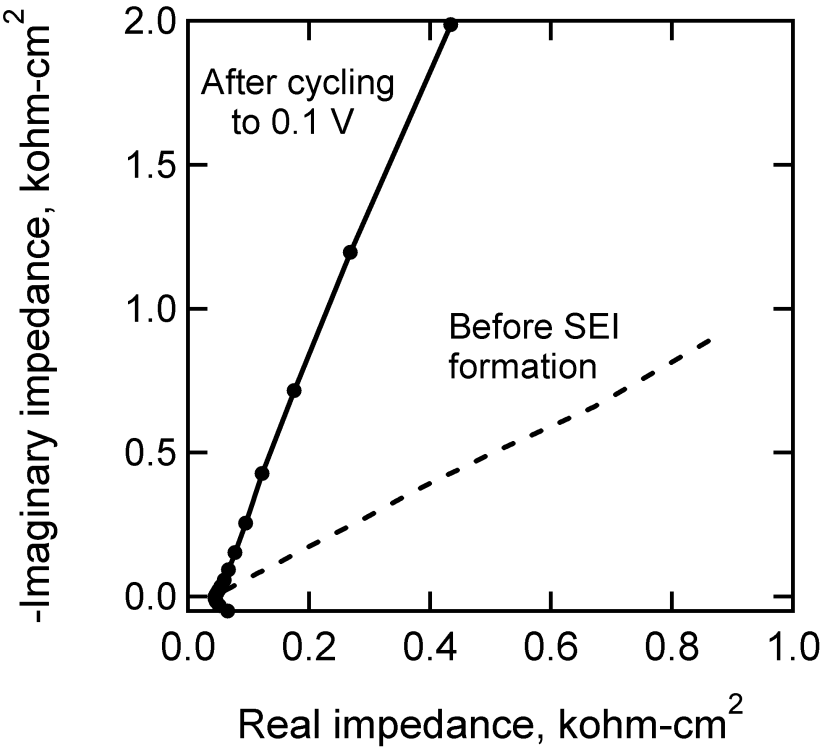

Figure 4.6: Effect of SEI formation on ferrocene EIS in $LiClO_4$. After three formation cycles to 0.1 V, the width of the high-frequency arc increases from a negligible amount to a number outside the range of measurement. Data shown are from the edge-plane sample in Fig. 4.4.

development by ferrocene kinetics, the electrode was cycled to progressively lower voltages. In between formation scans at 10 mV/s, impedance was measured at open circuit ($E^0 = 3.2$ V), and a ferrocene CV taken between 2.5 and 3.7 V at a scan rate of 100 mV/s.

This experiment is shown in Fig. 4.7 on a sample of primarily basal plane ($f_e = 0.02$). The electrode was cycled from open circuit at 3.2 V to 2.1, 1.5, 1.0, 0.6, 0.3, and 0.1 V, in that order, at 10 mV/s. SEI formation peaks occur at approximately 1.0 and 0.5 V, in agreement with Fig. 4.4. Peaks for residual oxidation and reduction of the ferrocene couple are seen around 3.2 V. Because the scan rate is slower, the magnitude of current is much smaller. Although SEI formation peaks begin to occur at 1.0 V, ferrocene kinetic measurements as shown in Fig. 4.8 show that the SEI does not provide electronic passivation until the formation voltage decreases below 0.6 V. Until the formation voltage decreases below 0.6 V, the ferrocene cyclic voltammagram does not deviate from that measured before the SEI formation cycles. The dashed line showing the ferrocene current before SEI formation is hidden underneath curves measured after formation, showing the complete lack of electronic passivation above 0.6 V. After formation to 0.3 V, the ferrocene reaction is almost completely suppressed. The CV after formation to 0.3 V shows a small oxidation current as potential

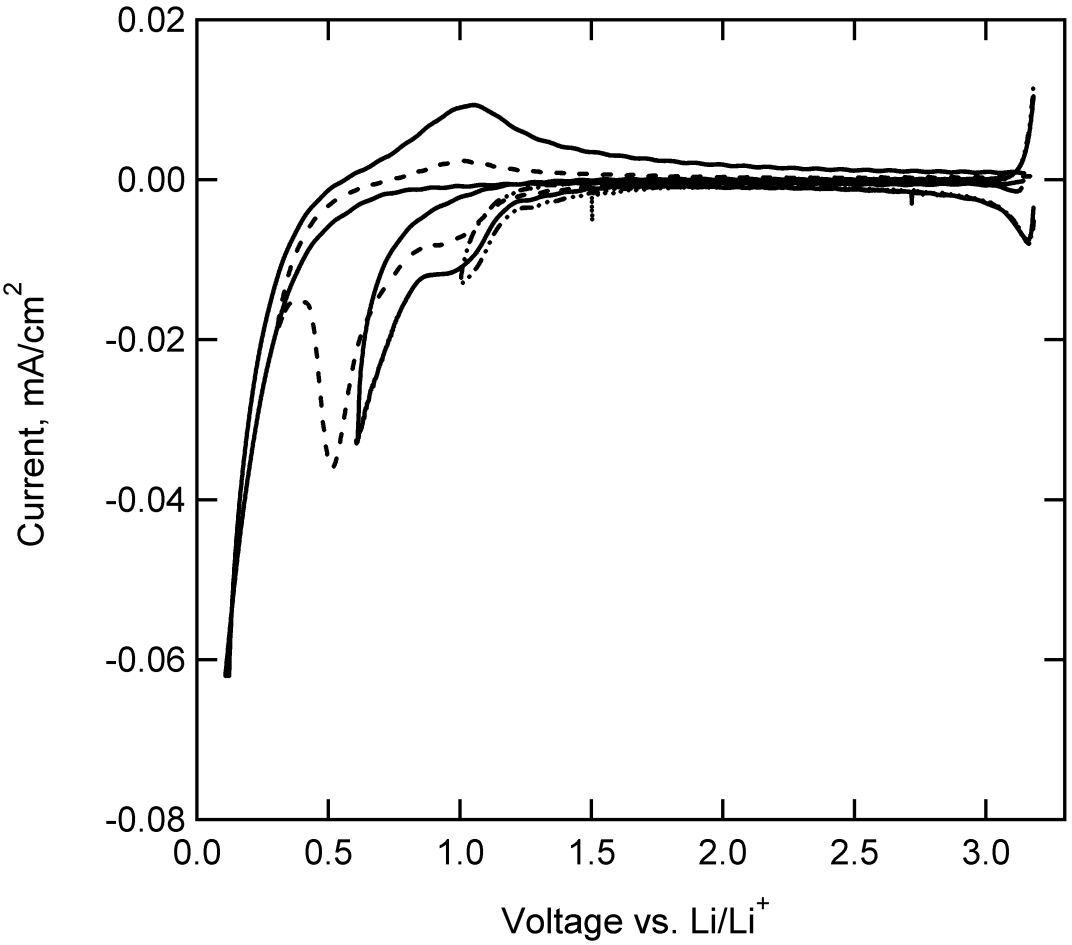

Figure 4.7: SEI formation in $LiClO_4$, cycling to variable voltage limits at 10 mV/s. Location of peaks is the same as in Fig. 4.4. $f_e = 0.02$.

reaches 3.7 V. Although this current could be ferrocene oxidation, it could also be oxidative stripping of the SEI, which occurs above 3.5 V on glassy carbon [49, 16]. The large oxidation peaks in Fig. 4.8 at 3.2 V are artifacts of the cycling protocol, which was defined in terms of the open-circuit potential. Because the relative concentrations of ferrocene and ferrocenium at the surface varied with time and potential, E^0 drifted during experiments. Although the drift was typically less than 20 mV, it caused the potentiostat to apply an abrupt step change in the potential at the start of the diagnostic CV and, thus, to measure a large and rapidly decaying current due to double-layer charging. Although the magnitude of the current at 3.2 V in Fig. 4.8 is high, it decays rapidly, in a manner consistent with double-layer charging. Furthermore, the curves measured after formation above 0.6 V show no changes to either the potential or magnitude of the peak ferrocene current, indicating that the current is nonfaradaic and does not affect the ferrocene measurement.

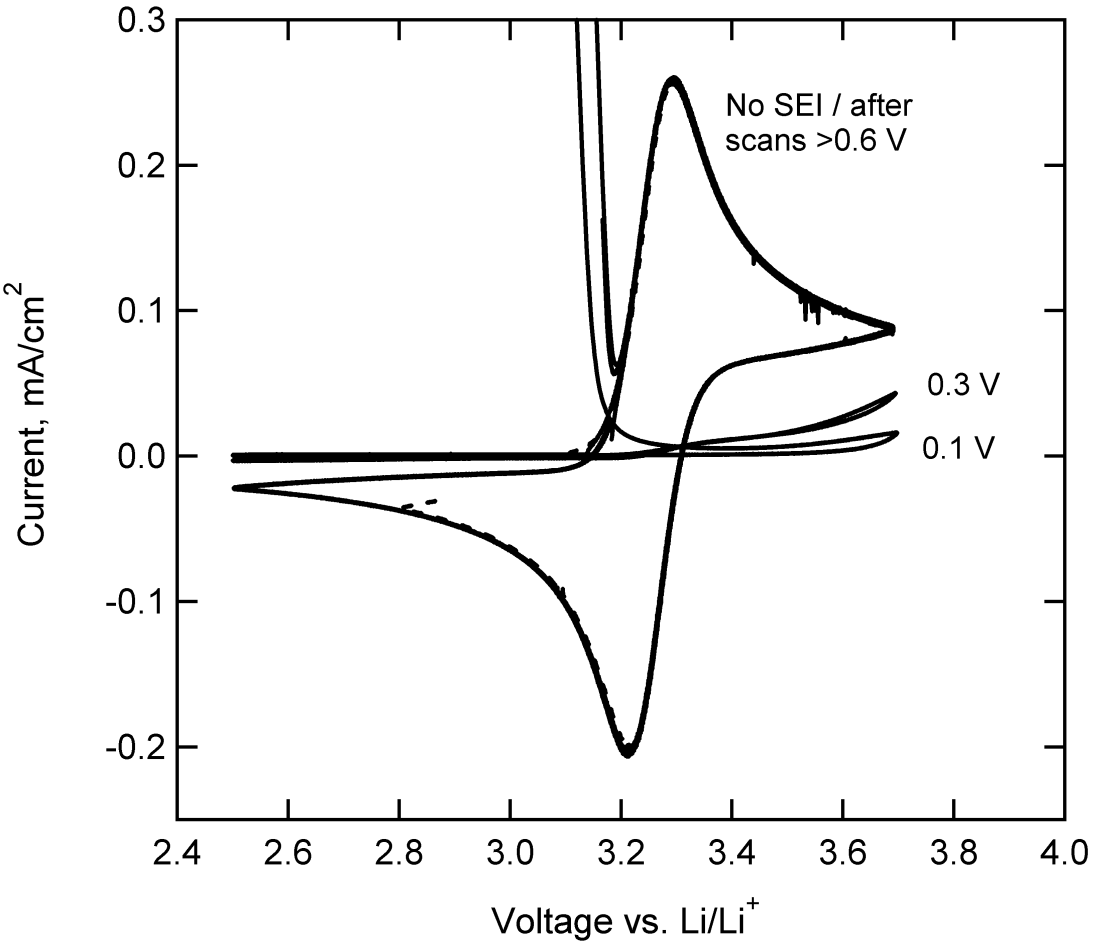

Figure 4.8: Effect of SEI formation on ferrocene CV in $LiClO_4$, variable formation voltage. No change in through-film ferrocene reaction is seen until the formation voltage decreases below 0.6 V, after which the ferrocene reaction is almost entirely suppressed. The dashed line showing the ferrocene current before SEI formation is hidden underneath curves measured after formation, showing the complete lack of electronic passivation above 0.6 V.

The Nyquist plot in Fig. 4.9 corroborates the difference between SEI formation above and below 0.6 V. The impedance before SEI formation is shown by the dashed line in (a). The 45^o slope and lack of high-frequency semicircle show a fast reaction. After SEI formation, EIS spectra show a similarly fast reaction until after the formation cycles to 0.3 and 0.1 V, when the charge-transfer resistance rapidly increases (Fig. 4.9b). Although the charge-transfer resistance increases greatly after SEI formation, the real intercept at high frequency does not increase with cycling. The rapid changes in the ferrocene CV and EIS measurements between formation to 0.6 and 0.3 V show that, even though the SEI begins to form at 1.0 V in $LiClO_4$-electrolyte (Fig. 4.7), it does not provide electronic passivation until the formation

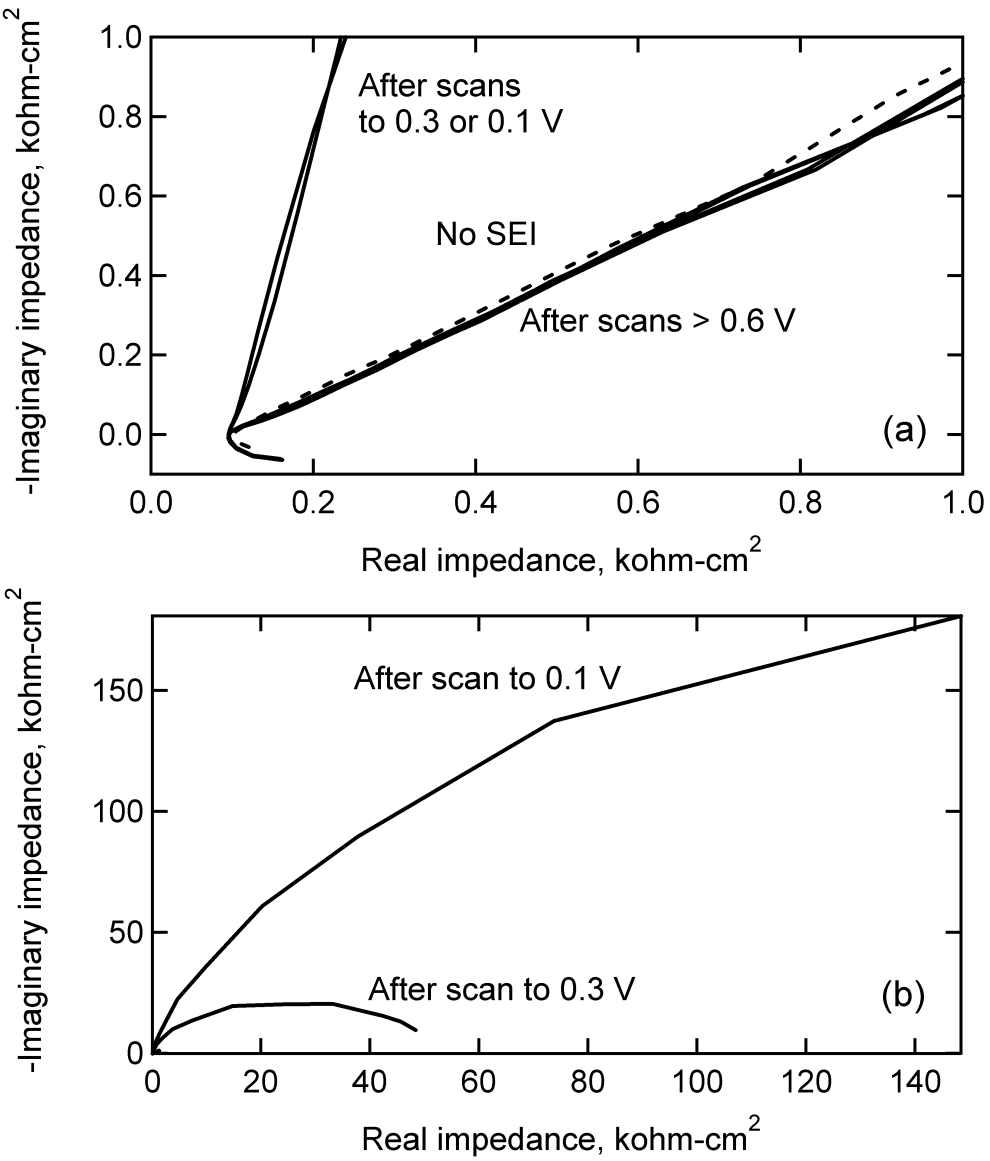

Figure 4.9: Effect of SEI formation on ferrocene EIS in $LiClO_4$, variable formation voltage. EIS shows an extremely fast reaction on the clean HOPG electrode and until the formation voltage decreases below 0.6 V. The real intercept does not change with SEI formation.

potential decreases below 0.6 V, upon which it blocks electron transfer very rapidly. It is unclear from the experiments whether the difference above and below 0.6 V is caused by a difference in reaction products or simply because the formation reactions have not occurred enough to cover the electrode.

Effect of solution contamination

In this study, water contamination was a major concern because f_e was measured using aqueous KCl. In order to keep a constant electrode area, the cell was not disassembled while drying. Thus, although the electrolytes used were battery-grade chemicals with extremely low water content, trapping water in the O-ring during cell drying remains a possibility. Aurbach et al. found that water reduction occurs in nonaqueous electrolytes at approximately 1.5 V vs. lithium [67]. Although the SEI formation spectra in Figs. 4.4 and 4.7 do not show any clear peaks at this potential, the high scan rate employed (20 mV/s) may measure slow reactions such as water reduction beginning at lower potentials. Thus, the reduction processes in Figs. 4.4 and 4.7 beginning at approximately 1.0 V may involve the reduction of trace water as well as electrolyte.

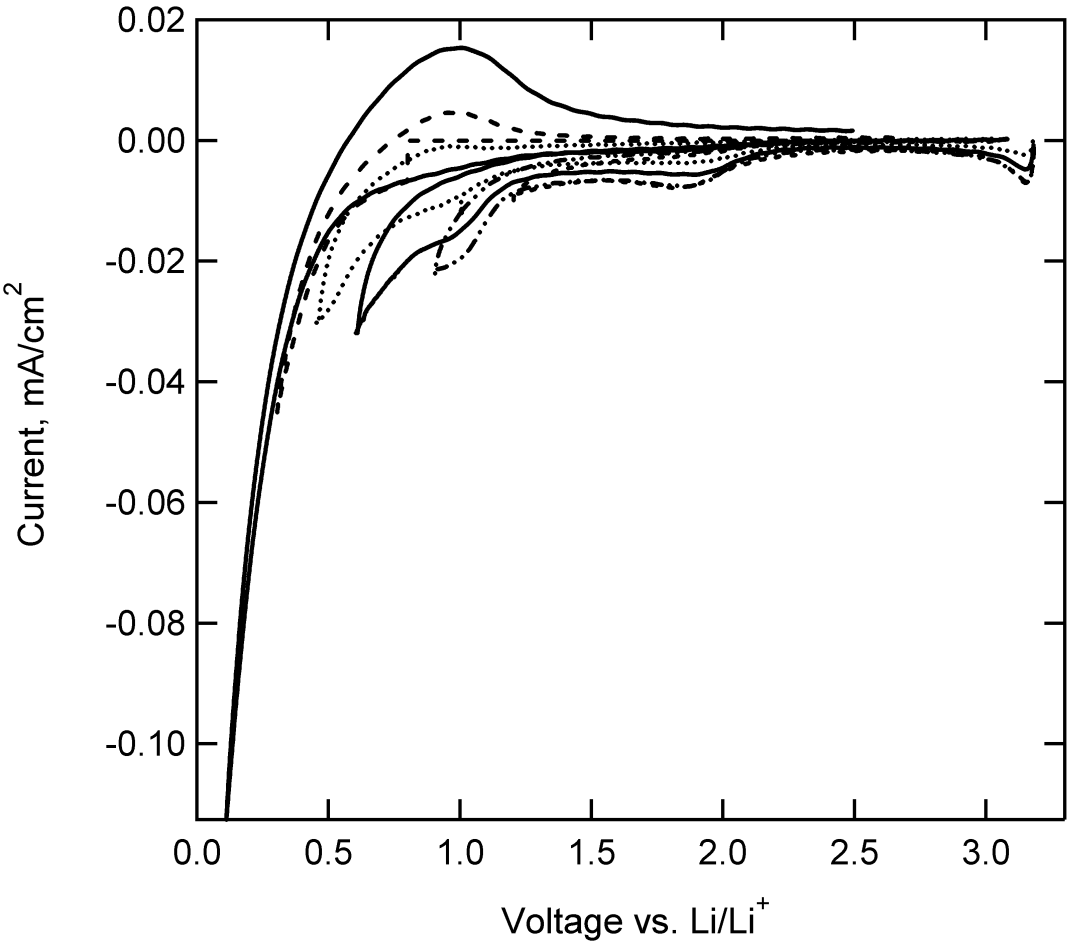

Figure 4.10: SEI formation in $LiClO_4$, 10 mV/s. The 1.9 V reduction peak indicates oxygen contamination. Formation currents are higher at all currents than they are in the absence of the 1.9 V peak as in Fig. 4.7. $f_e = 0.002$.

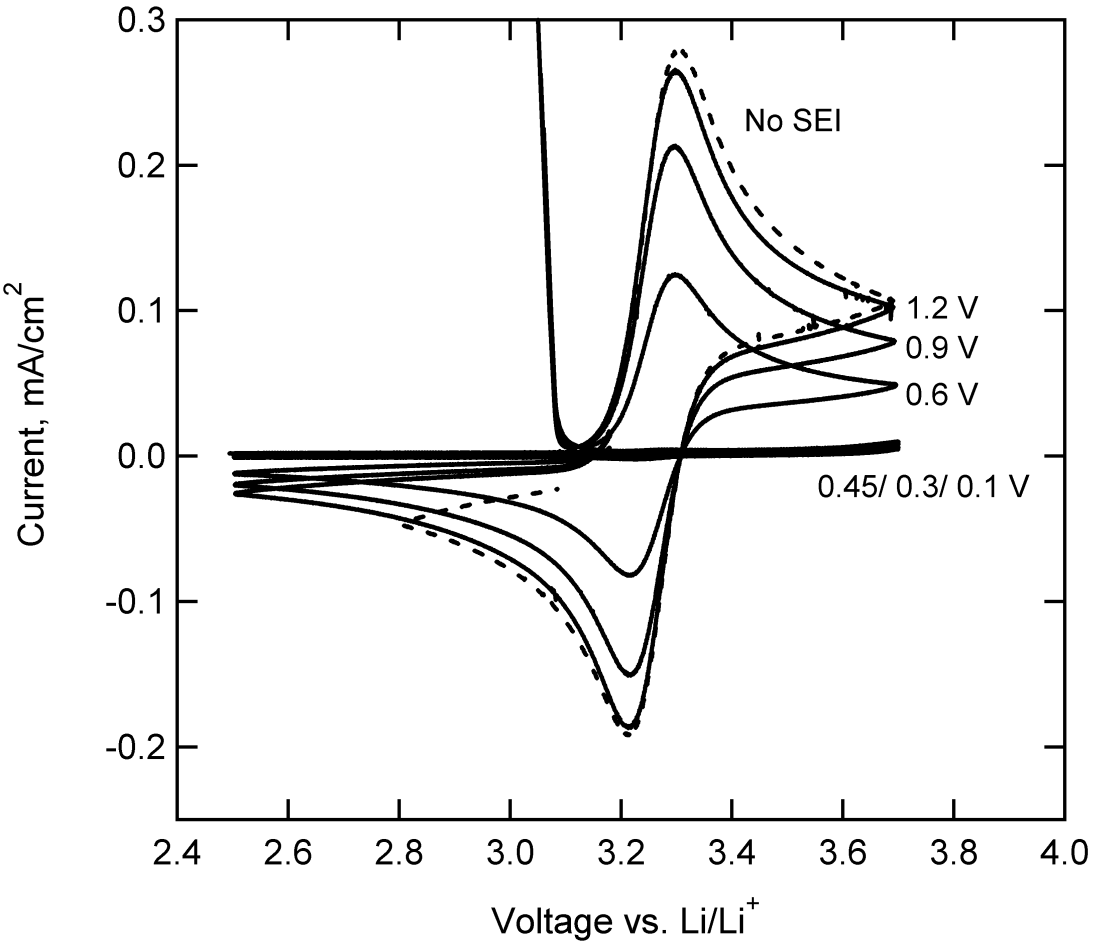

Figure 4.11: Effect of SEI formation on ferrocene CV in $LiClO_4$, oxygen contamination. In comparison to Fig. 4.8, the through-film ferrocene current decreases at all formation voltages, showing that HOPG is passivated more rapidly when the contaminant is present.

While the use of aqueous solutions in this work suggests that water is a possible contaminant, reduction of oxygen is also known to occur between 2.1 and 1.6 V vs. lithium [67]. Fig. 4.10 shows an experiment in which a 1.9 V reduction peak is observed. This peak occurred erratically and was not correlated to C_{dl} or f_e, suggesting a contaminant, and the location of the peak at 1.9 V suggests oxygen. The electrode in Fig. 4.10 was cycled to 1.2, 0.9, 0.6, 0.45, 0.3, and 0.1 V vs. Li/Li$^+$. Comparing Figs. 4.8 and 4.9 with Figs. 4.11 and 4.12 shows how oxygen causes HOPG to become passivated more quickly. When the 1.9 V peak is present, SEI formation current is generally larger at all voltages. Ferrocene current begins to decrease immediately after SEI formation cycling to 1.2 V, whereas the ferrocene CV in Fig. 4.8 shows no effects until 0.6 V. EIS data show a similar effect; the rise in charge-transfer resistance occurs earlier and more rapidly in contaminated electrolytes.

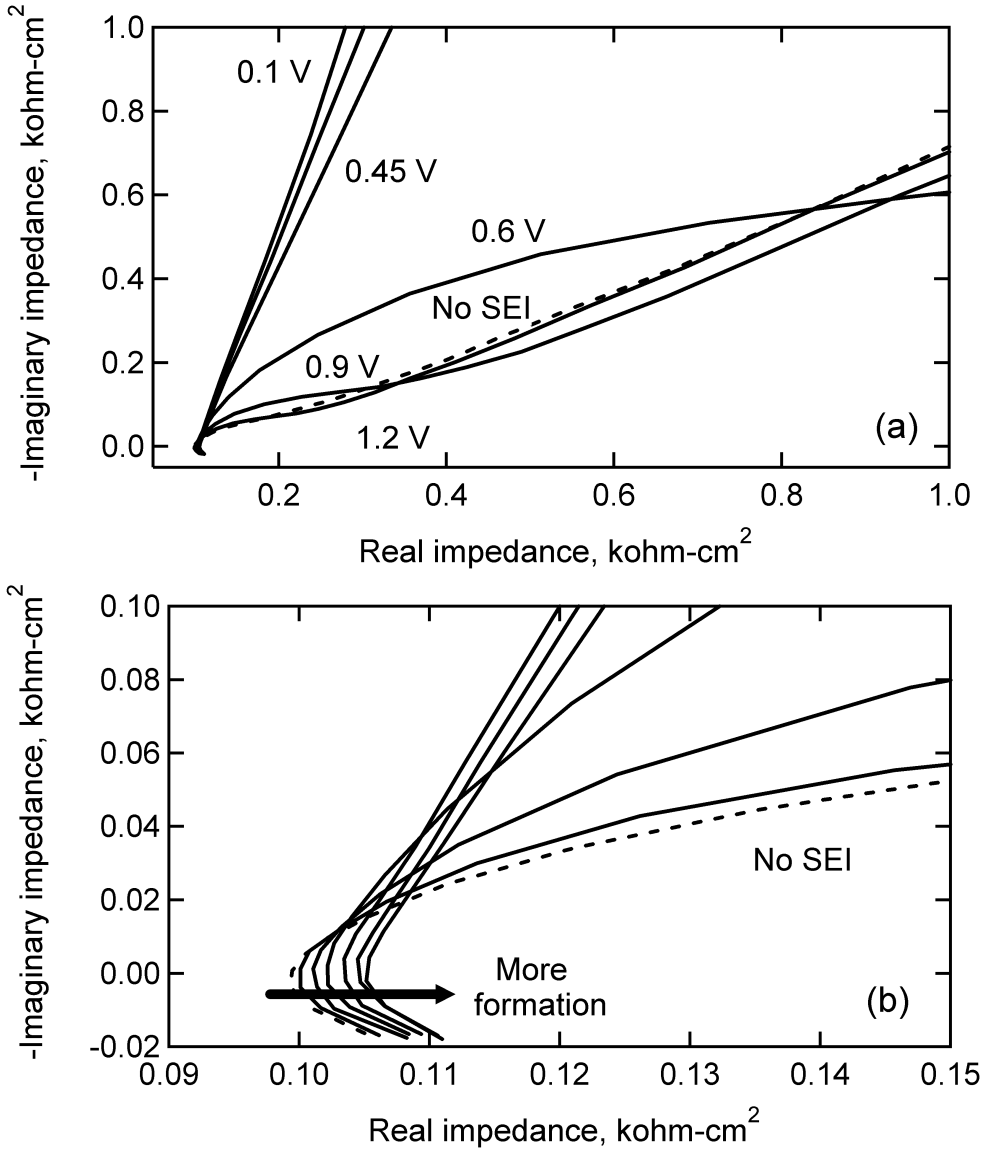

Figure 4.12: Effect of SEI formation on ferrocene EIS in $LiClO_4$, oxygen contamination. The rise in charge-transfer resistance occurs earlier and more rapidly than in Fig. 4.9. Zooming in on the real intercept shows that, reaction products formed in the presence of the contaminant are more ionically, as well as electronically, resistive.

EIS also shows that, as more SEI is formed, the real intercept increases from 0.0995 to 0.1052 kohm-cm^2. Thus, the reaction products formed in the presence of the contaminant are more ionically, as well as electronically, resistive. These observations are consistent with the predicted products of either oxygen or water reduction. In carbonate solvents, McCloskey et al. found that the primary product of oxygen reduction was Li_2CO_3, while Aurbach found

that water was reduced to LiOH [68, 67]. Both compounds should be both less soluble (and thus more passivating) and less ionically conductive than polymer-like reduction products of the carbonate solvent [67, 69]. Thus, the effects of the contaminant on the ferrocene CV and impedance do not by themselves specify the electrochemical reactions. To identify the reaction products accurately, spectroscopic or other nonelectrochemical methods are necessary. Although f_e in Fig. 4.7 was measured as 0.002, the deintercalation peak at 1.0 V is larger than the basal plane sample in Fig. 4.4, which has a calculated value of $f_e = 0.02$. However, the measured values of C_{dl} for the two samples differ by less than 1 μF/cm^2, attesting to the difficulty of accurately measuring f_e by this method when f_e is low and C_{dl} is small.

The characteristic parameters of impedance spectra, the high-frequency arcwidth and time constant, provide only a comparative measure of passivation because both kinetic and transport resistances from the SEI affect the parameters in the same way [61]. The characteristic measurements from CV, the peak current height and peak potential separation, can sometimes give mechanistic information about the mechanism of passivation; for example, increased peak splitting is most commonly attributed to a slower rate constant, while a reduced peak current is attributed to a mass-transfer limitation. At formation voltages 0.6 V and higher, the data in Fig. 4.11 show a decreasing peak ferrocene current, and no change in peak potential splitting. This indicates that the kinetics of the ferrocene reaction do not change, and that the change in current is caused by either a decrease in active area (a partially blocked electrode) or by the formation of a porous layer that slows diffusion. Distinguishing between these two mechanisms from the cyclic voltammagram is difficult, if not impossible. After formation to 0.45 V or lower, charge-transfer to ferrocene in Figs. 4.8 and 4.11 is so completely blocked that no peak current or peak potential can be observed. Therefore, the results of Figs. 4.10 to 4.12 cannot provide conclusive information about the mechanism of passivation, although they do provide a useful qualitative metric.

Comparison of $LiClO_4$ and $LiPF_6$-based electrolytes

The potentiodynamic experiment in Fig. 4.4 was repeated in 1.0 M $LiPF_6$ EC:DEC to compare the effect of fractional edge plane in the presence of a different salt anion. The HOPG electrodes were again cycled from open circuit, to 3.7 V, to 0.1 V vs. lithium three times at 20 mV/s. Fig. 4.13 shows two representative trials on the basal plane ($f_e = 0.01$) and the edge plane ($f_e = 1.0$). Comparison with Fig. 4.4 shows that the SEI formation behavior is extremely different between the two electrolytes. On the basal plane, the CV exhibits additional peaks at 0.8 and 0.45 V that are not seen in $LiClO_4$-based electrolyte. Additionally, in $LiClO_4$ solutions, the SEI formation peaks disappear completely after the first cycle, but in Fig. 4.13a, the SEI formation peak at 0.45 V is still visible. Further cycling (not shown) was able to suppress the formation peaks and reach a steady-state profile after approximately 8 to 10 cycles. On the edge plane (Fig. 4.13b), the location of the single peak is similar in the two electrolytes. However, passivation is not completed after a single cycle as it is in Fig. 4.4, although it appears to be faster on the edge than the basal plane. The slower passivation in $LiPF_6$-based electrolyte may be due to a number of factors. Aurbach

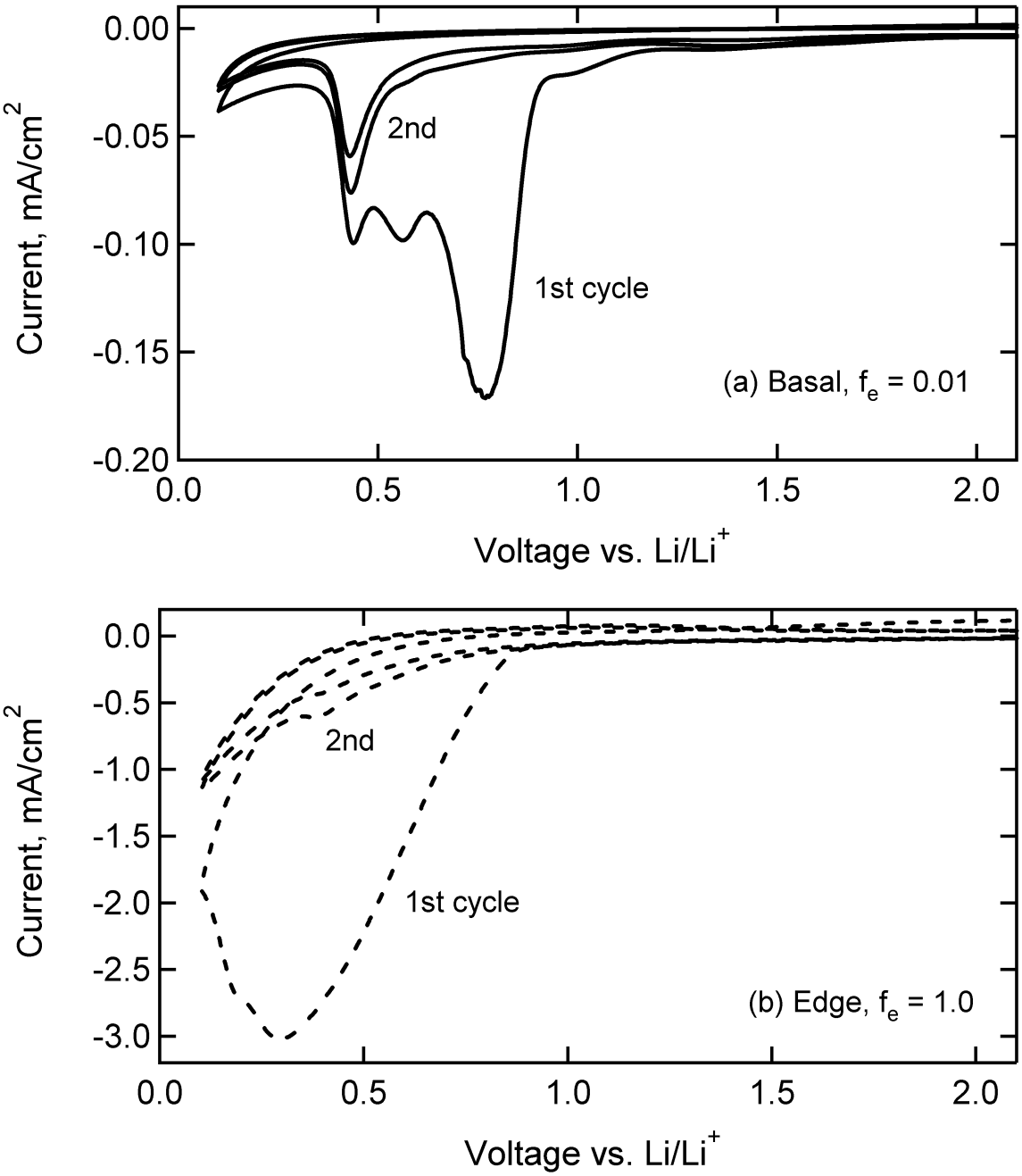

Figure 4.13: SEI formation in 1:1 EC:DEC 1.0 M $LiPF_6$ on edge and basal planes. (a) shows a sample with $f_e = 0.01$, while (b) shows the edge plane, f_e= 1.0. Scan rate is 20 mV/s. The voltammetric response is very different from $LiClO_4$-based electrolyte (Fig. 4.4), both in the location and magnitude of peaks. Passivation is also much slower.

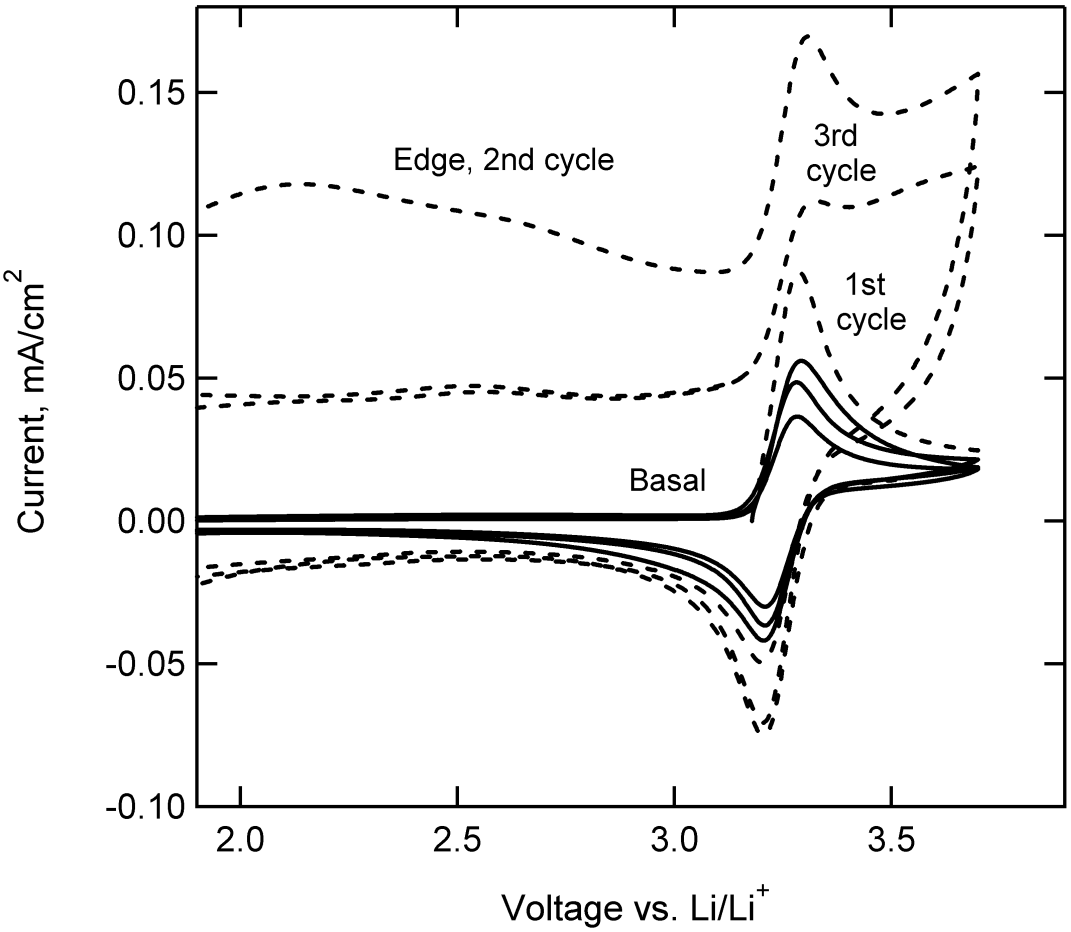

Figure 4.14: Effect of SEI formation on ferrocene CV in 1.0 M $LiPF_6$ in EC:DEC. On the basal plane, passivation is much slower than in $LiClO_4$-based electrolyte. On the edge plane, the SEI is oxidized at voltages greater than 2.1 V, as shown by currents larger than the reversible ferrocene current. Because the film is removed in the potential range of the ferrocene reaction, ferrocene CV cannot be used to compare electronic passivation on the edge and basal planes.

et al. proposed that HF, an unavoidable contaminant in $LiPF_6$-based electrolytes, reacts with and dissolves carbonate reduction products on the electrode surface; such dissolution reactions would slow the rate of SEI formation until more stable products were formed [56, 57]. Another possibility is that PF_6^- slows the precipitation kinetics of SEI products, causing slower passivation; the identity of the anion has been shown to affect precipitation kinetics in previous work [43]. The overall magnitude of the SEI formation current on the basal plane is similar in the two electrolytes, consistent with a recent study by Marom et al., who compared $LiPF_6$ and $LiClO_4$ on platinum electrodes [57]. On the edge plane, the measured

SEI formation current is approximately five times higher than that in $LiClO_4$ electrolyte, consistent with the higher value of f_e in Fig. 4.13b than in Fig. 4.4b (1.0 vs. 0.30).

The high-voltage behavior of the experiment in Fig. 4.13 is shown in Fig. 4.14. Initially, the peak potential separation for the ferrocene reaction is 77 mV on the basal plane and 65 mV on the edge plane. The peak ferrocene current is substantially higher on the edge plane, even though the superficial area, concentration, and scan rate are the same. This results suggests that, for this trial, scratching the electrode may have increased the microscopic surface area by roughening in addition to exposing more edge sites. However, the ferrocene peak current increases by approximately 55%, while the SEI formation and lithium de/intercalation currents increase by factors of 18 to 120, showing that surface roughness cannot be the only factor influencing the measurements. On the basal plane (solid line), the peak ferrocene oxidation and reduction currents decrease slightly with each cycle, and the peak potential separation remains nearly constant. Although the passivation is much slower than in $LiClO_4$-based electrolyte, the overall behavior is consistent with that in Fig. 4.11, which shows gradual passivation due to formation of a porous layer or partial blocking of the electrode.

The edge plane, in contrast, shows a dramatically different electrochemical response. On the second cycle, a large oxidation current is seen even below 2.0 V. This current shows a maximum at approximately 2.1 V, then peaks again at the location of the ferrocene peak potential and again at the upper scan limit of 3.7 V. Because the peak current is higher than that observed with no SEI, the oxidation current must correspond to oxidative stripping of SEI products from the electrode. Removal of SEI products explains why the reduction peak for ferrocenium on the second cycle is almost unchanged from that on the electrode without an SEI. As the electrode is cycled a third time, the decreased height of the oxidation and reduction peaks show that the ferrocene reaction is suppressed. Although the high current on the second cycle shows the oxidation of SEI products, the formation peak is still suppressed greatly from the first to second cycle in Fig. 4.13, showing that the oxidation reaction at high voltage does not completely remove SEI products. The partial removal of the film at high voltages complicates any comparisons between electronic passivation on the edge and the basal planes. The oxidative stripping of the edge-plane SEI in Fig. 4.14 was observed consistently over seven trials of the experiment. Stripping of the basal-plane SEI was minimal, occurring only to an extent consistent with a small but nonzero value of f_e. Bar-Tow et al. found that the edge-plane SEI was richer in inorganic compounds while the basal-plane SEI was richer in organic compounds [9]. A possible explanation for the behavior in Fig. 4.14 is that organic SEI products are oxidatively stabler. Previous work found that the SEI in $LiPF_6$-based electrolyte was also oxidized at high voltages; the oxidative removal of SEI products on the edge, but not basal plane, suggests that electrolyte reduction products formed on glassy carbon are more similar to those formed on the edge plane [49].

In the previous study, SEI products on glassy carbon were not oxidized until above 3.5 V, whereas Fig. 4.14 shows oxidation occuring at 2.1 V and higher. The difference betwen this and the previous study may be due to the different nature of the surface, or to the fast scan rate employed for these experiments (20 mV/s) in comparison with the 0.6 V potentiostatic

formation in the previous work. We hypothesize that, at faster formation rates, intermediate SEI products do not have time to form stabler compounds and are more easily oxidized than they are during potentiostatic formation. Preliminary experiments found that decreasing the scan rate from 20 mV/s to 2 mV/s decreased the magnitude of the oxidative current, but did not eliminate the stripping reactions. Future work should study in more detail the effect of scan rate on SEI formation and behavior in $LiPF_6$-based electrolyte.

4.3 Conclusions

Potentiostatic experiments show that electrochemical activity is higher on the edge than the basal plane of graphite, in agreement with literature results. At a constant potential of 0.6 V vs. lithium, current increases with increasing fractional edge plane density. Plotting formation charge vs. square root of time suggests transport-limited growth, regardless of the value of f_e. Glassy carbon exhibits similar behavior under the same conditions, although the measured value of f_e and the measured rate of film growth are not consistent with the correlation for that on HOPG. During potentiodynamic SEI formation experiments, the edge plane exhibits higher currents for both SEI formation reactions, which appear only on the first cycle, and for lithium de/intercalation currents, which reach a steady-state profile for oxidation and reduction.

Including ferrocene in the electrolyte permits in-situ monitoring of the degree to which an electrode is electronically passivated. In $LiClO_4$-based electrolyte, higher through-film ferrocene currents on the edge plane show that, despite greater SEI formation currents, the film formed on the edge plane is less passivating than that formed on the basal plane. The presence of oxygen contamination leads to an SEI that forms and passivates faster. The SEI forms more slowly in $LiPF_6$ than in $LiClO_4$-based electrolyte. On the edge plane, SEI products of $LiPF_6$ reduction are oxidized at voltages greater than 2.1 V. The difference between $LiPF_6$-based and $LiClO_4$-based electrolytes points to the importance of the anion in passivation behavior.

The CV of ferrocene as the SEI is formed at different voltages shows a decrease in peak current, but no change in peak-potential splitting, indicating either a partially blocked electrode or a transport limit caused by a porous film. Considering the sensitivity of the measurements, conclusive mechanistic analysis to distinguish between a porous-layer model and an active-site model is not possible. Furthermore, the results presented here on SEI formation, which occurs over minutes and hours, may not be directly applicable to SEI growth, which occurs over months and years and is responsible for capacity fade. The possibility that slow passivation in $LiPF_6$-based electrolyte is due to slow precipitation kinetics may also preclude the use of any planar electrode, such as HOPG, for SEI studies. The surface area : electrolyte volume is much higher when using porous electrodes of composite graphite, meaning that reactive intermediates cannot diffuse into a reservoir and will thus reach saturation concentrations and precipitate faster. However, the relative ease of the method and the observations in this work suggest that ferrocene has great utility as a qualitative indi-

cator of electrode passivation in realistic battery systems. Future work will continue to use ferrocene to study the effect of different electrolytes on electrode passivation.

Chapter 5

Atomic-force microscopy measurements

Although the method developed in Chapters 2 to 4 provides useful information about the SEI formed on glassy carbon, Chapter 3 shows that there is no unique set of parameters used to fit the impedance data, and even in the steady-state measurements, multiple combinations of k_0, τ, L, and ϵ may give values of $i_{\mathrm{lim},f}$ and k_{eff} that describe the data. In this chapter, we attempt to validate our electrochemical data using nonelectrochemical characterization techniques on the SEI. Atomic-force microscopy (AFM) and scanning electron microscopy (SEM) were performed by Dr. Ivan Lucas at Lawrence Berkeley National Laboratory.

AFM has been used in many previous studies of the SEI with substantial differences in experimental parameters and results. These studies have varied in the systems studied, the conditions under which the SEI is formed, and the thicknesses of films measured. Hirasawa, et al. formed the SEI galvanostatically at 63.7 μA/cm^2 in a solution of $LiClO_4$ in EC:EMC [52]. The SEI reached a thickness of 50 to 70 nm at potentials below 0.9 V. Alliata et al. grew an SEI in $LiClO_4$ in EC:DMC by scanning the electrode to low potential at 5 mV/s. Imaging during the scans, they found that formation of a 15 nm film began to occur at 0.7 V vs lithium. After a second CV cycle, the film became smoother and reached a thickness of 25 nm [55]. Chu et al. studied both $LiClO_4$ and $LiPF_6$ in EC:DMC on HOPG. Scanning the electrode to low potentials at 2 mV/s, they found film thicknesses of up to several hundred nm, with thicker films forming in $LiPF_6$-based electrolyte [53]. On inert electrodes, Aurbach et al. used electrolytes of $LiAsF_6$ and $LiPF_6$ in EC:DMC on gold. The SEI was formed by stepping the potential to decreasing potentials and waiting for the current to decay to zero before imaging. In the $LiAsF_6$ solution, electrolyte reduction products began to precipitate on parts of the electrode at 1.5 V. The film thickness at this voltage was 128 nm. As potential decreased, the film became slightly thicker and much less porous, reaching a final thickness of 148 nm at 0.5 V vs. lithium [43],

Although the studies by Alliata et al. and Chu et al. related the appearance of films to peaks in the voltammagram, we are not aware of any detailed analyses that relate the electrochemical data (charge vs. time) and the topographic data (the thickness). Furthermore, the

variation between studies demonstrates the importance of the specific electrolyte, electrode surface, and formation conditions to the film thickness. We thus attempt to replicate the SEI formation protocol of Chapter 4 on glassy carbon while monitoring in-situ the thickness of the film.

5.1 Experimental methods

Planar glassy carbon samples were obtained from Alfa Aesar. Before performing any electrochemical experiments, a pattern of alumina pillars was coated on the surface to provide a reference point for the height. First, the carbon was coated with poly (methyl methacrylate) (PMMA) and exposed to an electron-beam writer with the desired pattern. Layers of gold, silica, and finally alumina were then deposited on the sample for a total height of 80 nm. Gold and silica were necessary to improve adhesion between the electrochemically inert alumina and the glassy carbon. The PMMA was then removed by sonication in acetone. In-situ AFM was performed using a PicoSPM (Molecular Imaging) in a small Ar-filled environmental chamber. To compensate for electrolyte evaporation in the cell, an additional syringe of 1.0 M $LiPF_6$ EC:DEC electrolyte (Novolyte) was connected to the AFM cell. Lithium metal was the counter and reference electrodes. The electrode area was limited by an O-ring to 2.5 cm^2.

Because the time scale of AFM measurement may not be faster than SEI formation, the glassy carbon sample was polarized at 0.6 V for intervals of 5 to 60 seconds. The sample was then held at open circuit during the AFM scan, which was conducted in tapping mode with a scan speed of 0.5 lines per second. Each image took approximately 6 minutes to obtain.

After electrochemical experiments, the electrode was removed from the AFM cell, rinsed with diethyl carbonate to remove salt, and dried in air before imaging with a scanning electron microscope.

5.2 Results and Discussion

Figure 5.1 shows the glassy carbon sample imaged in the argon atmosphere before the introduction of electrolyte. An alumina pillar is identified by the square in the center of the image, while a height profile shows that the height of the pillar before SEI formation is 80 nm. After correcting for sample tilt, the profile is extremely flat. The area of the image is 20 μm $\times$ 20 μm. Figures 5.2 and 5.3 show AFM images as the electrode is polarized at 0.6 V. Fig. 5.2a shows the surface after electrolyte is introduced to the cell, but before polarization at 0.6 V. No difference can be seen between the electrode at open circuit and the electrode imaged in argon. Figures 5.2b through f show the electrode after polarization times of 5, 10, 30, 40, and 60 seconds, respectively. As the blue color becomes lighter, the difference in height between the red pillar and the glassy carbon surface decreases; thus, the SEI is increasing in thickness. The images also show that the film is rough, but more or

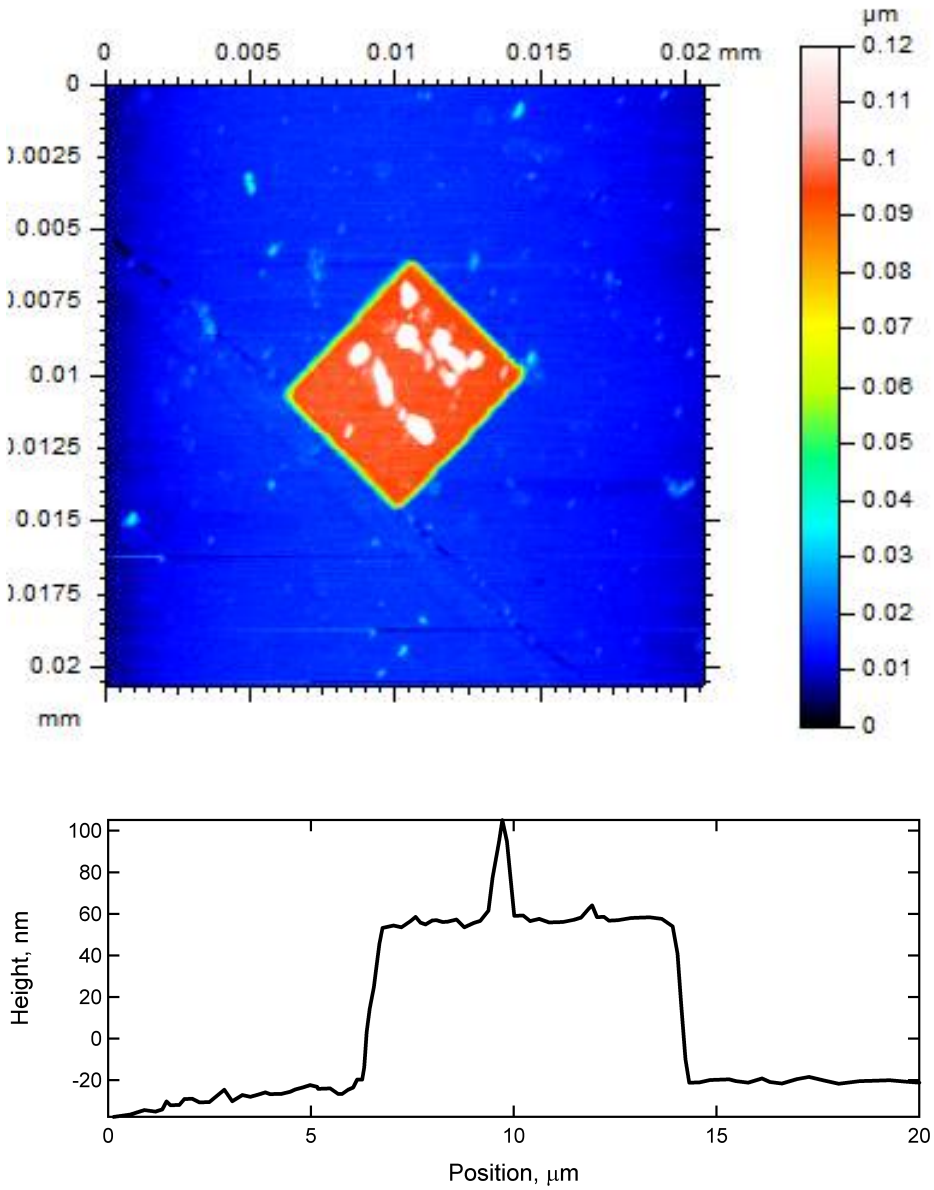

Figure 5.1: AFM image of glassy carbon in air. The square feature in the middle shows the alumina pillar. The top image shows the entire AFM, while the bottom is an example of a line scan across the center of the image.

less homogenous. The image at 60 seconds shows some inhomogeneities, but these are hard to separate from the effect of post-process flattening to correct for sample tilt. An average height, extracted from line scan data such as that shown in Fig. 5.1, is plotted vs. formation time in Fig. 5.4. The data points show that the thickness of the SEI increases fairly rapidly to approximately 20 nm in less than one minute of formation. This thickness is within the

range of thicknesses reported in the literature.

The total charge passed during the potentiostatic formation at 0.6 V is shown in Fig. 5.5. Stars mark the times at which the electrode was allowed to relax and AFM scans were taken. The x-axis of 'Formation time' does not include the relaxation time in which the AFM was measured. A potentiostatic formation curve on a RDE sample (Electrode C in Fig 3.2), without interruption, is also shown for comparison. For the first 90 seconds of passivation, the curve bends over, consistent with other experiments on glassy carbon. The magnitude of charges is also similar. However, at approximately 120 s, Fig. 5.5 shows a discontinuity in slope where the electrode ceases to exhibit passivation and the current starts to increase. The lack of passivation is accompanied by a change in the AFM images in Fig. 5.3a to f, shown at 90, 120, 150, 180, 240, and 300 seconds. Figs. 5.3a to c show a 20 μm $\times$ 20 μm sample while the image scale in d-f is 40 x 40 μm. The AFM images show gross inhomogeneities across the electrode, and very thick films. The average height in Fig. 5.4 shows an SEI thickness of up to 100 nm. Because of the wide inhomogeneities in Fig. 5.3, the post-imaging image processing may affect the measurement of the height after 120 seconds; thus, the reported number is only an estimate.

The thicknesses measured in Fig. 5.4 are higher than those reported by Hirasawa et al. and Alliata et al., but similar to those reported by Aurbach et al. and Chu et al [52, 55, 53, 43]. However, the lack of passivation after 90 seconds disagrees with our previous experiments on glassy carbon. Although very few, if any, previous studies have formed the SEI potentiostatically, we are also unaware of any similar reports in the literature. To determine whether the AFM itself interfered with the process of SEI formation, the electrode was imaged using SEM after the film-formation experiment. Post-experiment SEM images are shown in Fig. 5.6. The square patch in the corner of Fig. 5.6a) shows that, in the region where AFM experiments were performed, the SEI is removed from the electrode. Fig. 5.6b) shows this region in greated magnification. Thus, the tip interacts with the film and complicates any measurement of the thickness in Fig. 5.4. This observation is consistent with the work of Chu et al., who found that the SEI formed in $LiPF_6$ was softer than that in $LiClO_4$, and the tip was able to push around and relocate soft deposits [53].

Although interaction between the SEI and the AFM tip may explain unusually thick films, the section of the electrode imaged is at most 1600 μm^2, or 6.4×10^{-4}% of the 2.5 cm^2 surface; thus, interaction with the AFM tip cannot explain the lack of passivation exhibited by the entire electrode in Fig. 5.5. This lack of passivation was observed over multiple trials in the AFM and always occured after approximately two minutes of polarization at 0.6 V. Several possibilities for the lack of passivation exist:

1. The relaxation step, during which the AFM scans were performed, allows the SEI to undergo reactions in some way that promotes dissolution.

2. SEI formation reactions are known to evolve ethylene and other gases as decomposition products of carbonate solutions [70]. If these gases nucleate and form bubbles, the bubbles could affect the AFM cell, which faces up, differently than the rotating disk electrode, which faces down.

3. The lithography treatment used to add pillars to the surface affects the glassy carbon surface in a way that affects either the adhesion properties of the SEI, or the formation reactions themselves.

4. Because the gold layer of the alumina pillars would oxidize at high voltage, the carbon sample was not cycled at high voltage before the passivation hold. This may affect the glassy carbon surface differently, either in the adhesion or in the reactions themselves.

To test the possibility that Item 1 was the reason for the lack of passivation, the RDE was passivated in a similar manner to the AFM experiment, with potentiostatic holds of 0.6 V applied for the same intervals of 5 to 30 seconds as in the AFM experiment and relaxations of 5 minutes between holds. The resulting Q-t data, along with a comparison hold at 0.6 V for four minutes without interruption, is shown in Fig. 5.7a). The magnitude of charge is similar to the AFM experiment (Fig. 5.5) for the first 120 seconds / two minutes, and is higher than the comparison hold at constant potential. Measuring higher reduction currents for the interrupted than uninterrupted SEI formation makes sense, because applying a step change in potential will cause a double-layer charging current at short time. After each relaxation, this nonfaradaic current will be repeated, causing the total charge to be higher. Additionally, any concentration gradients affecting the electrolyte reduction kinetics will relax during the open-circuit periods and cause a higher current during the film formation steps. Despite the higher current, however, the interrupted formation shows consistent passivation through the formation holds, showing that relaxation does not cause reorganization reactions that permit film dissolution.

To test the possibility that that the orientation of the cell affected the passivation (Item 2), or that the electrode surface pretreatment was responsible for the lack of passivation in the AFM experiment (Item 3 and 4), the same polarization experiment was performed on two planar glassy carbon samples. One of the samples was not exposed to the lithography process; this electrode was cleaned with DMC and cycling before passivation. The other glassy carbon sample had been exposed to the photoresist process and etched with the alumina patterns, but not yet polarized in the AFM experiment. This sample was not cycled at high voltage before polarization. The cell design was the same as in Chapter 4; thus, the orientation was face-up, as in the AFM experiments. These results are shown in Fig. 5.7b) for polarization interrupted at 5 to 30 second intervals. The uninterrupted polarization curve for a sample without photoresist treatment is also shown. None of the three curves shows the nonpassivating effects seen in the AFM cell, where current starts to increase after 90 seconds. The measured current density is also much higher than on the RDE or in the AFM cell. In the RDE or the AFM cell, the total charge passed after 200 seconds of passivation is 3 to 4 mC/cm^2, whereas on the planar glassy carbon samples, the total charge is over 12 mC/cm^2.

The results of Fig. 5.7 show clearly that passivation is possible whether an electrode is oriented face-up or face-down, and that neither the photoresist treatment nor the cleaning procedure of cycling at high voltage is responsible for the lack of passivation in the AFM

experiment. However, the huge discrepancy (a factor of 3 to 4) between the magnitude of charge passed for the same experiment on the same materials in two different cell configurations is unsettling. Significant sample-to-sample variation was shown in Chapter 3 (Figs. 3.2 and 3.4); however, the magnitude of the difference between the planar sample and the RDE data is much larger than the differences between polarization curves in a) and b) of Fig. 5.7. In previous work, some of the RDE samples exhibited 'breaking-in' periods, where the electrode measured highly erratic currents for the first few weeks of experiments after it was purchased. Because the planar samples used for the AFM experiments and the experiments in Fig. 5.7 were not used repeatedly for months, in the same way that the RDE samples were, this "breaking in" effect could explain the discrepancy between the Q-t curves for the RDE and the other experiments. However, the AFM polarization agreed well with the RDE curve, at least for the first 90 seconds of polarization. Another possibility is that a material in the cell interferes with the results. Because of the stringent requirements for temperature control, the RDE must operate using a jacketed glass cell, whereas the HOPG cell is either polypropylene or Teflon. The HF formed from decomposing PF_6^- may attack glass cells and introduce silica impurities into the electrolyte [18]; however, little, if any, has been reported about the electroactivity of dissolved silica compounds in nonaqueous electrolytes. The AFM cell is also polypropylene, but several plastic and metal components of the AFM itself are in contact with the electrolyte during the experiment. One possibility for the lack of passivation in Fig. 5.5 is that some component in the AFM setup leaches into the electrolyte and reacts chemically with the SEI. More work is required to identify the discrepancies among test conditions and to identify the source of nonpassivating behavior in the AFM experiment.

5.3 Conclusions

In-situ AFM measurements were attempted to validate the electrochemical results for potentiostatic SEI formation on glassy carbon. However, characterizing the SEI is complicated and difficult. SEM images taken after the AFM experiments showed that the AFM tip removed the SEI, despite a small force constant and the use of tapping mode, not constant contact. Despite these interactions, measurements for the first 120 seconds of formation showed thicknesses of approximately 20 nm, in rough agreement with literature. After 120 seconds, current-time measurements showed a lack of passivation, which disagrees with the RDE and HOPG experiments in Chapters 2 to 4, as well as previous literature reports. Comparison with RDE and planar electrodes outside the AFM showed that the lack of passivation was not caused by gas evolution, film relaxation processes, or residues from the lithography process used to add pillars of constant height. Remaining possible explanations include variation in the glassy carbon samples themselves, or a contaminant leached from a material in the AFM cell. Future work should attempt to overcome these experimental problems in order to validate the previous electrochemical conclusions.

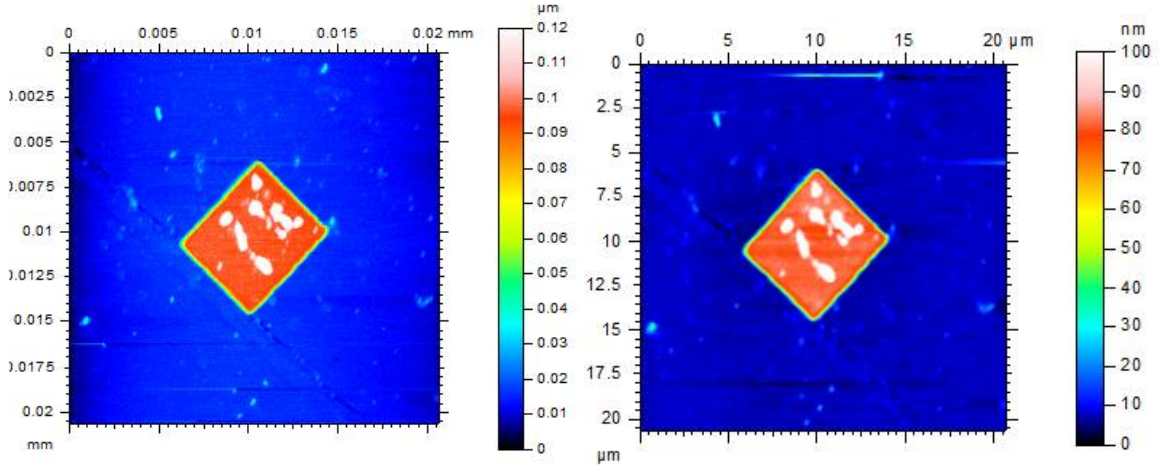

(a) AFM at open circuit

(b) AFM after 5 seconds

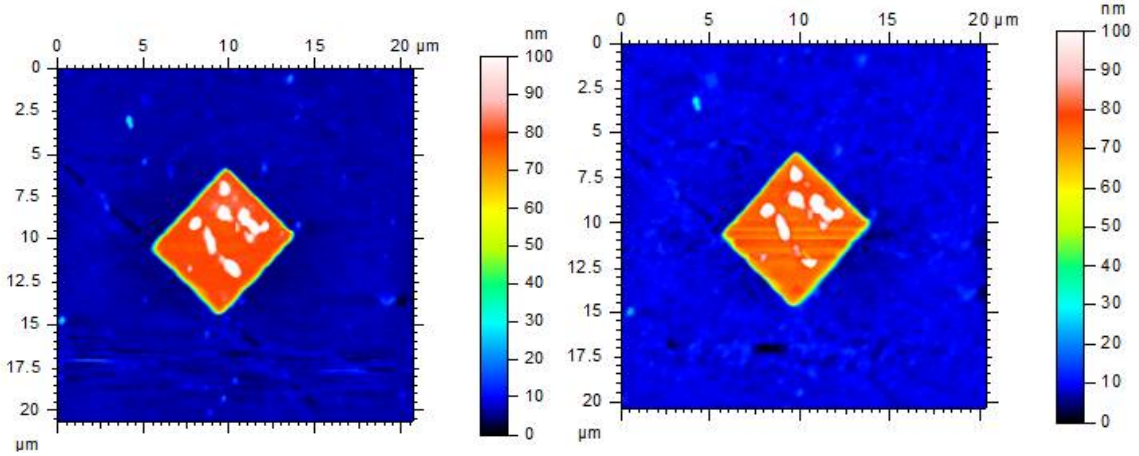

(c) AFM after 10 seconds

(d) AFM after 30 seconds

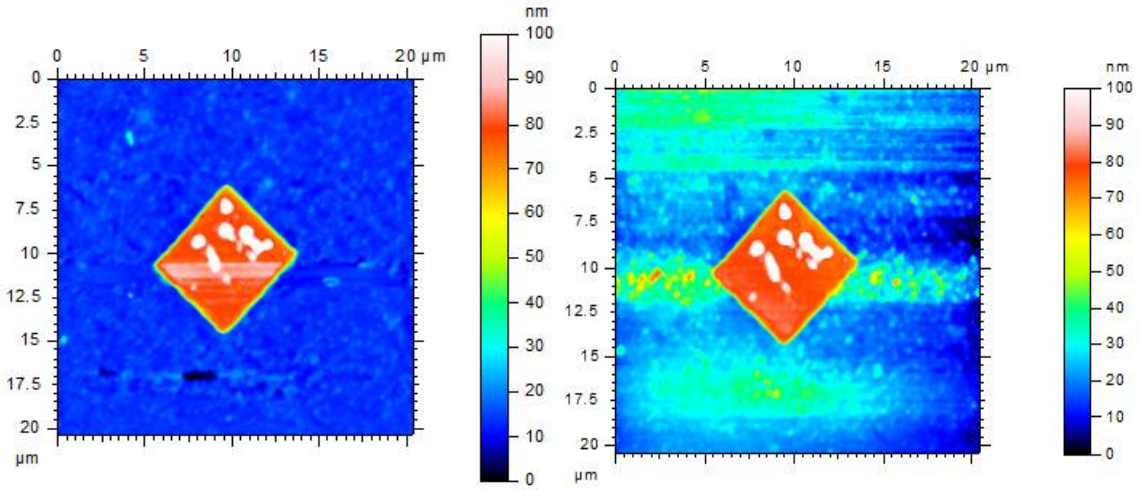

(e) AFM after 40 seconds

(f) AFM after 60 seconds

Figure 5.2: AFM images of film formation at 0.6 V, 0 to 60 s. The area of the image is 20 μm $\times$ 20 μm; the square in the middle is one alumina pillar.

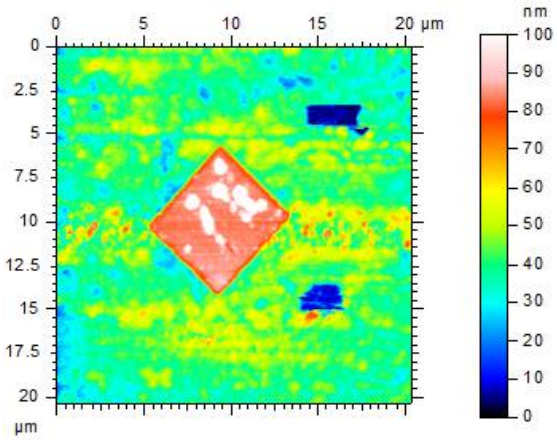

(a) AFM after 90 seconds

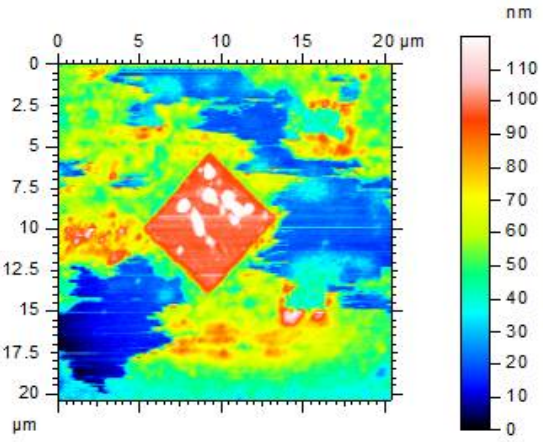

(b) AFM after 2 minutes

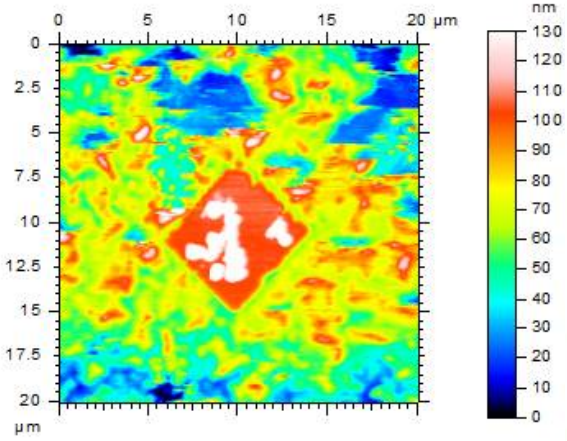

(c) AFM after 2.5 minutes

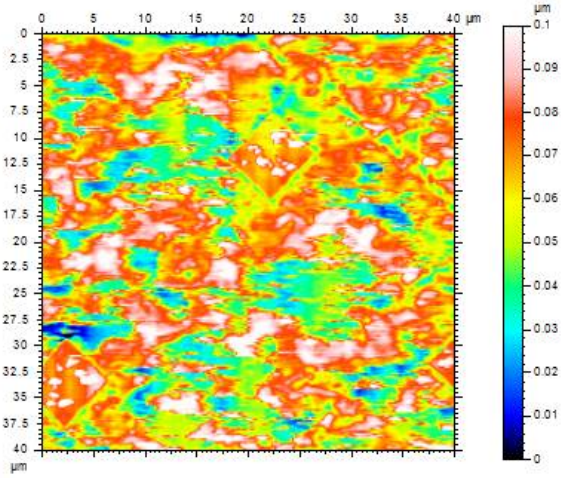

(d) AFM after 3 minutes

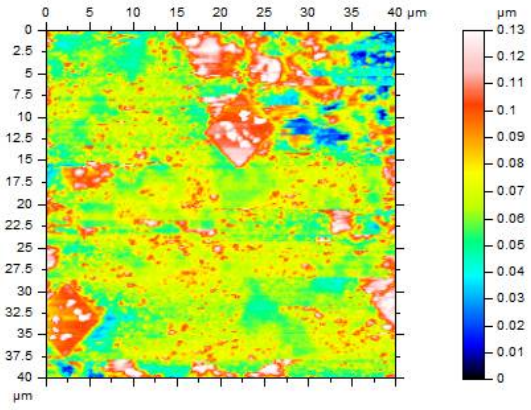

(e) AFM after 4 minutes

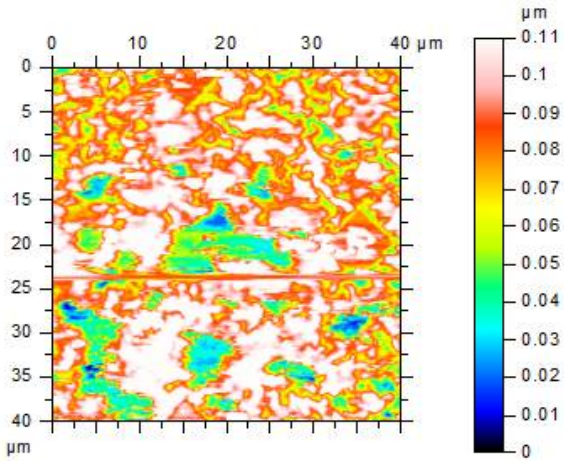

(f) AFM after 5 minutes

Figure 5.3: AFM images of film formation at 0.6 V, 90 to 300 s. In (a) through (c), the area of the image is 20 μm $\times$ 20 μm; the square in the middle is one alumina pillar. In (d) through (e), the area of the image is 40 μm $\times$ 40 μm; multiple alumina pillars are visible.

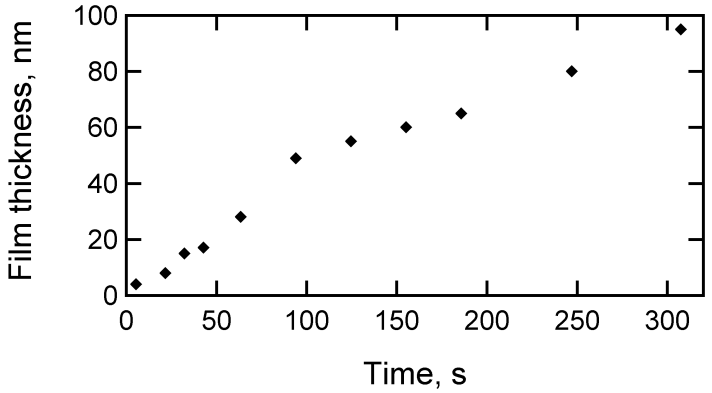

Figure 5.4: Thickness of film from AFM images. After 90 seconds of formation, the film becomes very nonuniform; see text.

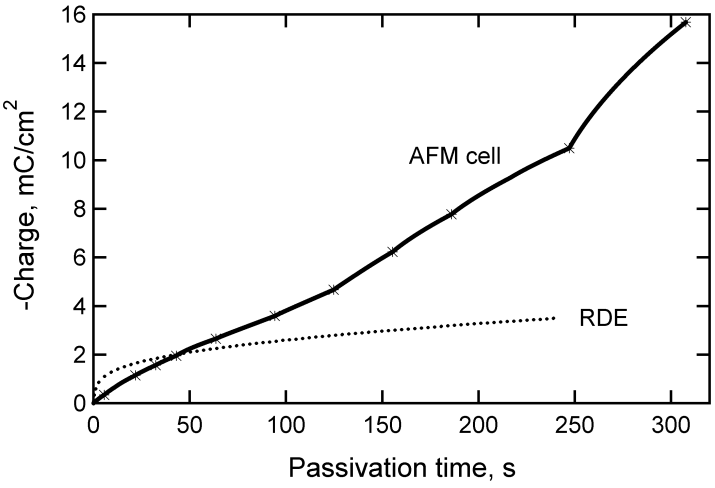

Figure 5.5: Q-t during SEI formation at 0.6 V, AFM measurements. Stars mark the times at which formation was interrupted for approximately 6 minutes while the electrode was imaged with AFM. The time spent imaging the electrode at open circuit is not included in the formation time on the x-axis. After approximately 120 seconds, current increases, showing that the film ceases to passivate the electrode. The dotted line shows a formation on the RDE (without interruption) for comparison.

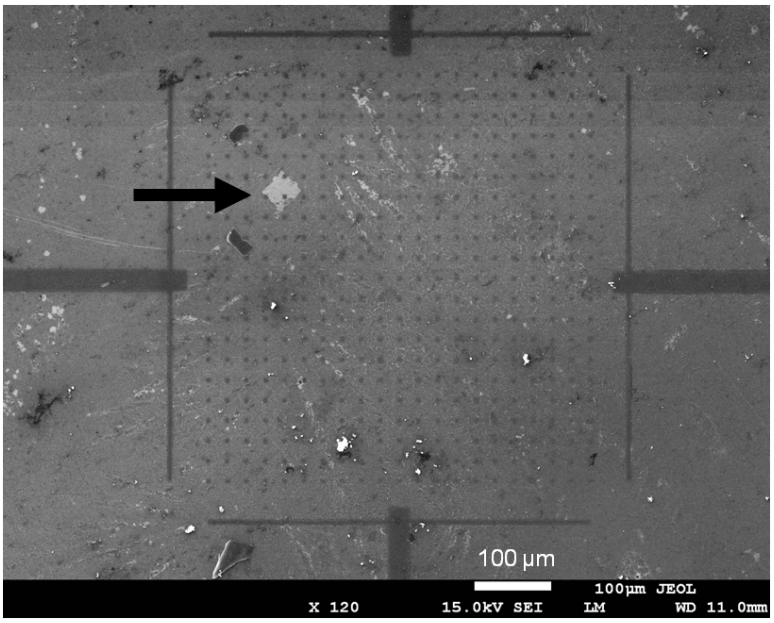

(a) The white scale bar is 100 μm.

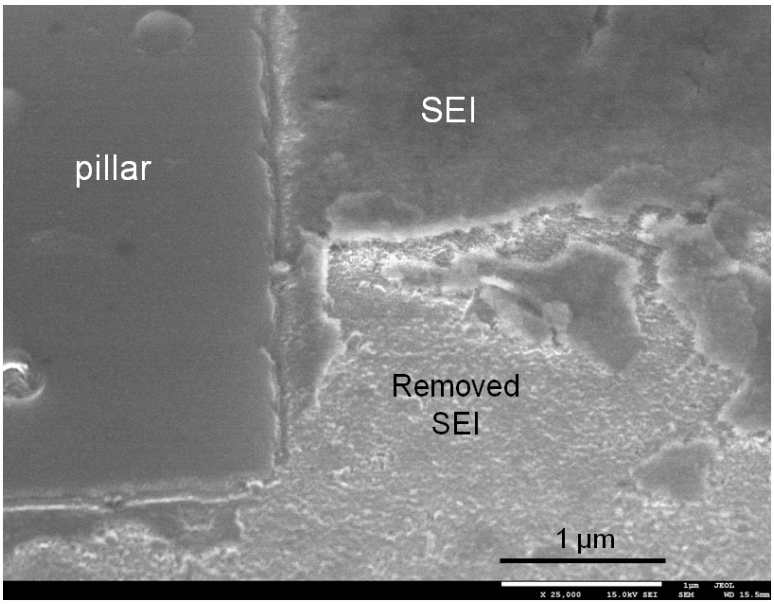

(b) The black scale bar is 1 μm.

Figure 5.6: Post-AFM SEM imaging. In (a), the small regularly spaced dots are the pattern of alumina pillars. The small light rectangle shows where the SEI has been removed by the AFM tip, indicated by the arrow in (a) and the label in (b).

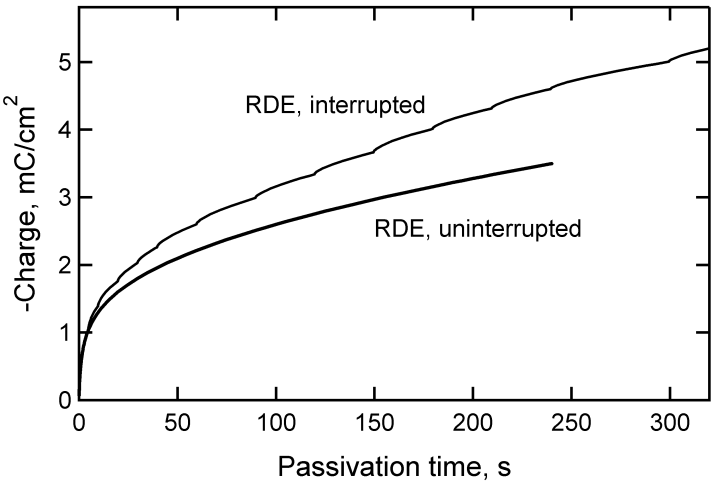

(a) Interrupted and uninterrupted polarization on RDE.

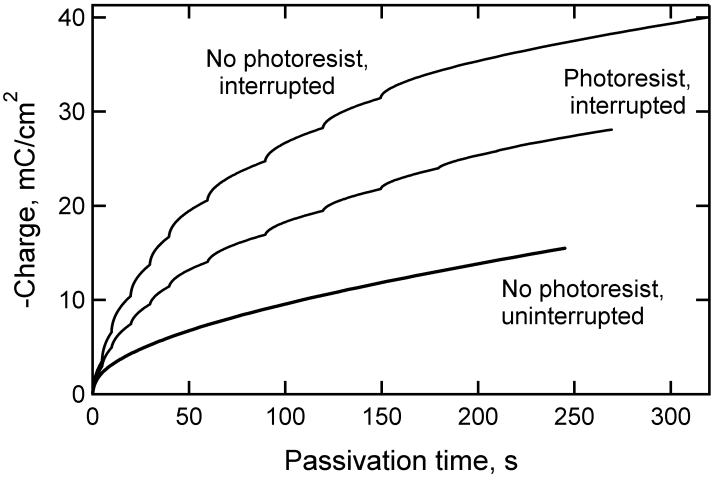

(b) Interrupted and uninterrupted polarization on planar glassy carbon.

Figure 5.7: Comparison of interrupted and uninterrupted formation at 0.6 V. Unlike the AFM experiment, both samples with and without the photoresist treatment showed consistent passivation for both interrupted and uninterrupted polarization at 0.6 V. The magnitude of charge passed was much greater on planar glassy carbon samples outside the AFM.

Part II

Modeling of overcharge reactions

Chapter 6

Two-dimensional modeling of lithium deposition

Deposition of metallic lithium during lithium-ion battery charging compromises cell safety by creating the possibility for dendritic growth and internal short-circuiting. The deposition reaction occurs upon overcharge, when lithium cannot insert into a saturated negative electrode and so plates out of the electrolyte onto the surface. To prevent overcharge, batteries are typically manufactured with an excess capacity of negative electrode. However, even with excess negative capacity, lithium can deposit if the potential drop between negative electrode and electrolyte reaches 0 volts versus lithium. This condition occurs in graphite electrodes upon fast charge, or at low temperature, when the overpotential required to drive current becomes greater than the equilibrium potential of graphite. By ending charge when the potential difference between positive and negative electrodes reaches a given cutoff potential, manufacturers attempt to prevent this mechanism of lithium deposition.

Arora et al used a one-dimensional macro-homogeneous cell model to describe lithium deposition in a system of Li_xC_6:$Li_yMn_2O_4$ [71]. One-dimensional macrohomogeneous models simultaneously solve for concentration and potential in the x-dimension of the electrolyte and in the r-dimension of electrode particles modeled as spherical. They have been used successfully to predict the overall behavior of many systems [72, 73, 74]. Macrohomogeneous models do not, however, capture the edge effects that are caused by the two- and three-dimensional geometry of physical cells. Edge effects have been experimentally observed to have significant influence on deposition and other side reactions during cell charging. Using micro-reference electrodes, Scott et al. measured the electrolyte potential in the center of the cell coil and at the edge of the coil, adjacent to the bare current collector, and observed a potential difference of up to 1 V [75, 76]. This potential variation allowed local potentials of 4.6 V versus lithium, resulting in oxidation of biphenyl, an overcharge protection additive. Experiments have also shown that even when average conditions do not favor lithium deposition, deposition preferentially occurs at the edges of electrodes, and that extending the negative electrode beyond the edge of the positive by approximately 1 mm can prevent deposition from occurring [77]. This work examines the effect of negative-electrode extension

on the current distribution during charging to explain why extending the negative electrode can prevent lithium deposition.

6.1 Model development

Two geometries were investigated in this work. Schematics of the systems modeled in COMSOL Multiphysics are shown in Figure 6.1, with a coordinate system labeled X and Y. Our model contains two subdomains, one representing the negative electrode, a film of graphite (Li_xC_6), and another representing the separator. In the first geometry, the positive electrode, cobalt oxide (Li_yCoO_2), is represented as an indentation in the separator. The half-length of the positive electrode is 2.5 cm, representing approximately half the length of a typical 18650 cell. The negative varies in length from 2.5 to 2.7 cm, giving an extension of 0 to 2 mm. The separator extends an additional 1 mm beyond the edge of the anode. The distances of 2.5 cm for the cell length and 1 mm for the separator extension are effectively infinite; simulations verified that decreasing either distance by a factor of two had no observable effect on the results. Our second geometry represents the positive electrode as a boundary along the top of the separator. Geometry I and II correspond physically to the cases of flooded and nonflooded cells, respectively. Although the second case is physically more realistic for battery manufacturers, the first permits us to examine edge effects in greater depth.

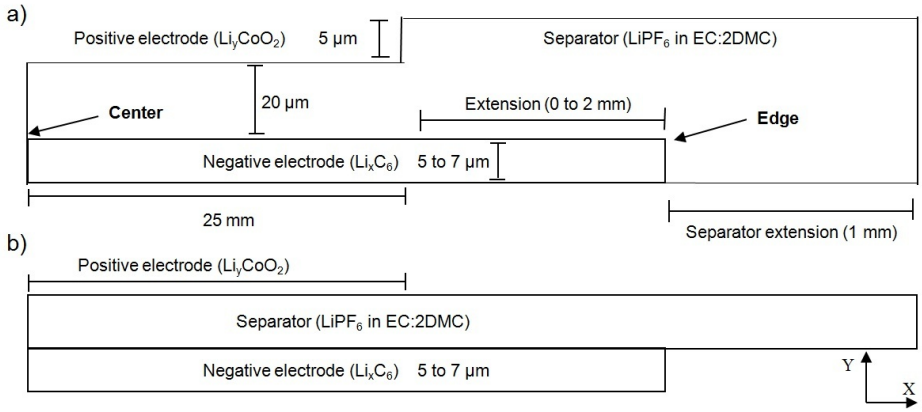

Figure 6.1: Model schematic (not to scale). The coordinate labels, X and Y, are distinct from the x and y used for stoichiometric ratios of lithium. In this work, 'length' refers to distance in Y and 'thickness' refers to distance in X.

The separator gap is 20 μm, and the base-case negative electrode and positive electrode thicknesses are 5.88 and 5 μm, based on the formula

$$\frac{C_-\rho_-w_-\Delta y}{C_+\rho_+w_+\Delta y} = 1.1 \tag{6.1}$$

where C_j is capacity, ρ_j is density, and w_j is thickness of material j. For the materials modeled, typical electrodes are 20 to 80 μm thick, and composed of particles approximately 10 μm in diameter. The thickness of the electrode (distance in coordinate Y) in our model thus corresponds to the radius of a particle in a porous-electrode model. We used a range of the stoichiometric coefficient in Li_yCoO_2, of 0.42 to 1.0 (Δy = 0.58) in order to keep the equilibrium potential of the positive electrode below 4.3 V, above which the delithiated electrode oxidizes solvents [78, 79, 80]. Δx in Li_xC_6 was 0.99. The equilibrium potential and range of cycling for each electrode are shown in Figure 6.2.

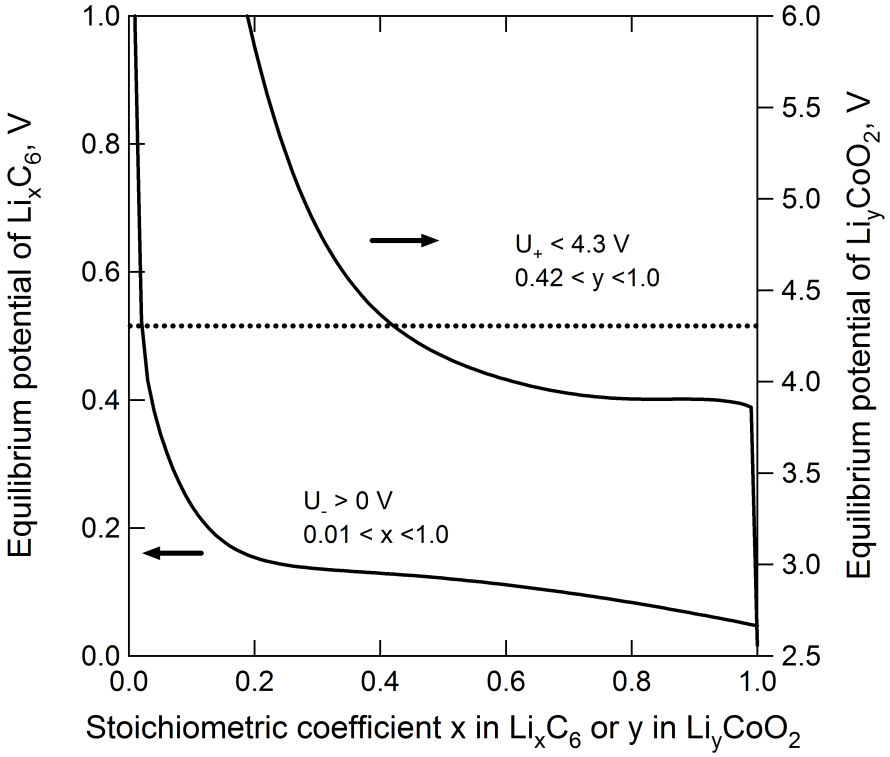

Figure 6.2: Equilibrium potentials of graphite, U_-, and oxide, U_+, as a function of stoichiometric coefficient, $c_s/c_{t,-}$. The range of cycling Δx and Δy were chosen in order to prevent U_+ ¿ 4.3 V. Fits for these curves are taken from references [71] and [81].

At low rates of charge and discharge, electrolyte concentration can be assumed constant. The liquid-phase potential Φ_2 then obeys Laplace's equation:

$$\nabla^2 \Phi_2 = 0 \tag{6.2}$$

and the current density is given by

$$i_2 = -\kappa_{\text{eff}} \nabla \Phi_2 \tag{6.3}$$

$$\kappa_{\text{eff}} = \kappa \epsilon^{1.5} \tag{6.4}$$

Because electrolyte concentration does not vary, κ_{eff} is a constant, adjusted for the separator porosity by the volume fraction ϵ raised to the Bruggeman factor 1.5. Inside the negative electrode, which is represented as a solid rectangular film, the lithium concentration is governed by the diffusion equation

$$\frac{\partial c_s}{\partial t} = D_1 \nabla \cdot (\nabla c_s) \tag{6.5}$$

where D_1 is the diffusivity of lithium ions in the electrode active material and is assumed constant. This equation is used only in the negative electrode because lithium diffusion in the positive electrode is not modeled. Literature values for the diffusion coefficients of both cobalt oxide and graphite vary widely, depending on state-of-charge and the method of measurement. Values reported range from 1×10^{-7} to 9×10^{-12} cm^2/s for Li_yCoO_2 [82, 83, 84, 85, 86, 81] and 1×10^{-7} to 2.27×10^{-13} cm^2/s for graphite [87, 88, 89, 90] In general, cited values for diffusivity of lithium in Li_yCoO_2 are higher than those for graphite, and because of SEI-forming reactions with the solvent, graphite particles are also generally larger than positive electrode particles. This means that the characteristic diffusion time, w^2/D_1, is shorter for the positive electrode. Accordingly, concentration is here assumed uniform with respect to position in the positive electrode. This means that for a galvanostatic charge, the positive-electrode lithium concentration can be parameterized as a function of time using Faraday's law:

$$c_{s,+} = c^0_{s,+} + \frac{I_{\text{set}}}{w_+ F} t \tag{6.6}$$

where $c^0_{s,+}$ is initial concentration, I_{set} is the charging rate in A/m^2 and w_+ is the thickness of the positive electrode.

The governing equations are not coupled in the subdomains themselves, but along the boundaries of both electrodes they are coupled by Faraday's law

$$n \cdot (-D_{1,-} \nabla c_s) = \frac{i_n}{F} \tag{6.7}$$

$$n \cdot (-\kappa \nabla \Phi_2) = i_n \tag{6.8}$$

n is the vector normal to the surface, and i_n is the transfer current with units of A/m^2. The expression for i_n depends on the kinetics of the system. At small currents, the Butler-Volmer expression for current density can be reduced to a linearized kinetic model, which we use here:

$$i_n = i_0 \frac{F}{RT} \left[(\Phi_1 - \Phi_2) - U(c_s) \right] \tag{6.9}$$

where Φ_1 is the potential of the solid phase, Φ_2 is the liquid-phase potential at the interface with respect to a lithium reference electrode, and U is the equilibrium potential of the graphite or oxide. Both U and i_0 depend on the concentration of lithium in the solid phase, as shown in Equations 6.10 to 6.12 and Figure 6.2.

$$i_0 = Fk(c_t - c_s)^{\alpha_{a,j}} (c_s)^{\alpha_{c,j}} (c)^{\alpha_{a,j}} \tag{6.10}$$

$$U_- = 0.7222 + 0.13868\left(\frac{c_{s,-}}{c_{t,-}}\right) + 0.28952\left(\frac{c_{s,-}}{c_{t,-}}\right)^{0.5} - 0.017189\left(\frac{c_{s,-}}{c_{t,-}}\right)^{-1} + 0.0019144\left(\frac{c_{s,-}}{c_{t,-}}\right)^{-1.5} + 0.28082\exp\left[15\left(0.06 - \left(\frac{c_{s,-}}{c_{t,-}}\right)\right)\right] - 0.79844\exp\left[0.44649\left(\left(\frac{c_{s,-}}{c_{t,-}}\right) - 0.92\right)\right] \tag{6.11}$$

$$U_+ = 3.8552 + 1.2473\left(\frac{c_{s,+}}{c_{t,+}}\right) - 11.152\left(1 - \left(\frac{c_{s,+}}{c_{t,+}}\right)\right)^2 + 42.8185\left(1 - \left(\frac{c_{s,+}}{c_{t,+}}\right)\right)^3 - 67.711\left(1 - \left(\frac{c_{s,+}}{c_{t,+}}\right)\right)^4 + 42.508\left(1 - \left(\frac{c_{s,+}}{c_{t,+}}\right)\right)^5 - 6.132\times10^{-4}\exp\left[7.657\left(\frac{c_{s,+}}{c_{t,+}}\right)^1 15\right] \tag{6.12}$$

c_t is the maximum concentration of lithium in the solid, determined by the theoretical capacity. Although the same kinetics apply at the positive and negative electrode interfaces, the sign of the current is reversed because anodic currents are defined to be positive.$\Phi_{1,+}$ is taken as the arbitrary zero point of potential, although only potential differences are used in this paper. The overall cell potential V_{cell} is given by the difference between the positive and negative electrodes

$$V_{\text{cell}} = \Phi_{1,+} - \Phi_{1,-} \tag{6.13}$$

Although a galvanostatic charge means that the total current applied to the electrode is constant with time, the current density along the electrode is nonuniform. This means that a constraint of the system is an integral boundary condition,

$$\oint i_n ds = I_{\text{set}} l_+ \tag{6.14}$$

l_+ is the length of the positive electrode (2.5 cm), and I_{set} is the average applied current density in A/m^2, determined by dividing the theoretical capacity of the positive electrode by the time of charge.

$$I_{\text{set}} = \frac{FC_+\rho_+ w_+ \Delta y}{t_{\text{charge}}} \tag{6.15}$$

I_{set} has units A/m^2, consistent with one-dimensional models. In a physical system or a three-dimensional model, the total current applied to a cell during charging has units of amps. The quantity $I_{\text{set}} l_+$, with units A/m, may be thought of as the total applied current for a two-dimensional system in which the neglected dimension is perpendicular to the plane of Fig. 6.1.

The arc length ds in Equation 6.14 applies to the entire electrode boundary, including the perpendicular edges in Geometry I. In order to solve for the nonuniform current distribution,

the model solves the governing equations and boundary conditions while varying E_{cell} until the surface integral of current density along the positive electrode matches the specified current. Because the solution of Laplace's equation in the separator guarantees that the divergence of flux is zero, Equation 6.14 is satisfied along the negative electrode surface as well.

The governing equations 6.2 and 6.5 were solved in COMSOL Multiphysics 3.4, with 6.7 to 6.12 implemented as boundary conditions. An "integration coupling variable" was used to solve 6.13 and 6.14 iteratively. The mesh was refined until the answers were independent of mesh size. Model parameters are presented in Table 6.1. The model described does not include either porous electrode or concentrated solution theory. We emphasize that this work is intended not as a practical guide to selecting electrode length, but rather as a theoretical exploration of how certain parameters, namely the geometry and capacity ratio, affect the problem of lithium deposition. Accordingly, we have neglected some physical phenomena in order to simplify the analysis and focus on those parameters of greatest interest. A summary of the assumptions in this model is given below.

1. Solid film electrodes
2. Linearized Butler-Volmer kinetics
3. Constant electrolyte concentration c_2
4. Irreversible capacity loss on first cycle neglected
5. Film resistances on electrodes neglected
6. Spatially uniform solid-phase potential $\Phi_{1,-}$ and $\Phi_{1,+}$
7. Isothermal

6.2 Model results and discussion

Current distributions

The current distribution in the system is determined by the balance of ohmic resistance from the electrolyte and kinetic resistance at the electrode interface, which is influenced by diffusion in the graphite. When solution conductivity is low or exchange current density is high, the system is ohmically limited, and the current distribution will approach the primary distribution. A primary current distribution is characterized by higher current densities at more accessible parts of the electrode [23]. For the case of evenly matched positive and negative electrodes, the edges are more accessible than the center. If, conversely, kinetics is slow or solution conductivity is high, the current density will approach uniformity along the electrode. Although the assumption of constant electrolyte concentration means that

Table 6.1: Cell properties and model parameters

Electrode Parameters	Li_xC_6	Li_yCoO_2
Reaction rate constant k, $m^{2.5}mol^{-0.5}s^{-1}$	4.9×10^{-11} [71]	2.8×10^{-10} [81]
Maximum concentration, mol m^{-3}	30.54	56.25
Range of cycling	0.99	0.58
Initial stoichiometric coefficient	0.01	1
Diffusion coefficient, m^2s^{-1}	5.5×10^{-14} [81]	–
Transfer coefficients α_a, α_c	0.5	0.5
Separator Parameters		
Volume fraction	0.55 [91]	
Solution conductivity, S m^{-1} (1.2 M $LiPF_6$ in EC:2 DMC)	1.3 [32]	
Electrolyte concentration, mol m^{-3}	1200	
Design-adjustable parameters		
Applied current, A m^{-2}	4.37 (1 C)	

conductivity is a constant in the system, both the equilibrium potential U_- and exchange current density i_0 change with lithium concentration in the electrode. The exchange current density depends on both solid lithium concentration and empty lattice sites in the electrode and thus reaches a maximum at $c_s = c_t/2$. U_- decreases rapidly for small values of x (see Figure 6.2), and thus the driving force for reaction, as well as the kinetic resistance, varies as the electrode is charged.

Current distributions affect the possibility of lithium deposition because of the generation of overpotential. As the negative electrode approaches saturation, the exchange current density decreases, and kinetic resistance increases. A larger (more negative) overpotential is then required to maintain the current. If the overpotential required becomes larger than the equilibrium potential, the electrode potential $\Phi_{1,-} - \Phi_2$ crosses 0 V and creates conditions favorable for deposition. The other mechanism of deposition is overcharge, when the negative electrode is charged to saturation ($c_{s,-} > c_{t,-}$). When either of these conditions is reached in a real system, the lithium deposition reaction will consume part of the applied current. However, because we are interested not in determining the rate of deposition, but rather in the times and positions at which deposition occurs, it is sufficient for us to know the conditions under which the electrode reaches either saturation or conditions that thermodynamically favor deposition, $\Phi_{1,-} - \Phi_2 < 0$.

Matched electrodes

Figure 6.3 shows qualitatively the current distributions for each of the two geometries at 25 minutes. In these plots, the gradient of color in the negative electrode represents the normalized solid-phase lithium concentration, and the lines represent the direction of current flow. Lines of constant liquid-phase potential Φ_2 run perpendicular to current flow but are

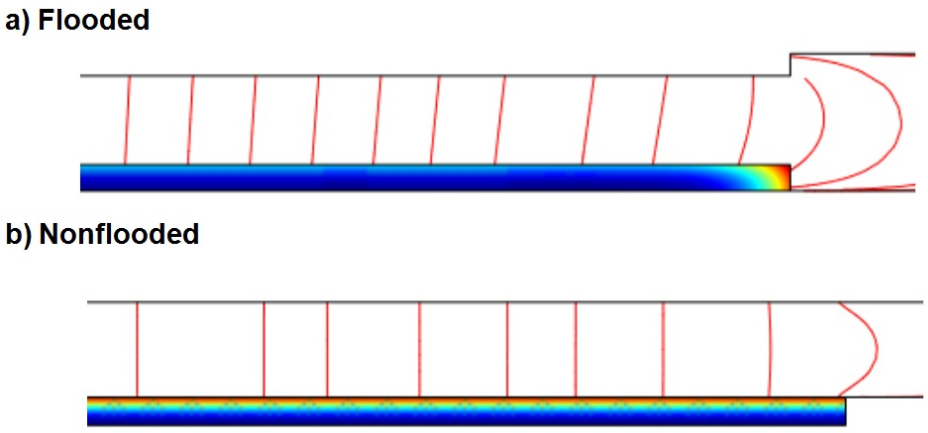

Figure 6.3: Current lines and normalized lithium concentration distributions in flooded (Geometry I) and nonflooded (Geometry II) cells. The gradient of color shows normalized lithium concentration (c_s/c_t) increasing from approximately 0.36 at the bottom to 0.44 at the top of the electrode for both cells. In the flooded cell, the greater accessibility of the edge region allows normalized concentration there to reach 0.63 when in the center c_s/c_t equals only 0.44. Current may flow out into the separator for either system, but the magnitude of this effect is much smaller for the second geometry.

not pictured. In the first geometry modeled, the case of a flooded cell, current can flow out into the separator and around to the end of the electrode; thus, lithium concentration is higher in the edge region. Despite the fact that the ends of the positive and negative electrodes in Geometry II do not contact the electrolyte, current still has the ability to flow out into the separator and create a nonuniform current distribution. However, because the ends of the electrode are insulated, the amount of current flowing out into the separator is too small to affect appreciably the concentration. Because the current distribution in the second geometry is essentially uniform, we focus on the more interesting behavior exhibited by the first system.

In Geometry I, the current flowing to the edge region of the negative electrode tends to be higher than that nearer the center because it is near the edge of the electrode and because there is also a corner. However, the presence of the extra electrode surface beyond the corner (the surface perpendicular to the positive electrode) causes the local current density i_n to be lower in the edge region. To express these opposing views, one can plot the current distribution in two ways: the local current density i_n against the arc length s, and the effective current density i_{eff} flowing to the top surface, obtained by totaling the insertion through a thickness, expressed as

$$i_{\text{eff}} = F \int_0^{w_-} \frac{\partial c_s(\chi, \psi)}{\partial t} d\psi \tag{6.16}$$

The extra current flowing through the end is included in the current flow to the edge region, but its penetration toward the center of the electrode is limited by the internal diffusion process. This is illustrated in Figure 6.4, which shows the current distribution expressed in these two ways at early, middle, and late times during the charge. There are pairs of curves at 0, 25, and 54 minutes. The areas under the curves are the same, but while i_n includes the entire electrode surface, i_{eff} extends only out to the edge. The average value of the curve is equal to one for i_{eff}, but slightly less than one for i_n because of the additional surface area along the end of the electrode. Figure 6.4 depicts only the very small region of the electrode that is influenced by edge effects. Because this region is such a small portion of the entire electrode, currents lower and higher than the average value can be observed without perceptibly affecting the value in the center.

Initially, there is no concentration polarization, although there is surface overpotential. i_n has a maximum at the edge, but the maximum is too small to be seen on the chart because at zero time, the exchange current density is very small, and the system approaches a kinetically-limited uniform distribution. Calculating the current the second way (i_{eff}) includes the current along the perpendicular edge and thus exhibits a much stronger maximum. i_{eff} is numerically very noisy at short time because, then, the penetration distances in the electrode are very short and concentration is very low. These smaller numbers are more susceptible to error because even a small change in concentration is large in comparison to the concentration itself, and thus numeric noise is amplified. Refining the mesh and reducing the time step was effective at reducing the error at short time, but in order to eliminate noise completely, an infinitely small mesh would be required. The results at long time are less sensitive to error because, at long time, changes in concentration are less abrupt and the solution is more stable. Refining the mesh to reduce short-time error did not affect the long-time model results.

As time progresses, the higher utilization in the edge region creates a concentration overpotential, which shifts the maximum in i_{eff} away from the edge region. This is shown in the dashed line of Figure 6.4 at $t = 25$ minutes. The maximum is relatively small, only about 10%, showing that the current distribution is substantially uniform. The concentration in the edge region remains higher, but the rate of concentration increase is the same at all parts of the electrode. Similar behavior has been observed in the modeling of lead-acid batteries [92].

Towards the end of charge, the edge region has become nearly saturated. Figure 6.5 shows the normalized concentration at both the edge and the center of the electrode versus time. The higher concentration in the edge region means that the equilibrium potential falls faster and the exchange current density passes through the maximum earlier at the edge than in the center. When this occurs, the insertion reaction at the edge becomes less favorable, and current density falls, as shown by the dotted lines in Figure 6.4 ($t = 54$ minutes). The two factors of equilibrium potential and exchange current density also force a greater local overpotential; thus, the edge reaches conditions favorable for deposition several seconds before the center of the electrode. Because of overpotential, conditions which favor deposition occur at approximately 54.5 minutes, while the cell reaches the cutoff potential

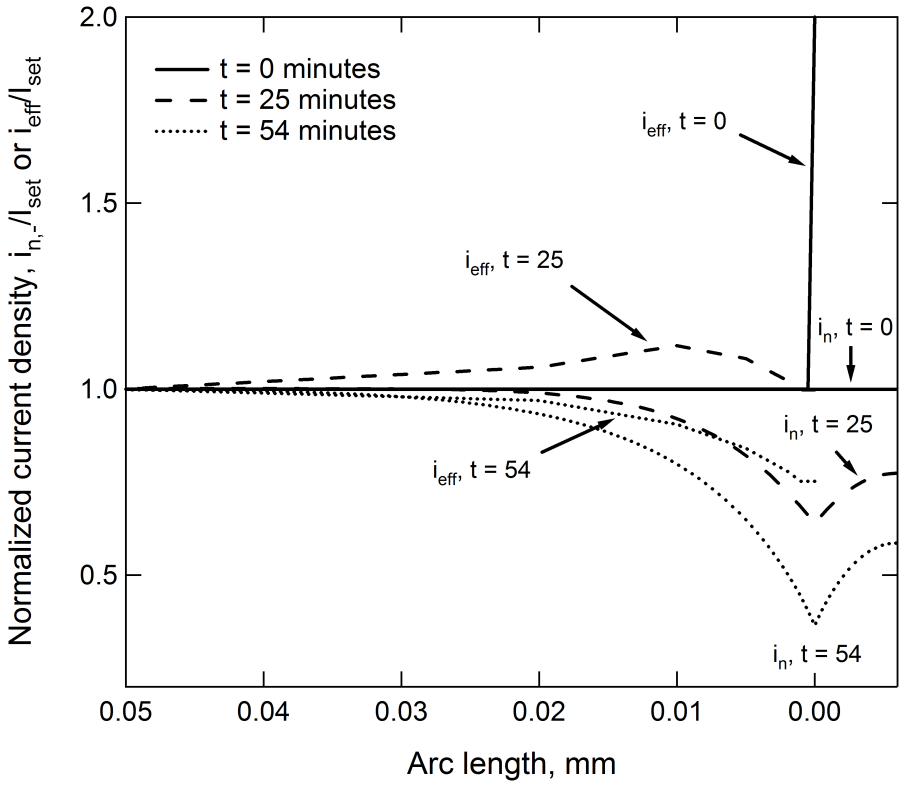

Figure 6.4: A plot of normalized current i_n and i_{eff} vs. arc length at different times shows how the current distribution is affected by the changing concentration in the negative electrode. In the figure, an arc length of 0 corresponds to the edge of the negative electrode, and the center of the electrode is off the scale at an arc length of 25 mm. Lines which extend past an arc length of zero represent i_n, and lines which end at zero represent i_{eff}. At short time (t=0 minutes), i_n is nearly uniform along the entire surface because it is kinetically limited, and i_{eff} has a large maximum at the edge. At intermediate time (t = 25 minutes), concentration overpotentials in the solid phase have caused the current distribution to even out, so that i_{eff} is somewhat uniform. At long time (t = 54 minutes) the edge region has become saturated and both current density i_n and effective current density i_{eff} fall at the edge. Numeric error is high at short time; the reasons are discussed in the text.

of 4.2 V at 55.0 minutes (Figure 6.6).

Because the positive electrode has a uniform lithium concentration, the edge and center of the positive electrode experience identical kinetic resistances and equilibrium potentials. Edge effects in the positive are therefore caused only by the potential distribution in the solution phase. In Figure 6.8, the current density plotted versus arc length along the positive electrode at short, intermediate, and long time shows that, compared to the negative electrode, current is fairly uniform; the slight increase at the edge is because of the higher i_{eff} at the edge region of the negative electrode. As time increases, the increased kinetic

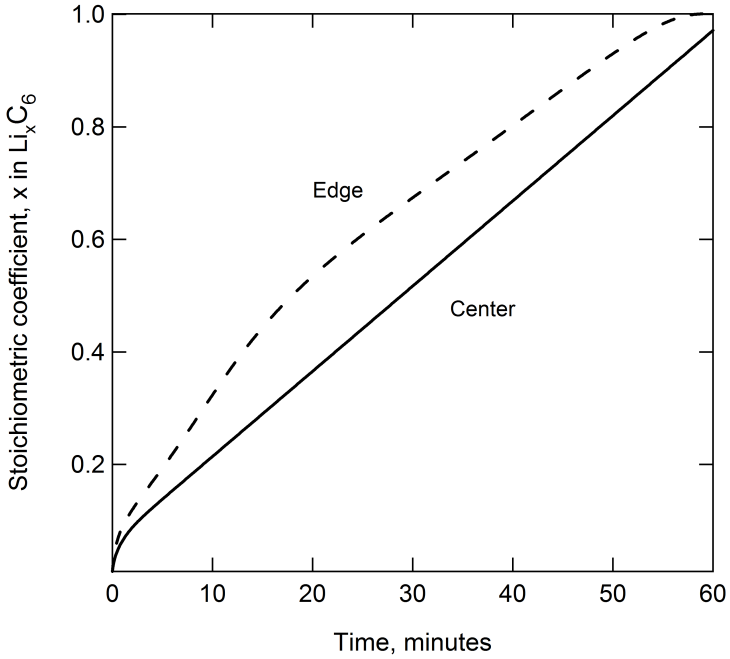

Figure 6.5: Normalized concentration vs. time at different positions along the negative electrode in a flooded cell shows that in the center, a near-constant concentration increase means a near-constant current equal to the average charge rate. At the edge, concentration rises faster at short time, and then slows as the electrode becomes saturated. The higher concentration at the edge creates conditions favorable for deposition at an earlier time than in the center. The locations of the labels Edge and Center are shown in Figure 6.1. For the case of nonflooded cells, the concentration vs. time curve at both the center and edge collapse onto the curve marked Center.

resistance and lower driving force at the edge of the negative draw less current at the edge of the positive. Again, the average values of i_n and i_{eff} do not change, but the greater length of the electrode can absorb the current variation in the edge region without significant changes in the center.

Effect of negative-electrode extension

Extension with constant thicknesses

Extending the negative electrode beyond the edge of the positive has two effects. First, the capacity ratio of negative to positive is increased. Because the applied current I_{set} is determined by the theoretical capacity of the positive electrode, the negative electrode sees a lower effective charge rate under the same conditions as before. The current density is also reduced because the area for charge transfer is larger. Smaller current densities will require

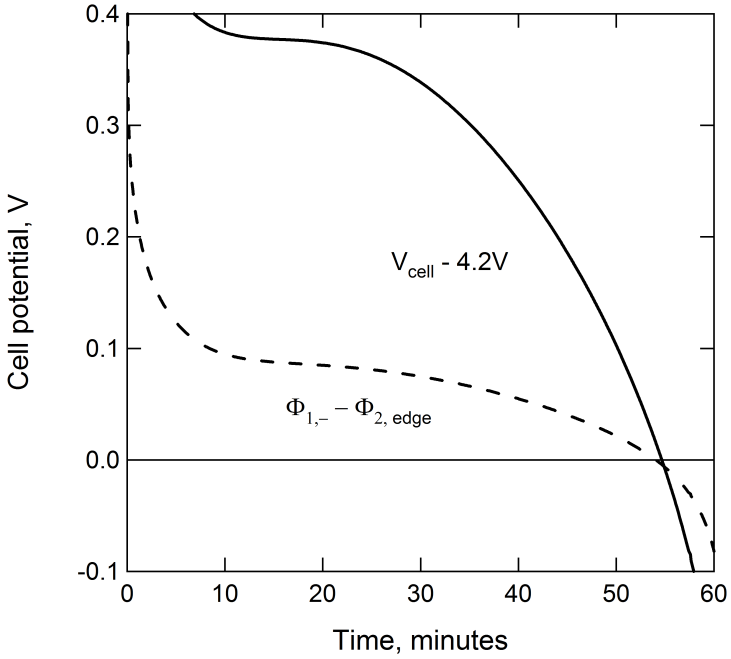

Figure 6.6: Potential drop at edge of electrode vs. time and cell voltage vs. time shows that, for a 1C charging rate, lithium deposition conditions are reached at approximately 54 minutes but the cell does not reach the cutoff potential of 4.2 V until 54.5 minutes. Deposition occurs, despite capacity balancing, because of overpotential in the negative electrode.

lower overpotentials, which means that $\Phi_{1,-}$ the potential of the negative electrode, falls more slowly. This delays the times at which the potential reaches that of deposition and cutoff. Second, the excess capacity is provided where mass transfer is highest. The electrode edge does not become saturated as quickly, and the time at which deposition occurs is delayed so that the cutoff potential is reached first. The times for each are shown in Figure 6.9. For electrodes where the negative is initially in excess by 10%, an extension of about 0.4 mm is sufficient to prevent the onset of lithium deposition until after the cutoff potential of 4.2 V is reached. As the electrode is extended further, the effect on the time to reach both cutoff and deposition is reduced because, as the added capacity moves farther from the positive electrode, current must overcome a greater ohmic resistance to make use of the added capacity. Figure 6.9 also shows that extending the negative electrode has a similar effect for both the cases of flooded and nonflooded cells. Although the nonflooded cell exhibits a uniform current distribution when the electrode are matched, extending the electrode still adds both capacity and surface area, reducing overpotential and delaying deposition.

Extending the negative electrode also has the effect of increasing the current density at the edge of the positive electrode, which lowers the time at which the positive electrode reaches a potential at which detrimental side reactions become thermodynamically favorable. Figure 6.7a shows the current density i_n versus arc length at the edge of the negative electrode

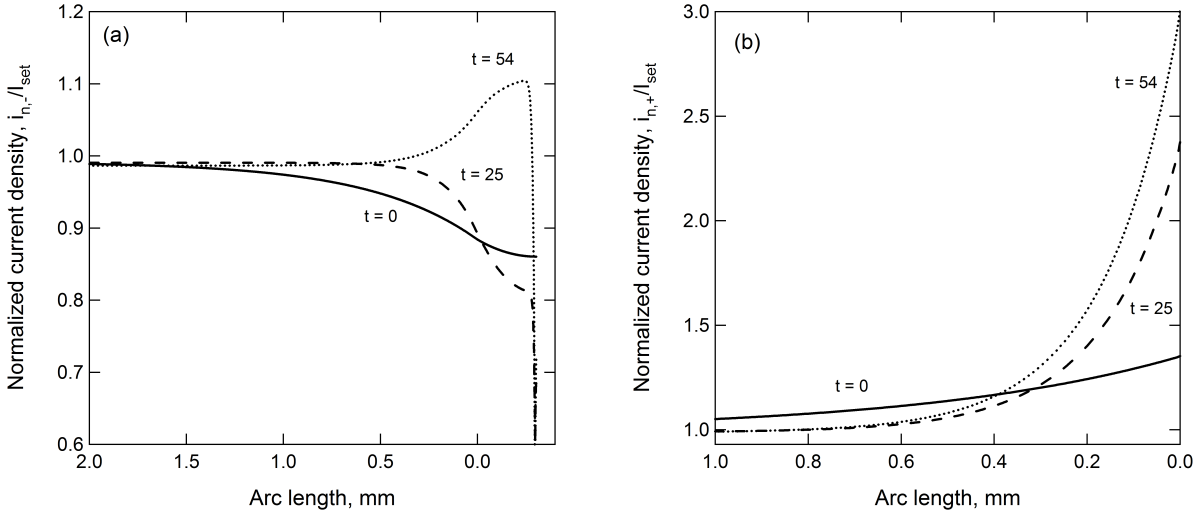

Figure 6.7: Normalized current density versus arc length along the negative (a) and positive (b) electrodes for mismatched electrode lengths (here, the extension is 0.3 mm). In the figure, an arc length of 0 corresponds to the edge of the positive electrode, which does not align with the edge of the negative. Current density is nearly uniform in the center but decreases towards the edge of the negative electrode at short time. At long time, concentration overpotentials cause current to shift to the edge and extension of the negative electrode. This draws a higher current from the edge of the positive electrode. Because the region affected by the edge is such a small percentage of the entire electrode surface, the current may be two or three times the average value without significantly affecting the current density in the center. The above plots are for the case of a flooded cell (Geometry I), but the behavior for both systems is qualitatively the same.

for the case of a 0.3 mm negative-electrode extension, and Figure 6.7b shows i_n versus arc length at the edge of the positive electrode in the same simulation. In these plots, an arc length of 0 corresponds to the end of the positive electrode. In the negative electrode, the extension is farther from the positive electrode and thus less accessible. Thus, at t = 0, the current density is lower in the extension. The added material of the extension increases the surface area available for reaction and causes the current density in a region extending approximately 2.5 mm from the edge (arc length = -0.3) to decrease. As in the case of matched electrodes, i_n reaches a nearly constant value at the center of the electrode, but, because I_{set} is determined by the capacity of the positive electrode, the normalized current density is less than unity at the center. As time increases, the center of the electrode saturates, and the maximum in current density shifts to the right. The higher current at the edge of the negative draws a higher current density from the edge of the positive electrode. Because the region affected by the edge is such a small percentage of the entire electrode surface, the current may be two or three times the average value without significantly affecting the current distribution in the center. This higher current

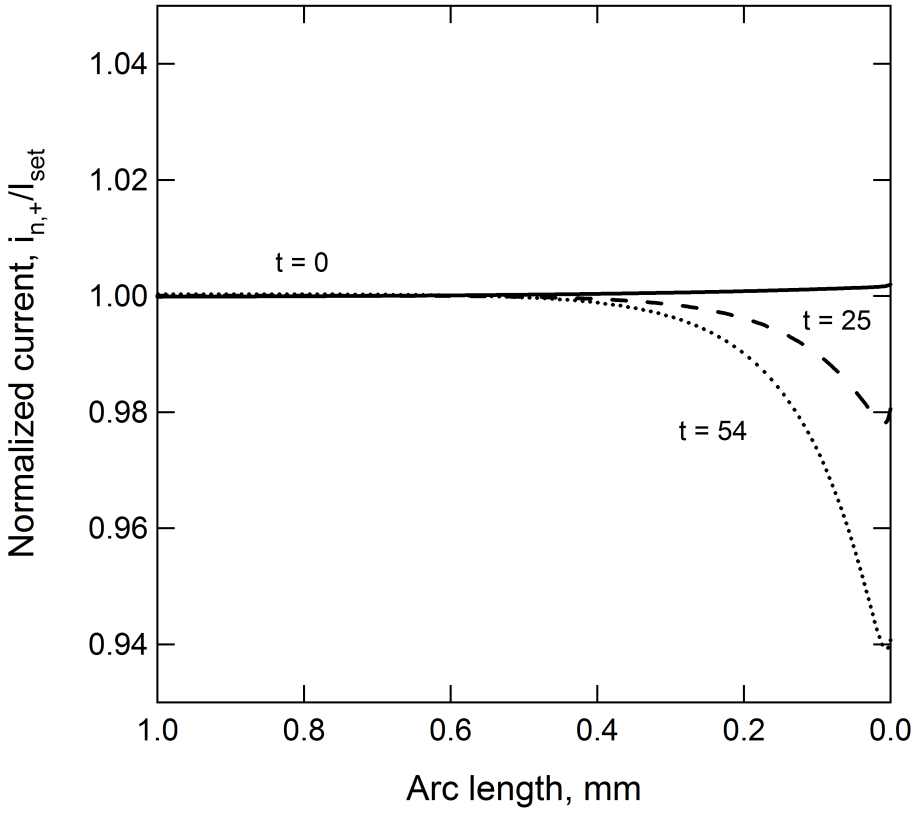

Figure 6.8: Normalized current versus arc length along the positive electrode for matched electrode lengths. In the figure, an arc length of 0 corresponds to the edge of the positive electrode, which is aligned with the negative. The center of the electrode is off the scale at 25 mm. Variation in current density is much smaller because concentration overpotentials do not occur in the positive electrode. At long time, the current density at the edge decreases because a lower driving force and higher resistance at the edge of the negative electrode draw less current.

density generates a greater potential drop at the surface of the positive electrode ($\Phi_{1,+} - \Phi_2$), crossing 4.3 V sooner as the extension increases. However, as Figure 6.7 shows, even at an extension of 2 mm, either deposition or cell cutoff is reached first, and side reactions at the positive are not of practical concern.

Comparison between thicker and longer electrodes

We can demonstrate that cell geometry has an effect on the current distribution independent of capacity ratio by keeping the lengths of the positive and negative electrodes equal while varying negative electrode thickness in order to obtain similar capacity ratios. These results are shown in Figure 6.10 and compared with the values from longer electrodes, as

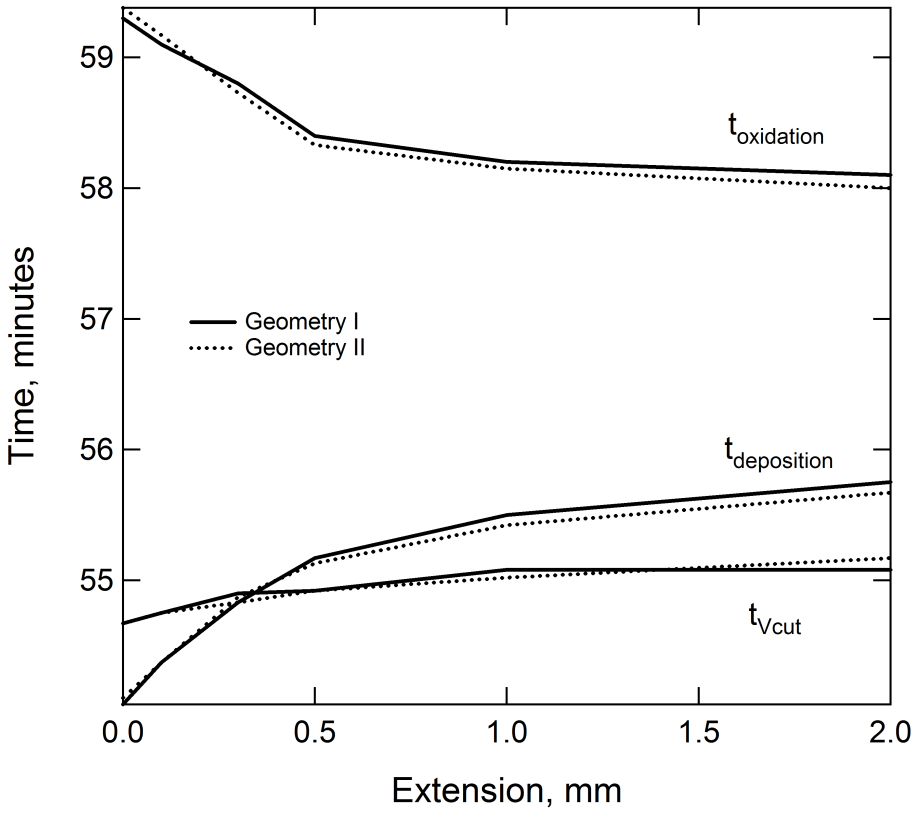

Figure 6.9: Time to reach conditions under which lithium deposits ($\Phi_{1,-} - \Phi_2 < 0$), $t_{\text{deposition}}$, time to reach cutoff potential (4.2 V), t_{Vcut}, and time to reach conditions under which solvents oxidize at the positive electrode ($\Phi_{1,+} - \Phi_2 > 4.3$), $t_{\text{oxidation}}$, versus extension of negative electrode for both flooded cells (solid lines) and nonflooded cells (dotted lines). Extending the negative electrode to approximately 0.4 mm beyond the edge of the positive delays the onset of lithium deposition until after the cutoff potential is reached.

in Figure 6.9. At smaller capacity ratios, the time to reach the cutoff potential increases by approximately the same amount regardless of where capacity is added. This is because the cutoff potential, E_{cell}, is the potential difference needed to drive the total current, $I_{\text{set}} l_+$, and, because both of these are based on the positive electrode, they do not change with the geometry. The time to reach deposition, however, increases more at smaller capacity ratios when the electrode is made longer and not thicker. Lithium deposition depends on the local electrolyte potential, and thus adding capacity and area at the edge is more effective at preventing deposition than making the electrode thicker. At higher capacity ratios, current must overcome a greater ohmic resistance to make use of the added capacity, and making the electrode thicker instead of longer is more effective at delaying deposition.

The intersection of curves (a) and (b) gives the capacity ratio at which the cutoff potential

will be reached before deposition occurs for the case of a longer electrode. Similarly, the intersection of (c) and (d) gives the capacity ratio if the electrode is made thicker but not longer. These capacity ratios may be related back to either the critical length or critical thickness required to prevent deposition. Finally, the intersection of (a) and (c) gives the capacity ratio at which extending the electrode prevents deposition less effectively than making it thicker. In other words, the electrode may be extended only so far before the added capacity becomes practically unusable. The intersection of (a) and (c) gives the critical electrode length, beyond which we reach a region of diminishing returns and it would be better to make the electrode thicker, instead of longer, regardless of cutoff potential.

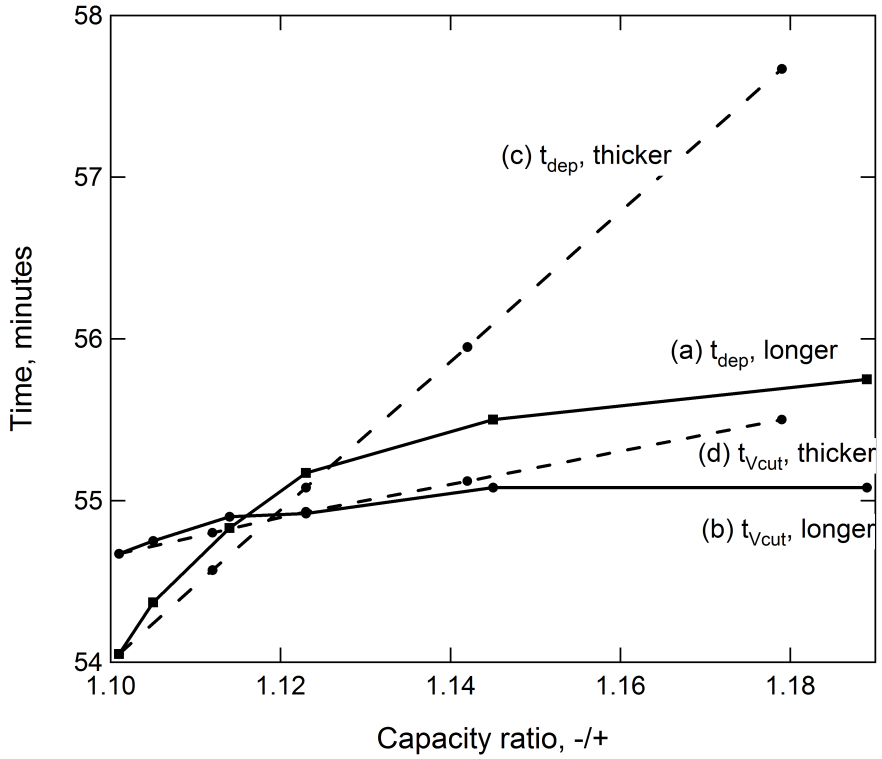

Figure 6.10: a) time to reach conditions under which lithium deposits ($\Phi_{1,-} - \Phi_2 < 0$), t_{dep}, b) time to reach cutoff potential (4.2 V), t_{Vcut}, under the conditions of extending the negative electrode, and c) time to reach deposition and d) cutoff potential when making it thicker, as functions of capacity ratio. Time to reach the cutoff potential is little affected by geometry, but extending the electrode is more effective at preventing deposition.

Extension with constant capacity ratio

To see if manipulating geometry alone can prevent lithium deposition, we extend the length and reduce the thickness of the negative electrode while maintaining a constant negative

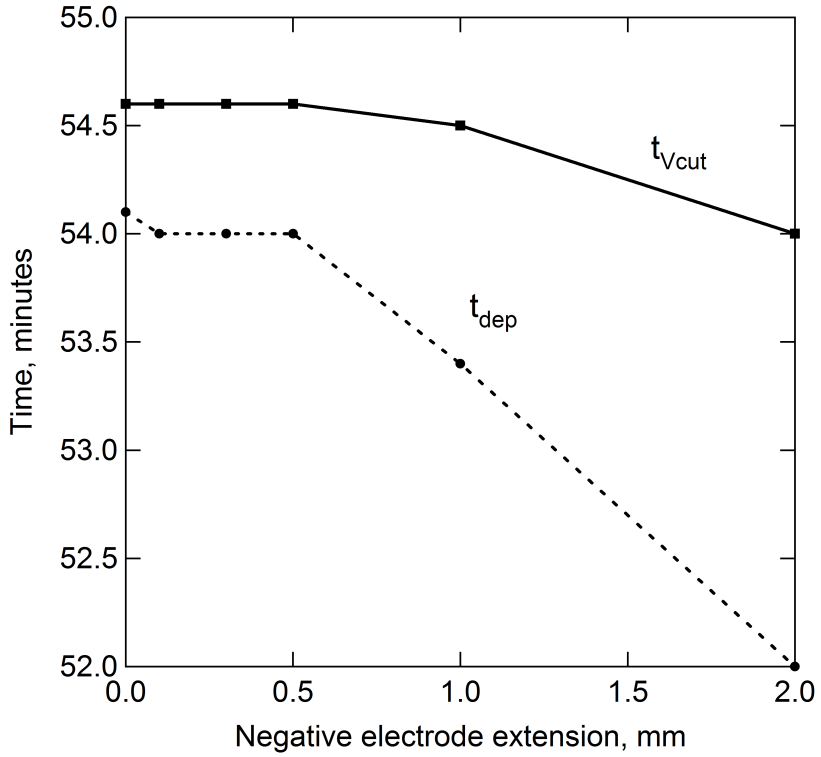

Figure 6.11: Plot of time to reach conditions under which lithium deposits, t_{dep}, and time to reach cutoff potential, t_{Vcut}, when capacity ratio is conserved by extending the negative electrode and making it thinner. Small changes to geometry have little effect on deposition, but further extension increases the average charge rate so that the cell both deposits lithium and reaches cutoff sooner.

electrode excess of 10%. These results are shown in Figure 6.11. The model shows that in comparison to the case of simply adding additional capacity, adjusting the geometry by a small amount has very little effect on postponing both the onset of deposition at the edge of the electrode and the time at which the cell reaches the cutoff potential, and thus lithium still deposits. At further extension, the electrode is stretched even longer and thinner, and the capacity ratio in the center of the electrode decreases. This means that the entire electrode sees a higher effective charge rate, and plates lithium sooner.

Parameter Exploration

Effect of rate constants

We want to know how the various input parameters of our model affect the shape of the curves in Figures 6.9 and 6.10. We first vary the negative reaction rate constant, k_{-}, both increasing and decreasing by approximately a factor of two, and plotting the time to reach deposition

and cutoff in Figure 6.12 as a function of electrode extension. Figure 6.12 shows that, with a low value of k_-, overpotentials are high and intercalation is not favorable compared to deposition. Also, even a small change in the rate constant has an extreme effect on the behavior of the cell. For reaction kinetics that are twice as fast as the baseline value, the cutoff potential is always reached before deposition occurs, and for kinetics that are half as fast, no amount of added length will be able to prevent deposition from occurring before the cutoff potential is reached. These results show that the model is extremely sensitive to the parameter k_-, and that for many values of k_-, kinetic effects will dominate any changes to electrode geometry. Of note also is that this model does not treat the kinetics of the deposition reaction. If the rate constant for deposition were lowered, deposition would still occur at $(\Phi_{1,-} - \Phi_2 < 0)$, but rates would be reduced.

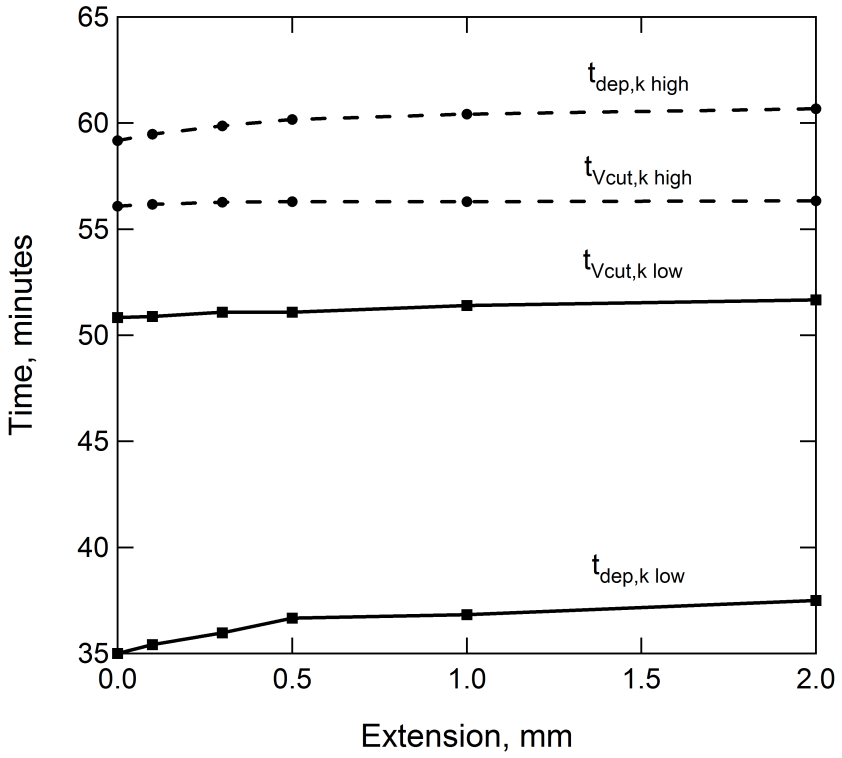

Figure 6.12: Time to reach conditions under which lithium deposits, t_{dep}, and time to reach cutoff potential, t_{Vcut}, for values of the reaction rate constant $k_- = 2 \times 10^{-11}$ and $10 \times 10^{-11}\text{m}^{2.5}\text{mol}^{-0.5}\text{s}^{-1}$ (the baseline value is $4.910 \times 10^{-11}\text{m}^{2.5}\text{mol}^{-0.5}\text{s}^{-1}$). A factor of five increase brings the model from a regime where no amount of electrode extension will prevent deposition to a regime where no deposition will ever occur.

Effect of charging rate

Charging a battery in a shorter time requires a larger current density, which in turn requires a larger overpotential. In our simulations, we use a C-rate, which corresponds to charging the cell in one hour. This is higher than what lithium ion batteries are typically charged at, so we increase and decrease the applied current by a factor of two in order to determine how sensitive the model is to this parameter. Like Figure 6.12, Figure 6.13 shows the time to reach lithium plating and the time to reach cutoff potential versus electrode extension in a flooded cell. The solid lines are for a charging rate of 2C, and the dashed for a rate of 0.5C. For comparison, the times are normalized by the C-rate so that 60 minutes correspond to 120 for a 0.5C charge and 30 for a 2C. Figure 6.13 shows that for a charge rate of 0.5C, cutoff will be reached before deposition conditions regardless of extension length, and thus no extension is necessary, but that for a rate of 2C, no amount of extension will be able to prevent deposition. While this result may not be quantitatively helpful for battery manufacturers, it agrees qualitatively with the empirical observation that deposition is a greater problem at higher rates. Additionally, the magnitude of edge effects is greater at higher rates as well. At a rate of 1C, the difference between liquid-phase potential at the edge and center is approximately 0.3 mV, which causes lithium to deposit several seconds earlier at the edge than the center. At a rate of 2C, the difference is approximately 0.5 mV, and at 0.5C, less than 0.1 mV.

Effect of electrolyte conductivity

We next determine the effect of electrolyte conductivity on the shapes of the curves in Figures 6.9 and 6.10. The time to reach either deposition or cutoff potential is plotted against electrode extension in Figure 6.14 for different values of κ_{eff}. Figure 6.14a shows the time to reach deposition and cutoff potential for longer electrodes as a function of electrode extension. Figure 6.14b shows the time to reach deposition for longer electrodes (solid lines) and thicker electrodes (dashed lines). The figures show that, as the conductivity increases, so does the relative gain of extending the electrode. When conductivity is low, the system has a nonuniform current distribution, and current prefers to flow directly across the electrode gap. When conductivity increases, the current distribution becomes more uniform, and the ohmic resistance to the electrode extension decreases, so that current is more likely to flow to the added capacity at the edge. Varying the conductivity has a much weaker effect on the time to reach cutoff potential, as shown by the dashed lines of Figure 6.14a, and on the time to reach deposition when the electrode is made thicker instead of longer, as shown by the dashed lines in Fig. 6.14b. A factor of four increase in the conductivity adds only ten seconds to the time to reach deposition for thicker electrodes.

Effect of separator distance

Finally, we look at the effect of the interelectrode gap. As Figure 6.15 shows, increasing the interelectrode distance from 20 to 50 μm has almost no effect on either the time to reach the

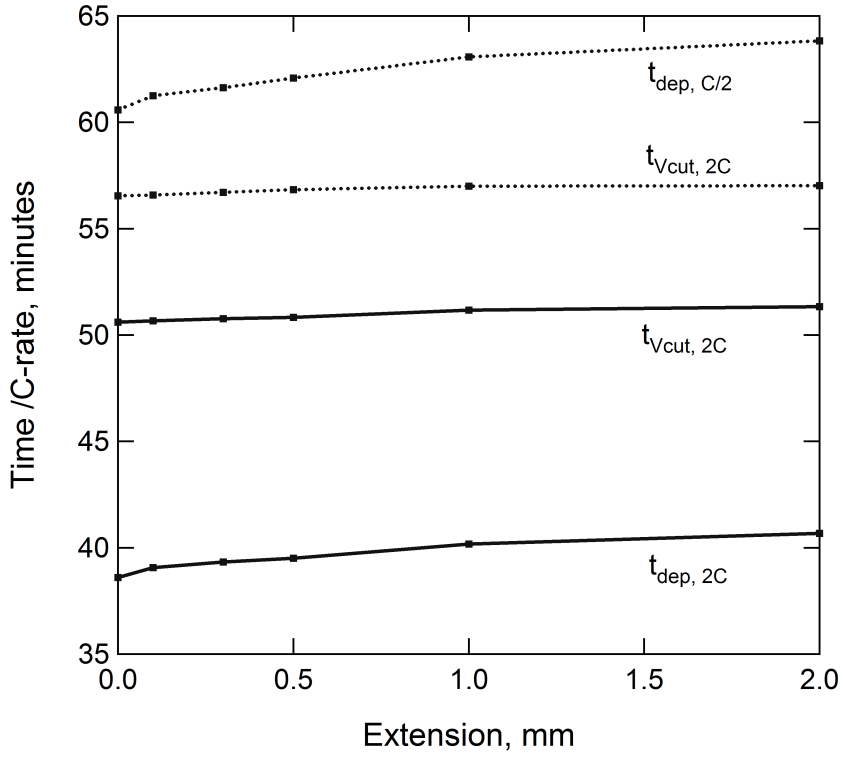

Figure 6.13: Normalized time to reach conditions under which lithium deposits, t_{dep}, and time to reach cutoff potential (4.2 V), t_{Vcut}, for a charging rate of 0.5C (dashed lines) and a charging rate of 2C (solid lines). At 0.5C, the cutoff potential is reached before the cell reaches deposition conditions without any electrode extension, but at 2C deposition occurs regardless of how much the electrode is extended.

cutoff potential or the results when the electrode is made thicker, not longer. The time to reach deposition, though, is much longer for a larger gap distance. Although we should expect that increasing the distance leads to a more nonuniform current distribution, the geometry of the system suggests that as the distance between electrodes increases, the difference between flowing directly across the gap and out to the side is no longer as significant. Extending the electrode is then more effective at preventing deposition when the electrodes are spaced farther apart than when they are closer together.

6.3 Conclusions

COMSOL Multiphysics was used to solve the two-dimensional potential and current distribution during galvanostatic charge of lithium-ion batteries, coupled with solid-state lithium diffusion in the negative electrode. The length of the negative electrode relative to the positive varied from 0 to 2 mm. In the case of evenly aligned positive and negative electrodes,

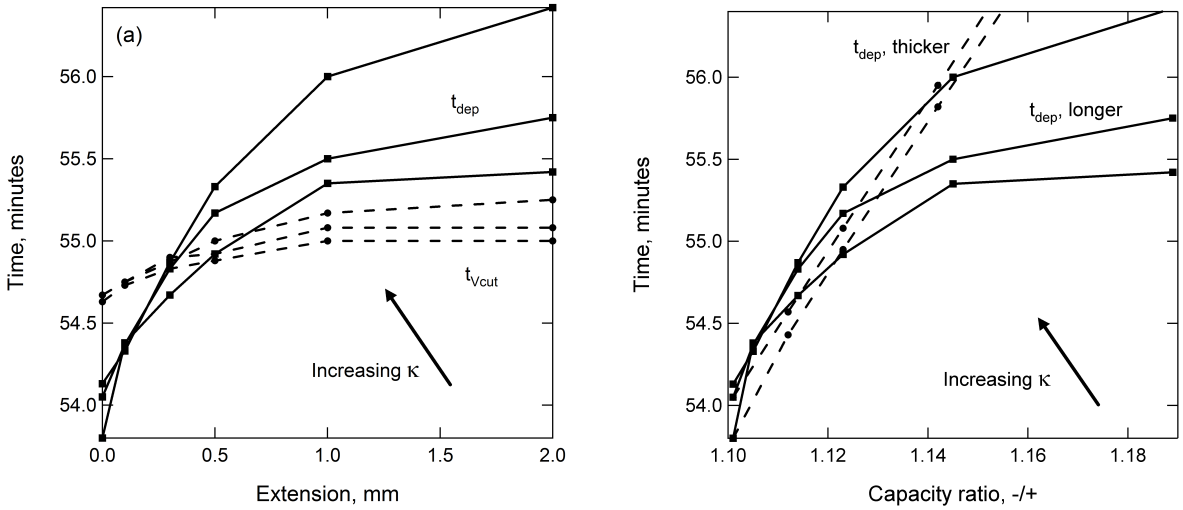

Figure 6.14: a) Time to reach deposition (solid lines) and cutoff potential (dashed lines) as the electrode is extended, for $\kappa_{\text{eff}} = 0.33$, 0.533 (baseline), and 1.3 S/m. b) time to reach deposition as electrode is either extended (solid lines) or thickened (dashed lines), for the same values of κ_{eff}. As the conductivity increases, there is less ohmic resistance through the separator to the extension and thus extending the electrode becomes more effective at preventing deposition. Neither the time to reach the cutoff potential nor the time to reach deposition is strongly affected when the electrode is made thicker.

the greater accessibility of the edge of the negative electrode causes the graphite there to approach solid-phase saturation sooner and requires a higher local polarization in order to maintain current flow. This polarization generates a local electrolyte potential that permits lithium deposition before the entire cell reaches the cutoff potential and stops charging. Although increasing the thickness of the negative electrode prevents deposition, extending the negative electrode is more effective in preventing the deposition that occurs preferentially at the edge. When the negative electrode is extended, current that previously flowed to the edge is distributed through the electrode extension. The additional capacity means a slower approach to solid-phase saturation and a longer time to reach conditions which favor lithium deposition. This effect holds for both flooded and nonflooded cells.

We varied four parameters: the negative reaction rate constant, the rate of charging, the electrolyte conductivity, and the distance between electrodes. The model is extremely sensitive to the rate constant and the charge rate; decreasing the rate constant or increasing the rate of charge by a factor of two can bring the model into a regime where neither increased thickness nor increased length can prevent deposition, while increasing the rate constant or decreasing the rate of charge by a factor of two shows that deposition will never occur. A higher conductivity means that extending the electrode is more effective at preventing deposition, because the resistance through the separator to the extension is reduced. A greater distance between electrodes also favors extending the electrode because the added

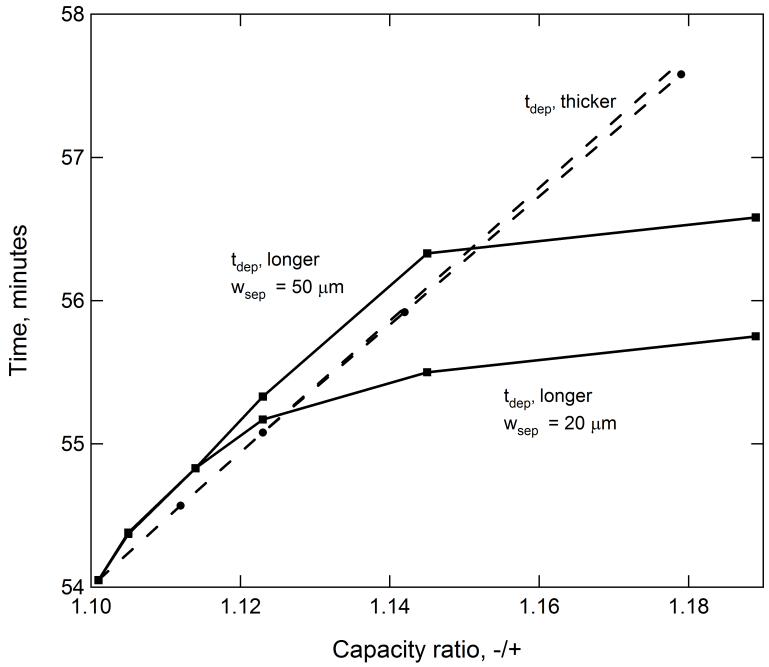

Figure 6.15: Time to deposition as electrode is either extended or thickened, for separator thicknesses of 20 and 50 μm. When the electrodes are farther apart, the difference between flowing directly across the separator and flowing out into the extension is smaller; thus adding capacity at the edge continues to be effective for a longer distance. Changing the separator thickness has very little effect on deposition time when the electrode is made thicker instead of longer.

distance that current must travel to reach the extension is less significant.

Extending the negative electrode also decreases the time to reach conditions that permit detrimental side reactions in the positive electrode, such as solvent oxidation. This is because the increased capacity at the edge of the negative draws a higher current from the edge of the positive, generating a greater potential drop at the positive edge. Choosing a lower cutoff potential will decrease the likelihood of both deposition and solvent oxidation because the cell will reach a lower cutoff potential sooner and stop charging before side reactions become possible; however, a lower cutoff potential will also decrease the total energy obtained, reducing cell performance.

List of Symbols

C	Capacity, C m^{-3}
c_s	Solid-phase lithium concentration, mol/m^3
c_t	Maximum solid-phase lithium concentration, mol/m^3
D	Diffusivity, m^2/s
E_{cell}	Cell voltage, V
F	Faraday's constant, 96487 C/mol
i_n	Current density, A/m^2
i_{eff}	Current density as expressed in Eq. 6.16, A/m^2
i_0	Exchange current density for lithium intercalation, A/m^2
I_{app}	Applied current density, equal to theoretical capacity of positive divided by time of charge, A/m^2
k	Lithium insertion rate constant, $m^{2.5}$/$mol^{0.5}$s
l	Length of electrode, m
n	Normal vector
s	Arc-length, m
t	Time, s
t_{charge}	Time of cell charge, s
U	Equilibrium potential, V
w	Electrode thickness, m
x	Stoichiometric coefficient of negative electrode
y	Stoichiometric coefficient of positive electrode
X	Position, m
Y	Position, m
α	Transfer coefficient
ϵ	Volume fraction
η	Overpotential, V
η_s	Surface overpotential, V
ϕ	Local potential, V
κ	Conductivity, S m^{-1}
ρ	Density, kg/m^3
Φ	Solid-phase potential, V
Subscripts	
1	Solid phase
2	Liquid phase
a	Anodic
c	Cathodic

Chapter 7

Cell-level modeling of overcharge protection

Developing new materials for testing is inherently expensive and time-consuming. Models can focus experimental work by determining limitations of current systems and suggesting specifications for new ones. In this section, we use system models and cell-cycling experiments to consider the possible benefits of redox shuttles for overcharge protection. We attempt to answer three questions.

1. What thermodynamic, transport, and kinetic properties would be necessary for a redox shuttle to provide overcharge protection, assuming that such a molecule could be created?

2. How are those properties affected by operating conditions and design parameters, such as the electrode thickness and porosity?

3. Would the shuttle introduce tradeoffs in performance? Narayanan suggested the possibility of an optimum redox potential for the shuttle: if the potential of the shuttle is too low, the electrode will not charge completely, but if the potential is too high, overcharge reactions will not be sufficiently prevented. Furthermore, the presence of natural overcharge protection in the nickel-metal hydride system causes self-discharge of the battery [93].

The use of macrohomogeneous models allows us to identify the optimal properties under both simplified and realistic operating conditions. Previous research on redox shuttles has focused almost exclusively on synthesizing and testing molecules, while theoretical aspects of this field have largely been confined to molecular simulations of the formal potential and stability of possible shuttle candidates [94]. The only systematic consideration of the thermodynamic, kinetic, or transport properties required for successful shuttle-provided overcharge protection seems to be early work by Narayanan, in which a simplified model was used to relate overcharge current to cell potential and to determine the limiting shuttle current [95].

The simplified model did not take into account the porous electrodes used in batteries, or the competing lithium insertion and overcharge reactions that shuttles are supposed to prevent.

7.1 Model development

The macrohomogeneous model for current distributions in porous electrodes has been solved using finite differences in the FORTRAN program Dualfoil for multiple applications [96]. Albertus et al. adapted the original lithium-ion model to the chemistry of the nickel-metal-hydride system, including the side reactions of oxygen and hydrogen generation on overcharge [93]. In this work, we adapt the side-reaction feature of their work to account for solvent oxidation at the cathode and a redox shuttle for overcharge protection.

Redox shuttles fall into two categories: generation of either a cationic or anionic radical. Current research has focused almost exclusively on the first category. In this case, the reactions at the electrodes on overcharge are

Positive electrode $Sh \rightarrow Sh^+ + e^-$

Negative electrode $Sh^+ + e^- \rightarrow Sh$

By our convention, the anodic current (generation of the cationic radical) is positive.

Only diffusion affects transport of the neutral molecule, but the oxidized cation, Sh^+, is also affected by migration. Concentrations of shuttle molecules are typically 0.05 to 0.1 M, and the electrolyte salt is typically 1.0 to 1.2 M; thus, the shuttle can be treated as a minor component in supporting electrolyte [23]. This means that the movement of the cation is governed by the Nernst-Planck equation:

$$\vec{N}_i = -z_i u_i F c_i \nabla\Phi - D_i \nabla c_i + c_i \vec{v} \tag{7.1}$$

with the migration term dropped. Because convection inside a porous electrode is zero, the shuttle is then affected only by diffusion, and a mass balance on the shuttle molecule reduces to

$$\varepsilon \frac{\partial c_i}{\partial t} = \nabla \cdot (D_{\text{eff}} \nabla c_i) + a j_{n,i} \tag{7.2}$$

where i = O or R, and where conservation of mass dictates that $j_{n,O} = -j_{n,R}$; that is, generation of Sh^+ corresponds to consumption of Sh. a is the specific surface area of the porous electrode. D_{eff} is the effective diffusivity, which includes the effects of porosity and tortuousity.

Finding the pore-wall flux $j_{n,i}$ in the porous electrode requires a kinetic rate expression:

$$j_{n,O} = k_a c_R \exp\left(\frac{\alpha_a F}{RT} V\right) - k_c c_O \exp\left(-\frac{(\alpha_c) F}{RT} V\right) \tag{7.3}$$

where V is the potential difference between the electrode and solution. At the equilibrium potential U, the rate is zero, and thus

$$k_a c_R \exp\left(\frac{\alpha_a F}{RT} V\right) = k_c c_O \exp\left(-\frac{\alpha_c F}{RT} V\right) \tag{7.4}$$

$$U = \frac{RT}{F} \ln\left(\frac{k_a c_O}{k_c c_R}\right) \tag{7.5}$$

c_O and c_R are the concentrations at the surface. If we replace them with reference concentrations, Equation 7.5 becomes

$$U^\theta = \frac{RT}{F} \ln\left(\frac{k_a c_{O,\text{ref}}}{k_c c_{R,\text{ref}}}\right) \tag{7.6}$$

V is replaced by

$$V = \eta + U^\theta \tag{7.7}$$

where η is defined as the difference between the equilibrium potential and the potential drop across the electrode-solution interface. Substituting Equations 7.6 and 7.7 into Equation 7.3 and rearranging yields

$$j_{n,O} = k_a^{\alpha_c} k_c^{\alpha_a} c_{O,\text{ref}}^{\alpha_a} c_{R,\text{ref}}^{\alpha_a} \left(\frac{c_R}{c_{R,\text{ref}}} \exp\left(\frac{\alpha_a F}{RT}\eta\right) - \frac{c_O}{c_{O,\text{ref}}} \exp\left(-\frac{\alpha_c F}{RT}\eta\right)\right) \tag{7.8}$$

Finally, we choose as a reference concentration half of the total shuttle, $\frac{1}{2}c_{\text{total}}$. Because $c_{O,\text{ref}} = c_{R,\text{ref}}$ and assuming that $\alpha_a = \alpha_a = 0.5$, the reference concentrations can be factored out of the expression, and the anodic and cathodic rate constants combined into one effective rate constant, k.

$$j_{n,O} = k\left(c_R \exp\left(\frac{\alpha_a F}{RT}\eta\right) - c_O \exp\left(-\frac{\alpha_c F}{RT}\eta\right)\right) \tag{7.9}$$

$j_{n,R} = -j_{n,O}$, and both of these reaction rates are related to the current in the porous electrode by $j_n = i_n/F$ for the one-electron reaction. Eq. 7.9 differs slightly from the standard Butler-Volmer form because when $\eta = 0$, current is not zero. By our convention, anodic currents (generation of the cationic shuttle species) are positive. Shuttle currents should be positive in the positive electrode and negative in the negative during charge or normal battery operation. If a graphite cell is severely overdischarged, the potential of the graphite may reach the potential of the shuttle molecule, and a positive shuttle current will occur in the negative electrode.

For the aromatic molecules often studied for overcharge protection, the redox kinetics are very fast and reactions are limited entirely by transport [95, 5, 16]. In this case, k in Eq. 7.9 is essentially a fitting parameter that we want to make infinitely large within the constraint of model convergence. However, such a high value of k is not universal, and if

the reaction is kinetically limited, k will be lower. It may also have different values at the different electrodes.

We also include in this model an irreversible oxidation side reaction at the positive electrode that occurs on overcharge, modeled with Tafel kinetics

$$i_{n,\text{side}} = Fk_s \exp\left(\alpha_a \frac{F}{RT}\eta_{\text{side}}\right) \tag{7.10}$$

$$\eta_{side} = V - U_{\text{side}} \tag{7.11}$$

This side reaction may represent any oxidation of the solvent or the electrode active material, and a key difference between it and the shuttle is that the overcharge reactions are irreversible. Because of the desired side reaction (the shuttle) and the undesired side reaction (the overcharge reaction), the current balance must be modified.

$$\nabla \cdot i_2 = aFj_{\text{main}} + a(i_{n,\text{side}} + i_{n,\text{shuttle}}) \tag{7.12}$$

In many practical cases the diffusion coefficients of the oxidized and reduced forms are very similar and can be treated as equal. In this case,

$$c^0 = c_{Sh}(x) + c_{Sh^+}(x) \tag{7.13}$$

where c^0 is the initial concentration of neutral shuttle added to the electrolyte. Because of this identity, we only need to model the concentration of one of the species in the system. To maintain consistency of signs and notation with oxygen evolution in the NiMH system, we choose the cation, or oxidized species (Sh^+). If, in addition, the reaction is fast enough to be in equilibrium, the concentration and potential at the electrode particle surface are related by the Nernst Equation,

$$\frac{c_O}{c_R} = \exp\left(\frac{F}{RT}\eta\right) \tag{7.14}$$

Combining Equations 7.13 and 7.14 gives the following expression for the shuttle pore-wall flux

$$j_n = -k_{Sh^+}\left(c_{Sh^+} - \frac{c^0 \exp\left(\frac{F}{RT}\eta\right)}{1 + \exp\left(\frac{F}{RT}\eta\right)}\right) \tag{7.15}$$

where k_{sh+} is a mass-transfer coefficient, D/δ. δ is the boundary-layer thickness inside the porous electrode. Although Equations 7.3 to 7.9 represent the system more rigorously than the simplified relations in 7.13 to 7.15, using these approximations reduces simulation time and improves convergence of the model. Calculation time can be reduced yet further if a zero-dimensional model is used. Zero-dimensional models apply at low rates, when transport limitations can be ignored. For the redox shuttle current, which is already limited by transport, the steady-state linear diffusion approximation is applied. A summary of the equations used in the simplified zero-dimensional model is shown in Table 7.1.

Table 7.1: Equations in zero-dimensional model.

Variable	Equation
y	$\frac{dy}{dt} = \frac{1}{Fc_{t,+}\epsilon_+ w_+} i_{\text{main}}$
i_{main}	$i_{\text{main}} = i_0 \left(\exp\left(\frac{\alpha_a F}{RT}(V - U(y))\right) - \exp\left(-\frac{(\alpha_c F}{RT}(V - U(y))\right)\right)$
	$i_0 = k_+ F c_{t,+} c_2^{\alpha_c} y^{\alpha_a} (1-y)^{\alpha_c}$
i_{side}	$i_{\text{side}} = k_s F c_2 \exp\left(\frac{\alpha_s F}{RT}(V - U_s)\right)$
i_{Sh}	$i_{Sh} = \frac{F D_{Sh} c^0}{w_{\text{sep}}} \frac{\exp\left(\frac{F}{RT}\eta\right)}{1+\exp\left(\frac{F}{RT}\eta\right)}$
V	$I_{\text{app}} = S_a w_+ \left(i_{\text{main}} + i_{\text{side}} + i_{Sh}\right)$

Table 7.2: Model parameters for full pseudo-2D model.

Parameter	Value	Units
$c_{t,+}$	278	mAh/g
ρ_+	4.75	g/cm^2
w_+	40	μm
ϵ_+	0.5075	
$k_{\text{main},+}$	1×10^{-12}	m$^{2.5}$/mol$^{0.5}$s
$\alpha_{\text{main},+}$	0.5	
c_2	1.0	M
w_{sep}	25	μm
ϵ_{sep}	0.55	
τ_{sep}	2.43	
U_{Sh}	4.43	V
D_{Sh}	1.4×10^{-6}	cm^2/s
$k_{Sh,mt}$	1×10^{-4}	cm^2/s

7.2 Model results

Current distribution in porous electrode

Figure 7.1 shows the simulated potential versus time in a lithium/lithium nickel-cobalt-manganese oxide (LiNCM) cell with 0.2 M of the molecule 2-(pentafluorophenyl)-tetrafluoro-1,3,2-benzodioxaborole (PFPTFB) [97]. Simulation parameters are given in Table 7.2. Units for the kinetic rate parameters are determined by the units of the exchange current densities [96]. As the overcharge current is increased from 0.017 to 3.4 mA/cm^2 (0.01 C to 2.0 C), the black arrows indicate the times at which concentration profiles of the shuttle cation versus cell sandwich position are shown in Figure 7.2. Figure 7.1 shows potential rising as the positive electrode is charged, then reaching a plateau as the shuttle molecules oxidize on the positive electrode and reduce on the negative. As the overcharge rate is increased, the cell potential also increases. This is because, at low overcharge currents, the shuttle can carry the current with a very small concentration gradient. As the rate increases, a larger

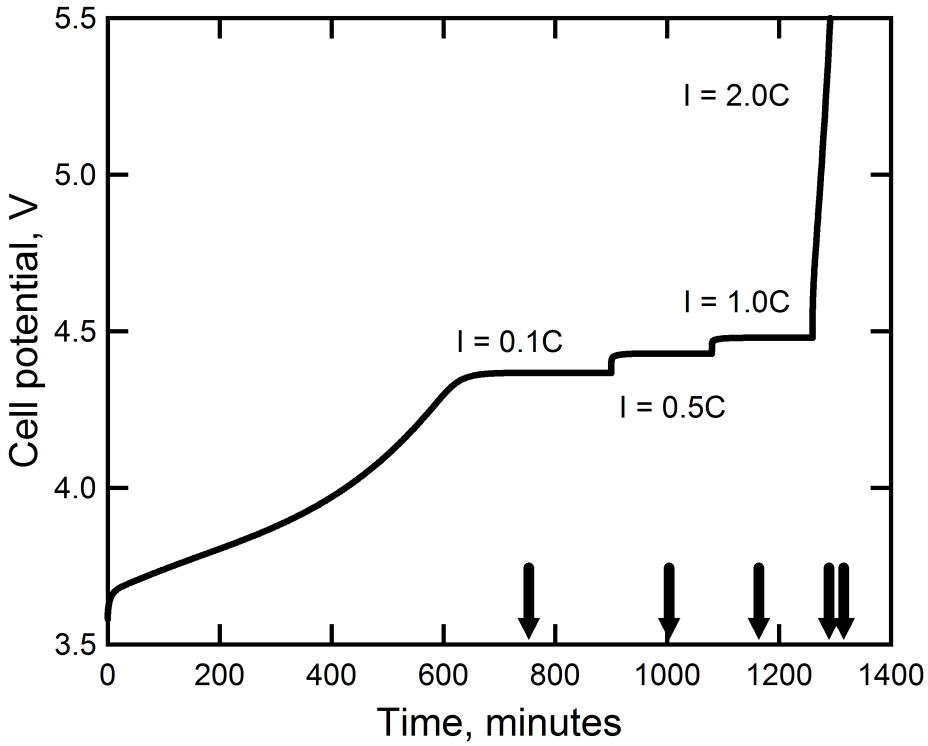

Figure 7.1: Simulated overcharge protection in a Li/NCM cell at increasing values of the overcharge current. The cell potential increases with increasing charge rate until the limiting current of the shuttle is reached. Black arrows indicate where concentration profiles are plotted in Figure 7.2.

gradient is required, and more of the total shuttle concentration exists as the charged species, as shown in Figure 7.2. A higher ratio of oxidized to reduced shuttle species corresponds to a greater overpotential and thus a higher operating potential. When the concentration gradient required to pass current is higher than the total added concentration of shuttle, the shuttle cannot provide overcharge protection. The limiting current of the shuttle is

$$i_{\text{lim,ovch}} = \frac{FD_{Sh}\epsilon_{\text{sep}}c^0}{w_{\text{sep}}\tau_{\text{sep}}} \tag{7.16}$$

Figure 7.2 shows that the time to reach a uniform steady-state concentration within the electrode is very short because, for a typical system, the time constant L^2/D is only a few seconds. Before steady-state is reached after each current change, the concentration decreases from the front to the back of the positive electrode. This is because the kinetics of the shuttle reaction is fast, causing a nonuniform reaction distribution within the porous electrode. The reaction distribution at 750 minutes, or the first black arrow in Figure 7.1, is plotted in Figure 7.3. The local transfer current, or reaction rate, falls off drastically from

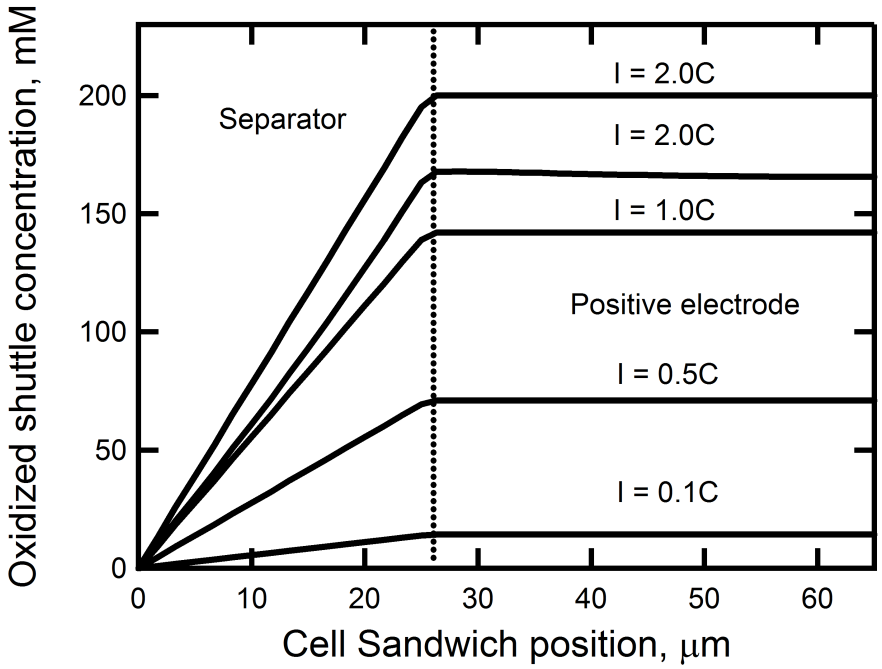

Figure 7.2: Concentration profiles of shuttle cation versus cell position at different times, as indicated by black arrows in Figure 7.1. The concentration is initially zero, but as cell potential rises, the cation is generated and diffuses across the separator. Concentration is zero in the negative electrode because the reaction is at the limiting current.

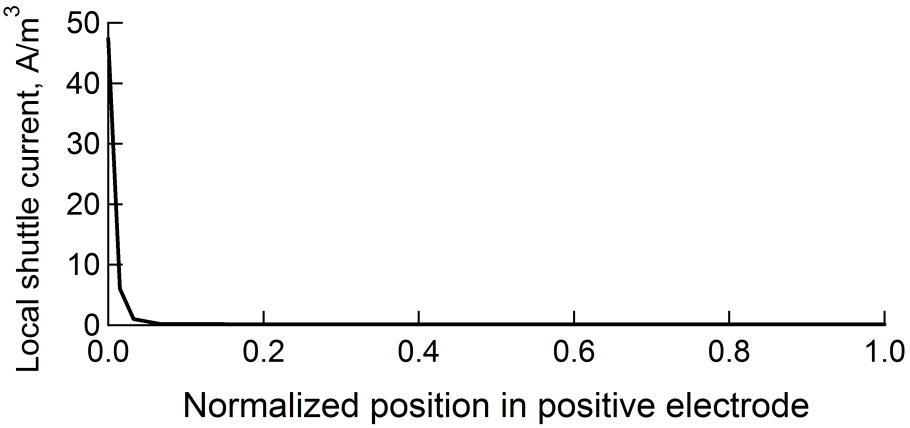

Figure 7.3: Reaction distribution versus normalized positive electrode position at 750 minutes. The reaction distribution is extremely nonuniform because the exchange current density is high and occurs preferentially at the front instead of the back of the electrode because liquid-phase conductivity is much lower than that of the solid phase.

the front to the back of the electrode. At later times, the shape of the distribution does not change although the magnitude of current increases at higher rates. The nonuniform reaction distribution can be explained by considering porous electrode theory and the dimensionless exchange current [23],

$$\nu^2 = (\alpha_a + \alpha_c)\frac{i_0 F a L^2}{RT}\left(\frac{1}{\kappa} + \frac{1}{\sigma}\right) \tag{7.17}$$

ν^2 is very large for redox shuttle reactions because, for a reversible reaction, i_0 is immeasurably high and ν^2 approaches infinity. Because the kinetic overpotential is negligible, cell resistance can thus be minimized by directing all current through one end of the electrode. Because solid-phase electronic conductivity in a nonaqueous battery is much higher than liquid-phase ionic conductivity, the reaction is at the front of the electrode. ν^2 does not include the effects of concentration overpotential, which will create a more even current distribution; thus, the current distribution in Fig. 7.3 in the absence of mass transport phenomena would be even more nonuniform. The nonuniformity of the reaction distribution suggests that electrode parameters such as thickness, porosity, and particle size will not be relevant to the application of redox shuttles in commercial cells when the diffusivities of the oxidized and reduced forms are equal. Although thicker or more porous electrodes provide a larger reservoir into which the oxidized cation can diffuse, a thicker or more porous electrode contains more electrolyte and thus more neutral shuttle molecules that can generate the cation. The net effect is that the shuttle quickly becomes oxidized through the depth of the porous electrode. The lack of concentration gradient anywhere away from the electrode/separator interface (Fig. 7.2) means that only the molecules at that interface diffuse towards the negative electrode.

Effect of electrode parameters on limiting current

In the simulation results above, the diffusivities of the oxidized and reduced forms of the shuttle were assumed to be equal. If the diffusivities of the oxidized and reduced forms are not equal, Eq. 7.13 will not hold, and electrode parameters may affect the ability of the shuttle to provide overcharge protection. Because of the nonuniform current density, a simple zero-dimensional model of the oxidized and reduced shuttle concentration can be used. To determine how the limiting overcharge current varies with electrode parameters such as thickness and porosity, we can write a mass balance on the total shuttle concentration (oxidized and reduced) at the limiting current during overcharge:

$$c^0(w_{\text{sep}} + \epsilon w_+) = \frac{c_R^* w_{\text{sep}}}{2} + c_O^*\left(\frac{w_{\text{sep}}}{2} + \epsilon w_+\right) \tag{7.18}$$

where c_O^* is the concentration of the oxidized cation in the positive electrode during overcharge and c_R^* is the concentration of the reduced neutral shuttle at the surface of the negative electrode. In Fig. 7.2, $c_R^* = c^0$ because of the requirement that $c_R + c_O = c^0$; however, if

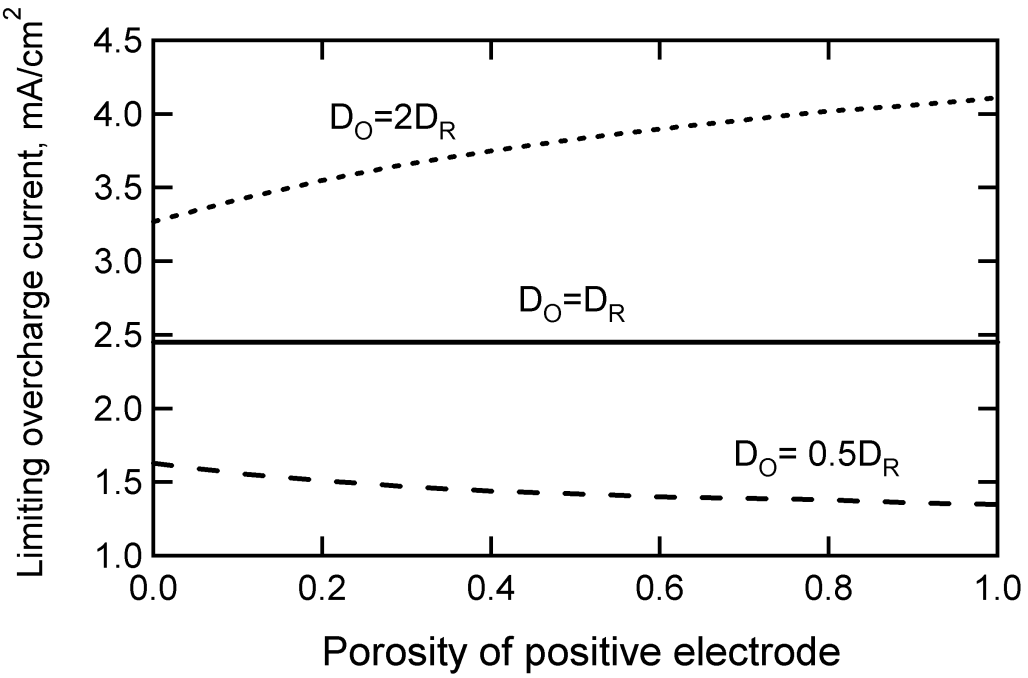

Figure 7.4: Calculated limiting overcharge current for different electrode porosities and ratios of D_O/D_R. As the reservoir volume increases, the transport properties of the oxidized species dominate the ability of the shuttle to provide overcharge protection.

$D_O \neq D_R$, at the limiting current

$$\frac{FD_O c_O^*}{w_{\text{sep}}} = \frac{FD_R c_R^*}{w_{\text{sep}}} \tag{7.19}$$

Combining and solving these two equations for the limiting overcharge current yields:

$$i_{\text{lim,ovch}} = \frac{FD_O c^0}{w_{\text{sep}}} c_O^* = \frac{FD_O c^0}{w_{\text{sep}}} \frac{w_{\text{sep}} + \epsilon w_+}{0.5 w_{\text{sep}}(1 + \frac{D_O}{D_R}) + \epsilon w_+} \tag{7.20}$$

For the case in which $D_O = D_R$, the reservoir of ϵw_+ cancels out and overcharge is independent of electrode parameters. If the diffusivities are not equal, increasing the reservoir size by increasing the porosity or electrode thickness increases the importance of the oxidized species on the limiting current. Fig. 7.4 shows the limiting overcharge current calculated for the case of $D_O = D_R$, $D_O = 2D_R$, and $D_O = 0.5D_R$ for porosity w_+ ranging from zero to one. All other parameters have the same values as used in the porous electrode simulations. As porosity increases, the size of the reservoir increases and the limiting current becomes closer to that of the oxidized species.

Effect of shuttle on self-discharge

The presence of natural overcharge protection in nickel metal hydride and nickel cadmium systems can lead to self discharge. The effect of a redox shuttle on self-discharge of the lithium/NCM system is shown in Figure 7.5. The simulated potential versus time is plotted

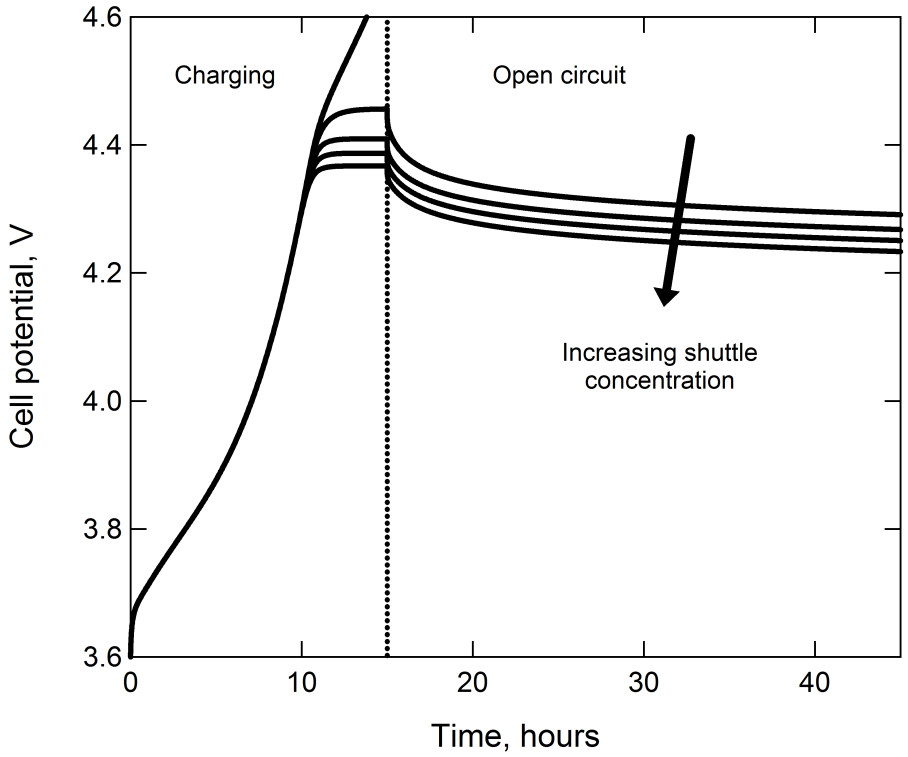

Figure 7.5: Simulated potential versus time of cell with 0.01, 0.025, 0.05, 0.1, and 0.2 M shuttle. The cell self discharges during open-circuit because the shuttle continues to oxidize on the positive electrode. For 0.01 M, cell potential shoots up because the shuttle concentration is not high enough to carry the overcharge current.

for different concentrations of the shuttle PFPTFB. The overcharge plateau increases from 3.71 to 3.8 V as total shuttle concentration decreases from 0.2 to 0.01 M because more overpotential is required to generate the concentration gradient that passes current. After fifteen hours, charge is stopped, and the cell is left at open circuit for 30 hours. During this time, cell potential decays because the shuttle is being oxidized at the positive electrode, discharging the cell in the process. After 30 hours of open-circuit, the cell potential has decayed by 0.14 to 0.17 V. Figure 7.5 shows that a higher concentration will have a more detrimental effect on self-discharge of batteries containing redox shuttles.

Table 7.3: Model parameters for zero-dimensional model.

Parameter	Value	Units
$c_{t,+}$	278	mAh/g
ρ_+	4.75	g/cm^3
w_+	40	μm
ϵ_+	0.5075	
$S_{a,+}$	9×10^4	cm^3/cm^3
$k_{\text{main},+}$	7.5×10^{-12}	m$^{2.5}$/mol$^{0.5}$s
$\alpha_{\text{main},+}$	0.5	
k_{side}	9×10^{-13}	m$^{2.5}$/mol$^{0.5}$s
α_{side}	0.5	
U_{side}	4.3	V
c_2	1.0	M
w_{sep}	25	μm
$D_{Sh,\text{eff}}$	2.5×10^{-6}	cm^2/s

Optimal shuttle redox potential

The cell-sandwich modeling results shown in Figures 7.1 to 7.5 agree qualitatively with published experiments [5]. Because of the nonuniform reaction distribution and short diffusion time constant, our models results do not differ significantly from the simple models presented in literature. Thus, we can use a simpler model when trying to determine the properties required for a redox shuttle to provide successful overcharge protection and to investigate the tradeoffs between overcharge protection and current efficiency. The zero-dimensional model described in Table 7.1 was used to approximate cell cycling data obtained from Lawrence Berkeley National Laboratory. The simulated and experimental cells are shown in Figure 7.6. Although the simulated current efficiency of 98.4% matched the experimental value, the capacity of the experimental cell in Figure 7.6 is offset by approximately 0.5 mA/cm^2. The offset comes from a measured first-cycle capacity loss that was much greater than the difference between charge and discharge on subsequent cycles, suggesting passivation phenomena, such as the formation of an SEI, not described by the simple Tafel equation used here.

The total current applied to the cell in Figure 7.6 during charge and discharge is 18 mA/cm^2. The breakdown of how this current is distributed between the reactions is shown in Figure 7.7. Initially, all current goes to the main intercalation reaction, but as potential rises, the overcharge reaction becomes favorable and begins to carry current, as shown by the increasing dotted line. Although this simulation does not define the oxidation as either a loss of cyclable lithium or active material, either of these situations will lead to capacity fade over time. If present, a redox shuttle reaction will begin to carry the current before the side reaction becomes favorable, as shown in Figure 7.8. In this simulation, the same parameters are used as previously, but the cell includes 200 mM of shuttle, and it is overcharged by 20%.

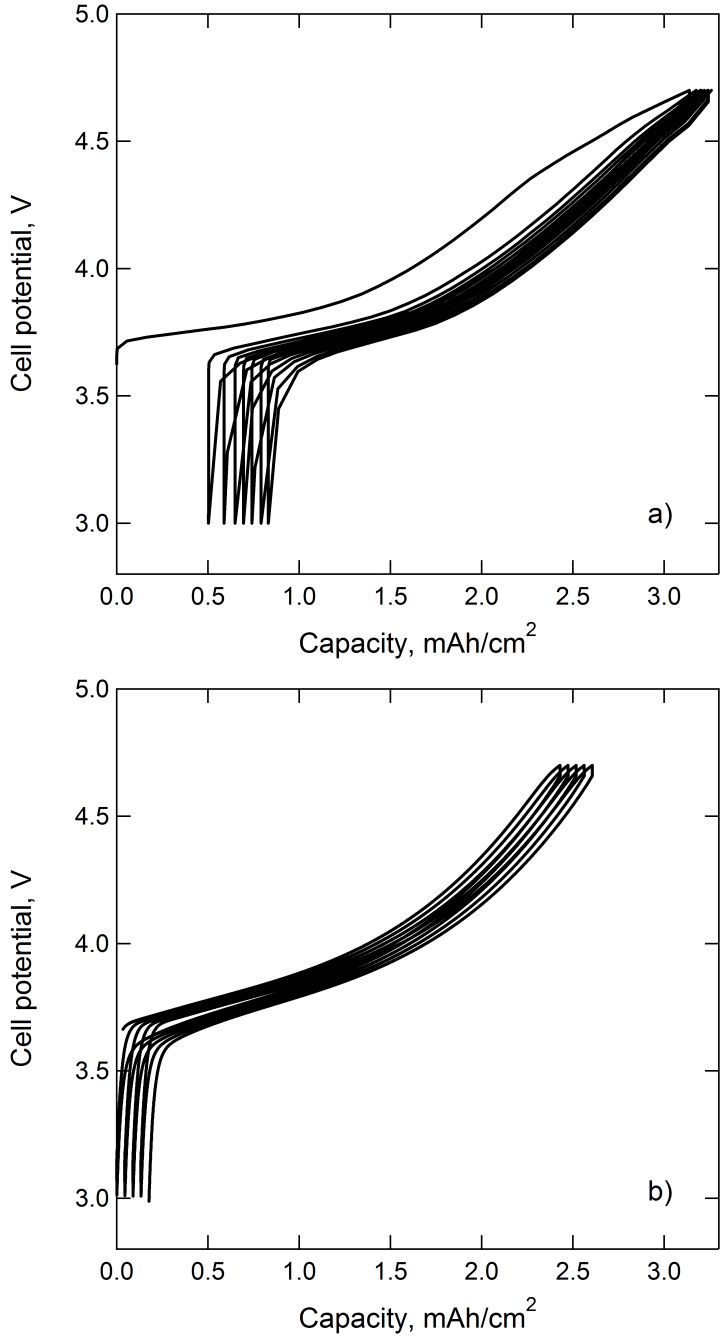

Figure 7.6: a) Measured and b) simulated cell potential versus capacity for a lithium/NCM cell. The charge capacity is greater than the discharge capacity, showing the presence of side reactions. The offset on the first cycle suggests formation of a solid-electrolyte-interphase not described by the simple model.

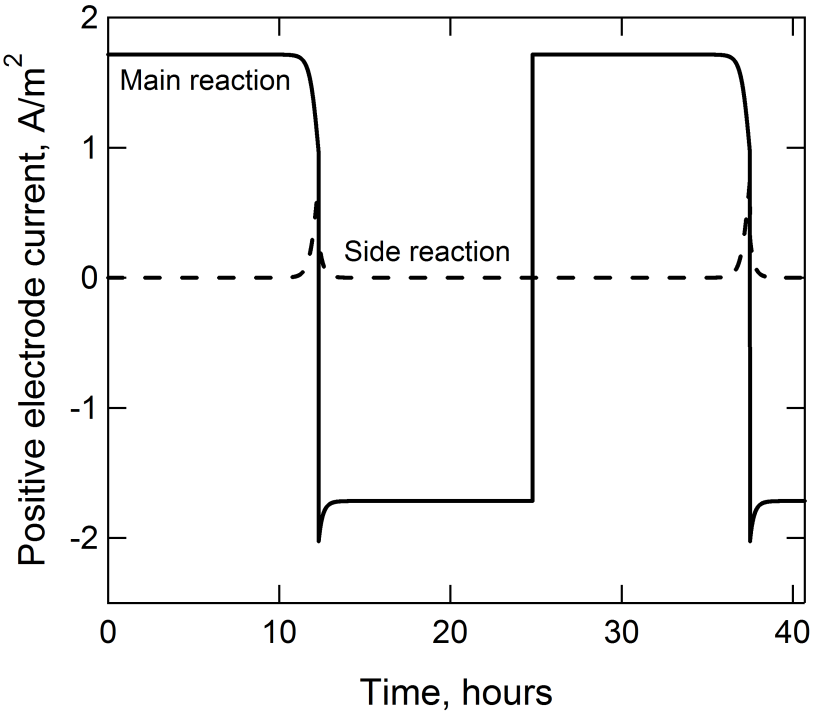

Figure 7.7: Main and overcharge reactions versus time. As potential rises, the amount of current going to the main reaction drops, and the side reaction increases.

The oxidation potential of the shuttle is varied to examine the tradeoffs between overcharge protection and current efficiency. As time increases and potential rises, the shuttle current becomes more favorable, and starts to carry all the current. Shuttles with lower oxidation potential react sooner and carry more charging current, which reduces the current efficiency. However, if the shuttle potential is too high, the side reaction is not prevented fully, shown by the dashed line. Integrating the currents from Figure 7.8 with respect to time in Figure 7.9 shows how much total current, or charge, has gone to each reaction as a function of shuttle redox potential. At low potential, the shuttle causes an extremely low energy efficiency, but at higher potential, the side reaction is not completely prevented. According to Figure 7.9, the optimal redox potential is between 4.4 and 4.5 V versus lithium.

In all of the simulation results shown above, the cell was assumed to remain isothermal during overcharge. For an industrial cell, this assumption is not realistic. When the shuttle is carrying overcharge current, no chemical work is accomplished; thus, all IR power passed to the cell is converted to heat, and the cell temperature rises. The amount of temperature rise depends on the current passed to the cell, the cell's internal resistance, the ratio of surface area to volume, and the heat-transfer coefficient outside the cell. A change in temperature will also affect the reactions inside the battery, including the overcharge reactions

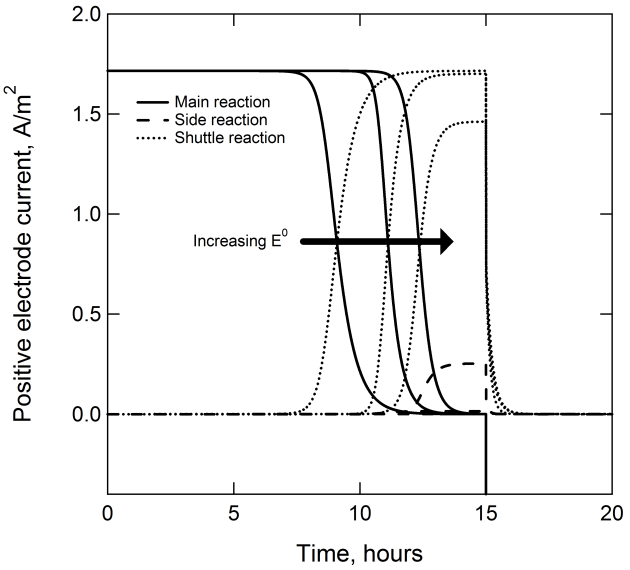

Figure 7.8: Breakdown of currents to main, overcharge, and shuttle reactions while including 200 mM of 4.2, 4.5, and 4.8 V redox shuttles. Increasing redox potential increases the current efficiency but increases the likelihood of overcharge reactions, represented by the dashed line.

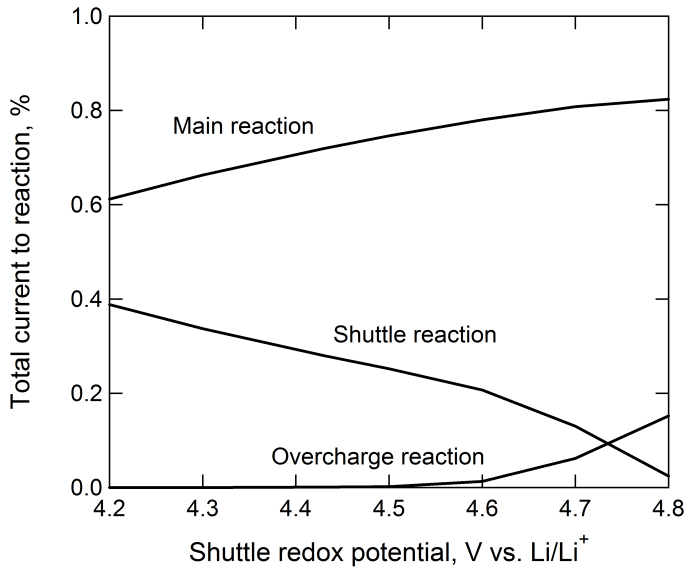

Figure 7.9: Total amount of current passed to each reaction versus shuttle redox potential, showing the tradeoff between current efficiency and overcharge protection.

that the shuttle is supposed to prevent and decomposition of the shuttle itself. The effect of temperature on capacity fade-causing reactions is extremely complex and the subject of

much current research, and it is beyond the scope of the current work to integrate redox shuttles into existing capacity-fade models.

7.3 Conclusions

In this chapter, we have used a system model in order to study how the presence of a redox shuttle affects the macroscale current-potential relations of the battery. We have shown that, for most realistic conditions, the current distribution of the redox shuttle will be highly nonuniform, which means that simpler models can be applied with minimal tradeoffs in accuracy. As the thickness and porosity of the positive electrode increase, the transport properties of the oxidized species become much more important than those of the reduced species when determining the limiting overcharge current. The presence of a redox shuttle can cause self-discharge within the cell; higher concentrations of shuttle will cause more self-discharge. Finally, considering only the tradeoffs between current efficiency and overcharge protection, the optimal redox potential for the conditions studied here is approximately 4.45 V versus lithium. In order to refine this optimum, a more sophisticated model for capacity fade should be developed, and the effects of temperature increase should be considered.

Bibliography

1. Vetter, J., Novák, M. R. P. Wagner, Veit, C., Möller, K. C., Besenhard, J. O., Winter, M., Wohlfahrt-Mehrens, M., Vogler, C. & Hammouche, A. Aging Mechanisms in Lithium-Ion Batteries. *Journal of Power Sources* **147,** 269–281 (2005).
2. Abraham, K. M., Pasquariello, D. M. & Willstaedt, E. B. Normal-Butylferrocene for Overcharge Protection of Secondary Lithium Batteries. *Journal of the Electrochemical Society* **137,** 1856–1857 (1990).
3. Golovin, M. N., Wilkinson, D. P., Dudley, J. T., Holonko, D. & Woo, S. Applications of Metallocenes in Rechargeable Lithium Batteries for Overcharge Protection. *Journal of the Electrochemical Society* **139,** 5–10 (1992).
4. Buhrmester, C., Chen, J., Moshurchak, L., Jiang, J. W., Wang, R. L. & Dahn, J. R. Studies of aromatic redox shuttle additives for LiFePO4-based Li-ion cells. *Journal of the Electrochemical Society* **152,** A2390–A2399 (2005).
5. Dahn, J. R., Jiang, J. W., Moshurchak, L. M., Fleischauer, M. D., Buhrmester, C. & Krause, L. J. High-rate overcharge protection of LiFePO4-based Li-ion cells using the redox shuttle additive 2,5-ditertbutyl-1,4-dimethoxybenzene. *Journal of the Electrochemical Society* **152,** A1283–A1289 (2005).
6. Peled, E. The Electrochemical Behavior of Alkali and Alkaline Earth Metals in Nonaqueous Battery Systems—The Solid Electrolyte Interphase Model. *Journal of The Electrochemical Society* **126,** 2047–2051 (1979).
7. Peled, E. *Lithium Batteries* (ed Gabano, J. P.) (Academic Press, London, 1983).
8. Andersson, A. M., Henningson, A., Siegbahn, H., Jansson, U. & Edstrom, K. Electrochemically lithiated graphite characterised by photoelectron spectroscopy. *Journal of Power Sources* **119,** 522–527 (2003).
9. Bar-Tow, D., Peled, E. & Burstein, L. A Study of Highly Oriented Pyrolytic Graphite as a Model for the Graphite Anode in Li-Ion Batteries. *Journal of the Electrochemical Society* **146,** 824–832 (1999).
10. Xu, K. Nonaqueous liquid electrolytes for lithium-based rechargeable batteries. *Chemical Reviews* **104,** 4303–4417 (2004).

11. Verma, P., Maire, P. & Novák, P. A review of the features and analyses of the solid electrolyte interphase in Li-ion batteries. *Electrochimica Acta* **55,** 6332–6341. ISSN: 00134686 (Sept. 2010).

12. Ploehn, H. J., Ramadass, P. & White, R. E. Solvent Diffusion Model for Aging of Lithium-Ion Battery Cells. *Journal of The Electrochemical Society* **151,** A456–A462 (2004).

13. Broussely, M., Herreyre, S., Biensan, P., Kasztejna, P., Nechev, K. & Staniewicz, R. J. Aging mechanism in Li ion cells and calendar life predictions. *Journal of Power Sources* **97-98,** 13–21 (2001).

14. Christensen, J. & Newman, J. A Mathematical Model for the Lithium-Ion Negative Electrode Solid Electrolyte Interphase. *Journal of The Electrochemical Society* **151,** A1977–A1988 (2004).

15. Safari, M., Morcrette, M., Teyssot, A. & Delacourt, C. Multimodal Physics-Based Aging Model for Life Prediction of Li-Ion Batteries. *Journal of The Electrochemical Society* **156,** A145–A153 (2009).

16. Moshurchak, L. M., Buhrmester, C., Wang, R. L. & Dahn, J. R. Comparative studies of three redox shuttle molecule classes for overcharge protection of $LiFePO_4$-based Li-ion cells. *Electrochimica Acta* **52,** 3779–3784 (2007).

17. Marcus, R. A. & Sutin, N. Electron Transfers in Chemistry and Biology. *Biochimica Et Biophysica Acta* **811,** 265–322 (1985).

18. Aurbach, D. *Nonaqueous Electrochemistry* (Marcel Dekker, New York, 1999).

19. Xu, K., Ding, S. P. & Jow, T. R. Toward Reliable Values of Electrochemical Stability Limits for Electrolytes. *Journal of The Electrochemical Society* **146,** 4172–4178 (1999).

20. Kostecki, R. & McLarnon, F. Microprobe study of the effect of Li intercalation on the structure of graphite. *Journal of Power Sources* **119,** 550–554 (2003).

21. Jenkins, G. & Kawamura, K. Structure of glassy carbon. *Nature* **231,** 175–176 (1971).

22. Ehrlich, G. M. in *Handbook of Batteries* (eds Linden, D. & Reddy, T. B.) 3rd ed. Chap. 35 (McGraw-Hill, 2002).

23. Newman, J. & Thomas-Alyea, K. E. *Electrochemical Systems* 3rd ed. (John Wiley and Sons, New York, 2004).

24. Bard, A. J. & Faulkner, L. R. *Electrochemical Methods* 2nd ed., 833. ISBN: 9780471043720 (John Wiley and Sons, Hoboken, 2001).

25. Gough, D. A. & Leypoldt, J. K. Membrane-covered, rotated disk electrode. *Analytical Chemistry* **51,** 439–444 (1979).

26. Peerce, P. J & Bard, A. J. Polymer Films on Electrodes: Part II. Film Structure and Mechanism of Electron Transfer with Electrodeposited Poly(vinylferrocene). *Electrochimica Acta* **112,** 97–115 (1980).

27. Leddy, J. A., Bard, A. J., Maloy, J. T. & Savéant, J. M. Kinetics of Film-Coated Electrodes - Effect of a Finite Mass-Transfer Rate of Substrate across the Film Solution Interface at Steady-State. *Journal of Electroanalytical Chemistry* **187,** 205–227 (1985).

28. Abraham, D. P., Knuth, J. L., Dees, D. W., Bloom, I. & Christophersen, J. P. Performance degradation of high-power lithium-ion cells–Electrochemistry of harvested electrodes. *Journal of Power Sources* **170,** 465–475 (2007).

29. Du Pasquier, A., Disma, F., Bowmer, T., Gozdz, A. S., Amatucci, G. & Tarascon, J. M. Differential Scanning Calorimetry Study of the Reactivity of Carbon Anodes in Plastic Li-Ion Batteries. *Journal of the Electrochemical Society* **145,** 472–477 (1998).

30. Amatore, C., Savéant, J. M. & Tessier, D. Kinetics of Electron-Transfer to Organic-Molecules at Solid Electrodes in Organic Media. *Journal of Electroanalytical Chemistry* **146,** 37–45 (1983).

31. Laoire, C. O., Plichta, E., Hendrickson, M., Mukerjee, S. & Abraham, K. M. Electrochemical studies of ferrocene in a lithium ion conducting organic carbonate electrolyte. *Electrochimica Acta* **54,** 6560–6564 (2009).

32. Stewart, S. G. *Determination of Transport Properties and Optimization of Lithium-Ion Batteries* PhD thesis (University of California, Berkeley, 2007).

33. Aurbach, D., Ein-Eli, Y., Markovsky, B., Zaban, A., Luski, S., Carmeli, Y. & Yamin, H. The Study of Electrolyte Solutions Based on Ethylene and Diethyl Carbonates for Rechargeable Li Batteries. *Journal of The Electrochemical Society* **142,** 2882–2890 (1995).

34. Aurbach, D., Zaban, A., Schechter, A., Ein-Eli, Y., Zinigrad, E. & Markovsky, B. The Study of Electrolyte Solutions Based on Ethylene and Diethyl Carbonates for Rechargeable Li Batteries. *Journal of The Electrochemical Society* **142,** 2873–2882 (1995).

35. Borodin, O., Smith, G. D. & Fan, P. Molecular dynamics simulations of lithium alkyl carbonates. *Journal of Physical Chemistry B* **110,** 22773–22779 (2006).

36. Sleigh, A. K. & von Sacken, U. Unusual cycling behaviour of disordered carbons in Li/C cells. *Solid State Ionics* **57,** 99–102 (1992).

37. Fong, R., von Sacken, U. & Dahn, J. R. Studies of Lithium Intercalation into Carbons Using Nonaqueous Electrochemical Cells. *Journal of The Electrochemical Society* **137,** 2009–2013 (1990).

38. Zhang, X. R., Kostecki, R., Richardson, T. J., Pugh, J. K. & Ross, P. N. Electrochemical and infrared studies of the reduction of organic carbonates. *Journal of the Electrochemical Society* **148,** A1341–A1345 (2001).

39. Zhang, S., Ding, M. S., Xu, K., Allen, J. & Jow, T. R. Understanding Solid Electrolyte Interface Film Formation on Graphite Electrodes. *Electrochemical and Solid-State Letters* **4,** A206–A208 (2001).

40. Gritzner, G. & Kuta, J. Recommendations on Reporting Electrode-Potentials in Non-Aqueous Solvents. *Pure and Applied Chemistry* **54,** 1527–1532 (1982).

41. Smalley, J. F., Feldberg, S. W., Chidsey, C. E. D., Linford, M. R., Newton, M. D. & Liu, Y. P. The Kinetics of Electron-Transfer through Ferrocene-Terminated Alkanethiol Monolayers on Gold. *Journal of Physical Chemistry* **99,** 13141–13149 (1995).

42. Savéant, J.-M. Permeation through polymer coatings on electrodes : Membrane versus pinhole permeation. *Journal of Electroanalytical Chemistry* **302,** 91–101 (1991).

43. Aurbach, D., Moshkovich, M., Cohen, Y. & Schechter, A. The Study of Surface Film Formation on Noble-Metal Electrodes in Alkyl Carbonates/Li Salt Solutions, Using Simultaneous in Situ AFM, EQCM, FTIR, and EIS. *Langmuir* **15,** 2947–2960. ISSN: 0743-7463 (Apr. 1999).

44. Zaban, A., Zinigrad, E. & Aurbach, D. Impedance Spectroscopy of Li Electrodes. 4. A General Simple Model of the LiSolution Interphase in Polar Aprotic Systems. *The Journal of Physical Chemistry* **100,** 3089–3101. ISSN: 0022-3654 (Jan. 1996).

45. Tribollet, B. & Newman, J. The Modulated Flow at a Rotating Disk Electrode. *Journal of the Electrochemical Society* **130,** 2016–2026 (1983).

46. Meyers, J. P., Doyle, M., Darling, R. M. & Newman, J. The impedance response of a porous electrode composed of intercalation particles. *Journal of the Electrochemical Society* **147,** 99 (2000).

47. Doyle, M., Meyers, J. P. & Newman, J. Computer simulations of the impedance response of lithium rechargeable batteries. *Journal of the Electrochemical Society* **147,** 99 (2000).

48. Deslouis, C., Tribollet, B., Duprat, M & Moran, F. Transient Mass Transfer at a Coated Rotating Disk Electrode. *Journal of the Electrochemical Society* **134,** 2496–2501 (1987).

49. Tang, M. & Newman, J. Electrochemical Characterization of SEI-Type Passivating Films Using Redox Shuttles. *Journal of the Electrochemical Society* **158,** A530–A536. ISSN: 00134651 (2011).

50. Rice, R. J., Pontikos, N. & McCreery, R. L. Quantitative correlations of heterogeneous electron-transfer kinetics with surface properties of glassy carbon electrodes. *Journal of the American Chemical Society* **112,** 4617–4622. ISSN: 0002-7863 (1990).

51. Rice, R. J. & McCreery, R. L. Quantitative relationship between electron transfer rate and surface microstructure of laser-modified graphite electrodes. *Analytical Chemistry* **61,** 1637–1641. ISSN: 0003-2700 (Aug. 1989).

52. Hirasawa, K., Sato, T., Asahina, H, Yamaguchi, S. & Mori, S. In Situ Electrochemical Atomic Force Microscope Study on Graphite Electrodes. *Journal of the Electrochemical Society* **144,** L81–L84. ISSN: 00134651 (1997).

53. Chu, A. C., Josefowicz, J. Y. & Farrington, G. C. Electrochemistry of Highly Ordered Pyrolytic Graphite Surface Film Formation Observed by Atomic Force Microscopy. *Journal of the Electrochemical Society* **144,** 4161–4169 (1997).

54. Cabaniss, G. E., Diamantis, A. A., Murphy, W. R., Linton, R. W. & Meyer, T. J. Electrocatalysis of proton-coupled electron-transfer reactions at glassy carbon electrodes. *Journal of the American Chemical Society* **107,** 1845–1853. ISSN: 0002-7863 (Apr. 1985).

55. Alliata, D, Koetz, R, Novák, P. & Siegenthaler, H. Electrochemical SPM investigation of the solid electrolyte interphase film formed on HOPG electrodes. *Electrochemistry Communications* **2,** 436–440. ISSN: 13882481 (June 2000).

56. Aurbach, D. & Zaban, A. Impedance Spectroscopy of Nonactive Metal-Electrodes at Low Potentials in Propylene Carbonate Solutions - a Comparison to Studies of Li Electrodes. *Journal of the Electrochemical Society* **141,** 1808–1819 (1994).

57. Marom, R., Haik, O., Aurbach, D. & Halalay, I. C. Revisiting LiClO[sub 4] as an Electrolyte for Rechargeable Lithium-Ion Batteries. *Journal of The Electrochemical Society* **157,** A972. ISSN: 00134651 (2010).

58. Yamada, Y., Miyazaki, K. & Abe, T. Role of Edge Orientation in Kinetics of Electrochemical Intercalation of Lithium-Ion at Graphite. *Langmuir* **26,** 14990–14994 (2010).

59. Spahr, M. E., Buqa, H., Würsig, A., Goers, D., Hardwick, L., Novák, P., Krumeich, F., Dentzer, J. & Vix-Guterl, C. Surface reactivity of graphite materials and their surface passivation during the first electrochemical lithium insertion. *Journal of Power Sources* **153,** 300–311. ISSN: 03787753 (Feb. 2006).

60. Bernardo, P., Dentzer, J., Gadiou, R., Märkle, W., Goers, D., Novák, P., Spahr, M. & Vix-Guterl, C. Influence of graphite surface properties on the first electrochemical lithium intercalation. *Carbon* **49,** 4867–4876. ISSN: 00086223 (Nov. 2011).

61. Tang, M. & Newman, J. Transient Characterization of Solid-Electrolyte-Interphase Using Ferrocene. *Journal of The Electrochemical Society* **159,** A281. ISSN: 00134651 (2012).

62. Amatore, C., Savéant, J.-M. & Tessier, D. Charge transfer at partially blocked surfaces:: A model for the case of microscopic active and inactive sites. *Journal of Electroanalytical Chemistry* **147,** 39–51. ISSN: 0022-0728 (1983).

63. Yamada, Y., Iriyama, Y, Abe, T. & Ogumi, Z. Kinetics of Lithium Ion Transfer at the Interface between Graphite and Liquid Electrolytes: Effects of Solvent and Surface Film. *Langmuir* **25,** 12766–12770 (2009).

64. Randin, J.-P. & Yeager, E. Differential Capacitance Study of Stress-Annealed Pyrolytic Graphite Electrodes. *Journal of the Electrochemical Society* **118,** 711–714 (1971).

65. Davies, T. J., Moore, R. R., Banks, C. E. & Compton, R. G. The cyclic voltammetric response of electrochemically heterogeneous surfaces. *Journal of Electroanalytical Chemistry* **574,** 123–152. ISSN: 00220728 (Dec. 2004).

66. Besenhard, J. O. Filming mechanism of lithium-carbon anodes in organic and inorganic electrolytes. *Journal of Power Sources* **54,** 228–231. ISSN: 03787753 (Apr. 1995).

67. Aurbach, D., Daroux, M., Faguy, P. & Yeager, E. The electrochemistry of noble metal electrodes in aprotic organic solvents containing lithium salts. *Journal of Electroanalytical Chemistry* **297,** 225–244. ISSN: 00220728 (Jan. 1991).

68. McCloskey, B., Bethune, D., Shelby, R., Girishkumar, G & Luntz, A. Solvents Critical Role in Nonaqueous Lithium-Oxygen Battery Electrochemistry. *The Journal of Physical Chemistry Letters* **2,** 1161–1166 (2011).

69. Tasaki, K., Goldberg, A., Lian, J.-J., Walker, M., Timmons, A. & Harris, S. J. Solubility of Lithium Salts Formed on the Lithium-Ion Battery Negative Electrode Surface in Organic Solvents. *Journal of The Electrochemical Society* **156,** A1019. ISSN: 00134651 (2009).

70. Imhof, R. & Novák, P. In Situ Investigation of the Electrochemical Reduction of Carbonate Electrolyte Solutions at Graphite Electrodes. *Journal of the Electrochemical Society* **145,** 1081–1087 (1998).

71. Arora, P., Doyle, M. & White, R. E. Mathematical Modeling of the Lithium Deposition Overcharge Reaction in Lithium-Ion Batteries Using Carbon-Based Negative Electrodes. *Journal of The Electrochemical Society* **146,** 3543–3553 (1999).

72. Doyle, M., Fuller, T. F. & Newman, J. Modeling of Galvanostatic Charge and Discharge of the Lithium Polymer Insertion Cell. *Journal of the Electrochemical Society* **140,** 1526–1533 (1993).

73. Fuller, T. F., Doyle, M. & Newman, J. Simulation and Optimization of the Dual Lithium Ion Insertion Cell. *Journal of the Electrochemical Society* **141,** 1–10 (1994).

74. Doyle, M., Newman, J., Gozdz, A. S., Schmutz, C. N. & Tarascon, J. M. Comparison of modeling predictions with experimental data from plastic lithium ion cells. *Journal of the Electrochemical Society* **143,** 1890–1903 (1996).

75. Scott, E. *Personal communication* 2008.

76. Scott, E., Tam, G., Anderson, B. & Schmidt, C. in *204th Meeting of the Electrochemical Society* (Orlando, 2003).

77. Spotnitz, R. *Personal communication* 2008.

78. Winter, M., Besenhard, J. O., Spahr, M. E. & Novak, P. Insertion electrode materials for rechargeable lithium batteries. *Advanced Materials* **10,** 725–763 (1998).

79. Plichta, E., Slane, S., Uchiyama, M., Salomon, M., Chua, D., Ebner, W. B. & Lin, H. W. An Improved Li/Li[sub x]CoO[sub 2] Rechargeable Cell. *Journal of The Electrochemical Society* **136,** 1865–1869 (1989).

80. Auborn, J. J. & Barberio, Y. L. Lithium Intercalation Cells Without Metallic Lithium. *Journal of The Electrochemical Society* **134,** 638–641 (1987).

81. Doyle, M. & Fuentes, Y. Computer simulations of a lithium-ion polymer battery and implications for higher capacity next-generation battery designs. *Journal of the Electrochemical Society* **150,** A706–A713 (2003).

82. Mizushima, K., Jones, P. C., Wiseman, P. J. & Goodenough, J. B. LixCoo2 (O Less-Than X Less-Than-or-Equal-to 1) - a New Cathode Material for Batteries of High-Energy Density. *Solid State Ionics* **3-4,** 171–174 (1981).

83. Thomas, M. G. S. R., Bruce, P. G. & Goodenough, J. B. Lithium mobility in the layered oxide Li1-xCoO2. *Solid State Ionics* **17,** 13–19 (1985).

84. Honders, A., der Kinderen, J. M., van Heeren, A. H., de Wit, J. H. W. & Broers, G. H. J. Bounded diffusion in solid solution electrode powder compacts. Part II. The simultaneous measurement of the chemical diffusion coefficient and the thermodynamic factor in LixTiS2 and LixCoO2. *Solid State Ionics* **15,** 265–276 (1985).

85. Dokko, K., Mohamedi, M., Fujita, Y., Itoh, T., Nishizawa, M., Umeda, M. & Uchida, I. Kinetic characterization of single particles of LiCoO2 by AC impedance and potential step methods. *Journal of the Electrochemical Society* **148,** A422–A426 (2001).

86. Sato, H., Takahashi, D., Nishina, T. & Uchida, I. Electrochemical characterization of thin-film LiCoO2 electrodes in propylene carbonate solutions. *Journal of Power Sources* **68,** 540–544 (1997).

87. Morita, M., Nishimura, N. & Matsuda, Y. Charge Discharge Cycling Behavior of Pitch-Based Carbon-Fiber in Organic Electrolyte-Solutions. *Electrochimica Acta* **38,** 1721–1726 (1993).

88. Takami, N., Satoh, A., Hara, M. & Ohsaki, T. Structural and Kinetic Characterization of Lithium Intercalation into Carbon Anodes for Secondary Lithium Batteries. *Journal of The Electrochemical Society* **142,** 371–379 (1995).

89. Verbrugge, M. W. & Koch, B. J. Lithium Intercalation of Carbon-Fiber Microelectrodes. *Journal of The Electrochemical Society* **143,** 24–31 (1996).

90. Yu, P., Popov, B. N., Ritter, J. A. & White, R. E. Determination of the Lithium Ion Diffusion Coefficient in Graphite. *Journal of The Electrochemical Society* **146,** 8–14 (1999).

91. Christensen, J., Srinivasan, V. & Newman, J. Optimization of Lithium Titanate Electrodes for High-Power Cells. *Journal of The Electrochemical Society* **153,** A560–A565 (2006).

92. Tiedemann, W. & Newman, J. in *Proceedings of the Symposium on Battery Design and Optimization* (ed Gross, S.) (Princeton: The Electrochemical Society, Pittsburgh, PA, 1979), 39–49.

93. Albertus, P., Christensen, J. & Newman, J. Modeling Side Reactions and Nonisothermal Effects in Nickel Metal-Hydride Batteries. *Journal of The Electrochemical Society* **155,** A48–A60 (2008).

94. Chen, Z. H., Wang, Q. Z. & Amine, K. Understanding the stability of aromatic redox shuttles for overcharge protection of lithium-ion cells. *Journal of the Electrochemical Society* **153,** A2215–A2219 (2006).

95. Narayanan, S. R., Surampudi, S., Attia, A. I. & Bankston, C. P. Analysis of Redox Additive-Based Overcharge Protection for Rechargeable Lithium Batteries. *Journal of The Electrochemical Society* **138,** 2224–2229 (1991).

96. Doyle, M., Fuller, T. F. & Newman, J. Modeling of Galvanostatic Charge and Discharge of the Lithium Polymer Insertion Cell. *Journal of the Electrochemical Society* **140,** 1526–1533 (1993).

97. Chen, Z. & Amine, K. Bifunctional electrolyte additive for lithium-ion batteries. *Electrochemistry Communications* **9,** 703–707 (2007).